INDOOR LOCALIZATION BASED ON RADIO INTERFEROMETRIC POSITIONING SYSTEM

A Thesis
Presented to
The Academic Faculty

by

Marie Shinotsuka

In Partial Fulfillment
of the Requirements for the Degree
Doctor of Philosophy in the
School of Electrical and Computer Engineering

Georgia Institute of Technology
December 2015

INDOOR LOCALIZATION BASED ON RADIO INTERFEROMETRIC POSITIONING SYSTEM

Approved by:

Dr. Xiaoli Ma, Advisor
School of Electrical and Computer Engineering
Georgia Institute of Technology

Dr. Robert J. Baxley
Chief Engineer
Bastille

Dr. G. Tong Zhou, Co-advisor
School of Electrical and Computer Engineering
Georgia Institute of Technology

Dr. Mary Ann Weitnauer
School of Electrical and Computer Engineering
Georgia Institute of Technology

Dr. Gee-Kung Chang
School of Electrical and Computer Engineering
Georgia Institute of Technology

Dr. Wen Zhan Song
Department of Computer Science
Georgia State University

Date Approved: July 31, 2015

To my parents and brother,

ACKNOWLEDGEMENTS

First and foremost, I would like to thank my advisors Dr. Xiaoli Ma and Dr. G. Tong Zhou for their continuous support and guidance throughout my Ph.D. studies at Georgia Tech. Without their dedication and leadership, I would not been able to achieve the goal. They always inspired and enlightened me. They provided every opportunities possible for me to develop as a researcher. They had given me a chance to work in Shenzhen, China, where I had the opportunity to work closely with diverse students and experience the different culture at first hand. I feel lucky to have such inspirational females as my advisors.

I also would like to thank Dr. Yiyin Wang from Shanghai Jiao Tong University for her continuous support since she came to Georgia Tech as a post-doctoral researcher. She had given me insights that significantly improved my work. Also, I would like to thank Dr. Gee-Kung Chang for his suggestions and encouragements. Collaborations with his group had played a significant part of my dissertation and Ph.D. research, and I especially thank Lin Cheng and Feng Lu from Dr. Chang's group for helping me building prototypes and providing comments from different perspectives. I also would like to thank Dr. Robert J. Baxley, Dr. Mary Ann Weitnauer, and Dr. Wen Zhan Song for kindly accepting to service on my thesis committee and providing useful comments to improve the quality of this dissertation.

I also would like to thank the members of my research group at Georgia Tech. Special thanks to Dr. Hayang Kim for her continuous friendship and support even after her graduation, Yiming Kong for sharing memorable time with me in Shenzhen, and Dr. Malik M. U. Gul for his help in prototyping. Also, I would like to thank Dr. Zhenhua Yu, Hyunwoo Cho, Qingson Wen, Kai Ying, Lian Li, Brian Beck and

Andrew Harper. I sincerely enjoyed and learned a lot from insightful discussions with them.

Last but not least, I would like to thank my family, especially my parents and brother. They are a source of inspiration throughout my life and give me courage to overcome difficulties and challenges.

TABLE OF CONTENTS

LIST OF TABLES

LIST OF FIGURES

LIST OF SYMBOLS OR ABBREVIATIONS

ACF Autocorrelation Function.

AIPS Accurate Indoor Positioning System.

AM Amplitude Modulation.

AR1 First-Order Autoregressive.

ARIPS Asynchronous Radio Interferometric Positioning System.

AWGN Additive White Gaussian Noise.

BPF Band-Pass Filter.

CDF Cumulative Distribution Function.

CFO Carrier Frequency Offset.

CRLB Cramér-Rao Lower Bound.

CRT Chinese Remainder Theorem.

CSI Channel State Information.

CW Continuous-Wave.

DRIPS Dual-tone Radio Interferometric Positioning System.

DSB-SC Double-Sideband Suppressed-Carrier.

EA Electrical Amplifier.

EDFA Erbium-doped Fiber Amplifier.

ESPRIT Estimation of Signal Parameters via Rotation Invariance Techniques.

FIM Fisher Information Matrix.

GA Generic Algorithm.

GPS Global Positioning System.

HA Horn Antenna.

IF Intermediate Frequency.

IL Interleaver.

LFM Linear-Frequency Modulation.

LHS Left-Hand Side.

LO Local Oscillator.

LOS Line-of-Sight.

LPF Low-Pass Filter.

LSE Least Squares Estimator.

MAE Mean-Absolute Error.

MIE Method of Interval Error.

MIMO Multiple-Input and Multiple-Output.

MLE Maximum Likelihood Estimator.

MMW Millimeter Wave.

MZM Mach-Zehnder Modulator.

NI National Instruments.

OFDM Orthogonal Frequency-Division Multiplexing.

ORP Optical Received Power.

PC Polarization Controller.

PD Photodiode.

PSD Power Spectral Density.

PXI PCI Extensions for Instrumentation.

RD Range Difference.

RF Radio Frequency.

RHS Right-Hand Side.

RIPS Radio Interferometric Positioning System.

RIPS-sq Radio Interferometric Positioning System with Square-law Device.

RIPS-u Radio Interferometric Positioning System with Undersampling Receiver.

RMSE Root-Mean Square Error.

RoF Radio-over-Fiber.

RSS Received Signal Strength.

RX Receiver.

SC Supressed Carrier.

SNR Signal-to-Noise Ratio.

SRIPS Stochastic Radio Interferometric Positioning System.

SSMF Standard Single Mode Fiber.

STC Space-Time Code.

STRIPS Space-Time Radio Interferometric Positioning System.

TOA Time-of-Arrival.

TX Transmitter.

USRP Universal Software Radio Peripheral.

UWB Ultra-Wideband.

WLSE Weighted Least Squares Estimator.

WSN Wireless Sensor Network.

WSS Wide-Sense Stationary.

SUMMARY

Finding location plays a significant role in many applications such as car navigation systems, product tracking in the warehouse, and failure detections of the buildings. However, developing accurate positioning system for indoor areas is challenging due to multipath. Ultra-wideband (UWB) radars and super-resolution techniques are known to be robust to multipath, but they are computationally expensive. On the other hands, localization using received signal strength (RSS) and channel state information (CSI) are cost-effective but can only provide a coarse location information. Hence, it is important to consider computational complexity, implementation cost, and localization performance.

The objective of this dissertation is to develop low-complexity accurate indoor localization systems that is robust to multipath. To obtain highly accurate location information, we utilize millimeter waves (MMWs) for ranging. The MMW band around 60 GHz is recently proposed as an alternative spectrum for short-range communication systems. Existing MMW-based indoor localization systems have shown robustness to multipath and high accuracy by exploiting the characteristics of the MMWs. Yet, high computational complexity still remains as an issue. Hence, we introduce radio interferometric positioning system (RIPS) to the MMW band for indoor localization. The basic idea behind the RIPS is to calculate a range from the phase of an interference signal created by two sinusoidal signals at slightly different frequencies. The extracted interference signal is at low frequency, and thus, required receiver bandwidth is low, making the RIPS suitable for resource-limited wireless sensor networks (WSNs). In the first part of this dissertation, we design a receiver using undersampling techniques to circumvent the noise augmentation problem in

the original RIPS. We perform theoretical analysis of both the original and proposed RIPS by deriving the Cramér-Rao Lower Bounds (CRLBs) of the range and location estimates. We consider white and colored noise and corroborate the derived bounds with numerical examples. The systems are also implemented on National Instruments' Universal Software Radio Peripherals (NI USRPs) for experimental analysis. To reduce the localization complexity of the RIPS, we develop a ranging model using two transmitters and a receiver. Asynchronous RIPS (ARIPS) uses a dual-tone signal to cope with carrier frequency offsets (CFOs) and integer ambiguity issues. The second part of this dissertation focuses on designing indoor localization systems using MMWs. The RIPS cannot be directly applied for indoor localization as it is highly sensitive to multipath, and the MMW signaling causes unavoidable integer ambiguities. Hence, we employ space-time coding (STC) in the ranging signal of the proposed systems. The efficiency of the proposed systems is confirmed through simulations and experiments.

CHAPTER I

INTRODUCTION

Localization has wide range of applications including monitoring, navigation, and tracking [38, 67, 47], and consequently, a localization system has to be designed to fulfill the requirements specifically for a particular application. For example, few meters of accuracy is sufficient for localization in outdoor [46, 58] whereas much higher accuracy in the order of centimeters is required in indoor environments [27]. Computational complexity becomes especially important when localizing wireless sensor networks (WSNs) [34, 43] as sensor nodes are typically resource-limited [2]. Amount of time required for localization also has to be considered as it directly leads to latency, which becomes critical in real-time tracking systems [48, 17].

For indoor applications, finding accurate location is especially challenging as environments are typically rich in multipath [67, 31]. Well-known Global Positioning System (GPS) fails to work in indoor environments because of a lack of line-of-sight (LOS) between the user and the satellites [49]. Even if the GPS signal reaches indoor and the environment is free of multipath, few meters of positioning accuracy provided by the GPS is not enough for some indoor geolocation applications such as location-based authentications [36, 47]. Moreover, when the localization is performed at mobile units, computational complexity of the localization system has to be kept low [27].

Deployment and implementation costs are also important to consider. One approach to reduce the cost is to use measurements that are already available for other purposes. Example of such measurements is received signal strength (RSS), which is readily available in many commercial devices [33]. In the RSS-based techniques, the

RSS measurements are used to calculate a range based on a power attenuation or by comparing measured RSS with fingerprints obtained prior to localization [71, 4, 5]. Similarly, WiFi signals and channel state information (CSI) are proposed for ranging in [71, 72]. Unfortunately, requirement for offline survey leads to additional deployment cost, and signal instability limits the system accuracy.

Another approach is to employ time-based localization techniques. For instance, a time-of-arrival (TOA) is measured by detecting the time instance of when the signal arrives at the receiver [32, 10]. With impulse signals, the receiver can resolve the first from multiple arriving signals, making these techniques robust to multipath. Wideband signals are required to obtain precise time measurements, but typical commercial devices are band-limited. Hence, realizing impulse signals with high resolution in time may be challenging. In [26], the first arriving path is detected in the frequency domain by sounding the channel at multiple frequencies. Super-resolution techniques used to differentiate multiple paths require high computational complexity, and the complexity increases as a number of paths increases [33].

Recently, positioning systems using millimeter waves (MMWs) are developed to accurately find the location in indoor environments under multipath [68, 30, 6, 13]. The MMW is a signal around 3-300 GHz band, and this unlicensed band is considered as an alternative spectrum to alleviate the heavy traffic in a conventional radio-frequency (RF) spectrum [37, 55]. Experiments have shown promising performance of existing MMW-based indoor localization systems [68, 30, 6, 13], but they require high computational complexity. In this disseration, we employ radio interferometric positioning system (RIPS) [29] to develop indoor positioning systems with high accuracy but at low complexity.

The RIPS is a range-based system, where a location is calculated based on a set of range measurements. Two transmitters transmit sinusoidal signals at slightly different frequencies to cause interference. The phase is measured from a low-frequency signal

obtained with a square-law device that is available at low cost. Then, a range is calculated by taking the phase difference at two receivers. Low-computational complexity of the RIPS makes it suitable for resource-limited sensor nodes [2], and its potential to yield high accuracy has attracted interest to adopt the RIPS in various applications including indoor localizations [22, 7, 73]. However, one of the main drawbacks of the RIPS is its sensitivity to multipath [70, 22]. When the channel is faded due to multipath, the received signal contains an unknown phase shift that the receivers cannot resolve. Existing RIPS-based indoor localization systems aim to gain the robustness to multipath by compromising computational and implementation complexities. For instance, computationally-expensive super-resolution technique is used in [73], and specialized hardware is required in [7], where spinning beacons are employed to measure the Doppler shifts. In this dissertation, we combine space-time code (STC) and MMW signaling to solve the fading sensitivity of the RIPS. By exploiting the availability of large contiguous bandwidth in the MMW spectrum [37] and its channel characteristics, our proposed systems can yield highly accurate location information without compromising complexities.

1.1 Thesis Contributions

As we are concerned with both the performance and complexities, in this dissertation, we perform development, analysis, and implementation of localization systems. Important contributions of this dissertation are as follows:

- The undersampling receiver for the RIPS [52] is developed to circumvent the noise augmentation problem in the original RIPS. The performance gain of the undersampling RIPS over the original RIPS is confirmed through simulations and hardware implementations.

- Theoretical analysis on the ranging performance of the RIPS is performed by deriving Cramér-Rao Lower Bounds (CRLBs) under white and colored noise.

To facilitate the analysis, a common framework for both the undersampling RIPS and the original RIPS are developed.

- The RIPS with dual-tone signaling is developed to reduce the localization complexities, accommodate the carrier frequency offsets (CFOs), and expand the resolvable range. The robustness of the proposed asynchronous RIPS (ARIPS) [66] against the CFOs is presented through simulations.

- Space-time RIPS (STRIPS) [53] and accurate indoor positioning system (AIPS) [50] are developed from the RIPS by combining STC and MMW signaling. Robustness to the fading is corroborated by simulations, and both the systems are implemented on hardware to evaluate their feasibility and performance.

1.2 Thesis Organization

The rest of this dissertation is organized as follows. In Chapter 2, we discuss the MMW signaling for indoor localizations. Then, we provide the background of the RIPS by reviewing its system model, followed by the literature survey on existing RIPS-related work. Chapters 3 and 4 focus on the RIPS at the conventional RF spectrum. Chapter 3 presents the RIPS employing undersampling techniques [52], where we design the receiver to avoid the increase in the noise power in the original RIPS [29]. Theoretical analysis is performed on the RIPS with proposed and original receiver designs, and we derive the CRLBs of range and location estimates under white and colored noise. Numerical and experimental results are presented to confirm the efficiency of the proposed receiver. In Chapter 4, the RIPS using dual-tone signaling is developed to avoid integer ambiguity and accommodate the CFOs. We introduce a ranging model with three nodes to avoid computationally-heavy localizations in the original RIPS.

Chapters 5 and 6 focus on MMW-based indoor localization systems using STC. The system model and ranging scheme of the STRIPS [53] is presented in Chapter 5.

We compare its performance with the original RIPS and confirm its robustness against fading through simulations. Hardware implementation and experimental results are also provided. Chapter 6 presents the AIPS and consider two ranging signal models with three types of detectors. Simulation and experimental results corroborate the effectiveness of the AIPS. Conclusions of this dissertation and potential future research topics are discussed in Chapter 7.

Notations: Bold upper case letters denote matrices. Bold lower case letters denote vectors. $\mathcal{N}(\mu, \sigma^2)$ refers to a Gaussian distribution with mean μ and variance σ^2, and $\mathcal{U}(a, b)$ signifies a uniform distribution over the range $[a, b]$. Superscripts $(\cdot)^T$, $(\cdot)^H$, $(\cdot)^*$, and $(\cdot)^\dagger$ denote transpose, Hermitian transpose, complex conjugate, and pseudo-inverse, respectively. $[\cdot]_i$ denotes the ith element of the vector, and $[\cdot]_{i,j}$ denotes the element in the matrix at the ith row and jth column. The Euclidean norm is denoted as $\|\cdot\|$. We represent the modulo operation as $mod(a, b)$, where $mod(a, b) = a - b\lfloor a/b \rfloor$ with $\lfloor \cdot \rfloor$ denoting rounding down towards zero. We use $\arg\{\cdot\}$ to denote the argument of a complex number, and $\mathrm{diag}\{\cdot\}$ represents the diagonal matrix of a vector. Expected value of a random parameter is denoted as $E[\cdot]$. The element-wise multiplication of vectors is denoted with $\odot$. Throughout this dissertation, we represent the observation matrix $\mathbf{H}(\mathbf{f}) = \frac{1}{2}[\mathbf{h}_N([\mathbf{f}]_1),\ \mathbf{h}_N^*([\mathbf{f}]_1),\ ..., \mathbf{h}_N([\mathbf{f}]_K),\ \mathbf{h}_N^*([\mathbf{f}]_K)]$, where $\mathbf{h}_N(f) = [1,\ e^{j2\pi f},\ ..., e^{j2\pi f(N-1)}]^T$ and $\mathbf{f}$ is a $K \times 1$ vector consists of a set of K frequencies.

CHAPTER II

BACKGROUND

The objective of this dissertation is to develop indoor positioning systems based on the RIPS. In this chapter, we introduce the MMW for indoor localization and present examples of existing MMW-based indoor localization systems. We review the system model of the original RIPS from [29] and discuss its strengths and weaknesses. We also provide a literature survey on existing RIPS-related work and conclude the chapter with the important contributions of this dissertation.

2.1 MMWs For Indoor Localization

There is a growing interest in utilizing the MMW band for next generation communication systems [41, 55, 37], but the MMWs was in the past considered to be inadequate for wireless communications due to its high signal attenuation [14]. Assuming there is no loss in the system hardware, the Friis free space model is given as [40, p. 107]

$$P_R(d) = \frac{P_T G_T G_R}{(4\pi f d)^2} \tag{1}$$

where P_T is the transmitted power, $P_R(d)$ is the received power, G_T is the transmitter antenna gain, G_R is the receiver antenna gain, d is the distance between a transmitter and a receiver, and f is the transmission frequency. According to (1), the signal experiences more power attenuation as transmission frequency gets larger. Hence, the MMWs attenuates more than typical RF signals. Another concern using the MMWs for wireless communications is the high energy absorption level of the spectrum. The oxygen molecules absorbed as much as 98% of energy of the signals at the 60 GHz MMW region [1]. This high energy absorption level further reduce the range that the

MMW signals can cover.

However, the high power attenuation of the MMWs is recently reconsidered as an advantage for short-range communication systems. It allows high frequency reuse in the limited area and is less likely to cause interference [1]. In addition, there is a large contiguous band available in the spectrum [37] that allows transmissions of wideband signals. Furthermore, a coherence bandwidth of the channel is relatively large (in the order of MHz) as the multipath components in the band are limited [37]. In addition, with short signal wavelength, it becomes possible to develop small, low-cost antennas [1] suitable for mobile devices. These characteristics not only benefits the communication systems but also indoor localizations.

MMW-based indoor localization systems are already proposed in [37, 68, 30, 13]. Availability of a large bandwidth in the MMW spectrum allows time-based localization systems to attain extremely high time resolution with orthogonal-frequency division multiplexing (OFDM) [68, 30] and ultra-wideband (UWB) signals [6]. High time resolution in the order of nanoseconds can resolve the first arriving path from reflected signals. Also, ranging with the RSS of MMWs are proven to be effective because high path loss of MMWs leads to a strong correlation between RSS and distance [13]. However, the time-based systems [68, 30, 6] are computationally expensive, and the RSS-based approach [13] needs an offline survey to characterize the environment prior to localization. To develop low-complexity indoor localization systems with MMWs, we use the RIPS [29], the system model of which is reviewed in the following section.

2.2 Radio Interferometric Positioning System

2.2.1 System Model and Range Estimation

A ranging model of the RIPS is illustrated in Figure 1. As shown in the figure, each ranging session involves two transmitters and two receivers. When multiple receivers

are involved, we denote the distance between the kth transmitter and the mth receiver as $d_{k,m}$. The goal here is to estimate the Q-range, which is a linear combination of four distances defined as

$$q = d_{1,1} - d_{2,1} - d_{1,2} + d_{2,2}. \tag{2}$$

In each ranging session, we assume that the receivers are synchronized in time, and all the participating nodes are synchronized in frequency. Time synchronization of the transmitters is not required.

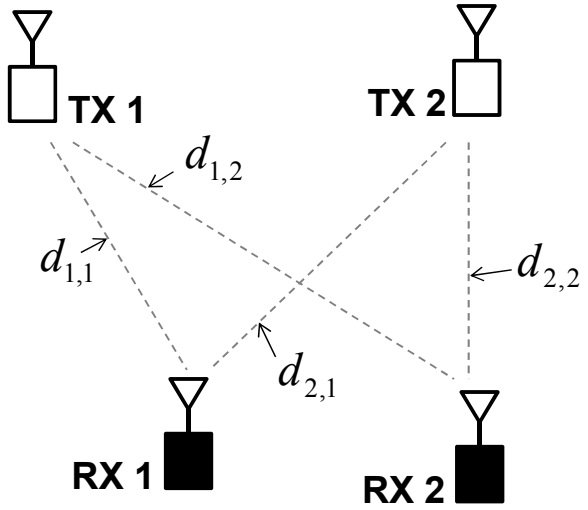

Figure 1: Ranging model of the RIPS with two transmitters and two receivers.

The transmitting signal at the kth transmitter is modeled as

$$s_k(t) = a_k \cos(2\pi f_k t + \theta_k), \tag{3}$$

where a_k, f_k and θ_k denote the amplitude, frequency and initial phase of the kth transmitting signal, respectively. Without loss of generality, assume $f_1 > f_2$ and further define $f_d = f_1 - f_2$ and $g = (f_1 + f_2)/2$. At receivers, the received signal is downconverted to an intermediate frequency (IF) by a local oscillator (LO) at the

frequency f_0. The resulting signal at the mth receiver is given as

$$\begin{aligned} r_m(t) &= \sum_{k=1}^{2} a_k \cos\left(2\pi(f_k - f_0)t - 2\pi f_k\left(\frac{d_{k,m}}{c} + t_k\right) + \theta_k\right) + v_m(t) \\ &= \sum_{k=1}^{2} a_k \cos\left(2\pi(f_k - f_0)t - \varphi_{k,m}\right) + v_m(t) \end{aligned} \tag{4}$$

where $\varphi_{k,m} = 2\pi f_k\left(\frac{d_{k,m}}{c} + t_k\right) - \theta_k$ with t_k denotes the unknown time instant when the kth transmitter started its transmission, c is a speed of light, and $v_m(t)$ is an additive noise.

In the RIPS, a square-law device is used at the receiver. The signal is first filtered with a band-pass filter (BPF) to remove any noise in the band outside of interest. Then, the received signal $r_m(t)$ in (4) is squared as

$$\begin{aligned} r_m^2(t) =& \sum_{k=1}^{2} a_k^2 \cos^2\left(2\pi(f_k - f_0)t - \varphi_{k,m}\right) \\ &+ 2a_1a_2 \cos\left(2\pi(f_1 - f_0)t - \varphi_{1,m}\right)\cos\left(2\pi(f_2 - f_0)t - \varphi_{2,m}\right) + \tilde{v}_m(t) \\ =& \frac{a_1^2 + a_2^2}{2} + \frac{1}{2}\sum_{k=1}^{2} a_k^2 \cos\left(4\pi(f_k - f_0)t - 2\varphi_{k,m}\right) \\ &+ a_1a_2 \cos\left(4\pi(g - f_0)t - \varphi_{1,m} - \varphi_{2,m}\right) \\ &+ a_1a_2 \cos\left(2\pi f_d t - \phi_m\right) + \tilde{v}_m(t), \end{aligned} \tag{5}$$

where $\tilde{v}_m(t)$ is an aggregated noise and $\phi_m = \varphi_{1,m} - \varphi_{2,m}$. Hence, the output of the square-law device contains the frequency components at $\pm 2(f_k - f_0)$, $\pm 2(g - f_0)$ and $\pm f_d$ as well as DC components. By designing the parameters as $f_d \ll f_k - f_0$, we remove the frequency components beyond f_d with a low-pass filter (LPF). Further removing the DC component, we obtain a low-frequency differential signal expressed as

$$y_m(t) = a_1a_2 \cos\left(2\pi f_d t - \phi_m\right) + \widetilde{v}_m(t). \tag{6}$$

Notice that the phase difference at the two receivers can be rewritten as

$$\begin{aligned}\phi_1 - \phi_2 =& \frac{2\pi}{c}\left\{g(d_{1,1} - d_{2,1} - d_{1,2} + d_{2,2}) + \frac{f_d}{2}(d_{1,1} + d_{2,1} - d_{1,2} - d_{2,2})\right\} \\ =& \frac{2\pi}{c}\left\{g \cdot q + \frac{f_d}{2}(d_{1,1} + d_{2,1} - d_{1,2} - d_{2,2})\right\},\end{aligned} \tag{7}$$

where $q = d_{1,1} - d_{2,1} - d_{1,2} + d_{2,2}$ is the Q-range as defined in (2). From $f_d \ll g$, the second term is considered negligibly smaller than the first term. As a result, ϕ_m and the Q-range are approximately related as

$$q \approx \frac{c}{2\pi g}\left(\phi_1 - \phi_2\right). \tag{8}$$

2.2.2 Location Estimation

Although the ranging scheme of the RIPS is fairly simple, localization using the Q-range measurements is a complicated task. The Q-range is a linear combination of four distances as shown in (2), and its relationship with the location of any of the participating node is nonlinear. The genetic algorithm (GA) is used [29] to localize the network as a whole, and [35] proposes to use the RSS measurements as the initial conditions for the GA. In [28], a probabilistic model of the noise is employed to perform the distributed localization and to support sparse network topologies. The complexity of the Q-range-based localization algorithms is analyzed in [15], and the authors proposed the distributive algorithm suitable for large WSNs.

To simplify the localization with the Q-range measurements, the collaborative localization method is discussed in [21]. The method estimates the location of an unknown node based on two independent Q-range measurements, where locations of the rest of the nodes are known. Similar to [21] is the hyperbolic positioning [19, 62], where a position of an unknown node is determined by finding the intersection of two hyperbolas. In this dissertation, we localize a node one at a time and reduce the localization complexity by converting the Q-range into the range-difference (RD) measurements. Details are found in Section 3.1.2. Furthermore, in Chapter 4, we

introduce a ranging model with three nodes to measure the RD directly, and thus complex Q-range-based localizations are avoided.

2.3 Literature Survey on RIPS-Related Work

Because of its flexibility and low complexity, the RIPS has been adopted for various scenarios. One of which is tracking of mobile nodes [18, 17, 3]. In [18], a mobile node tracking system based on the RIPS called inTrack is proposed to analyze the effects of velocity and moderate outdoor multipath on the system performance. The system is further improved in [17] by incorporating a Doppler shift into location estimation. Their experimental results show a mean absolute error (MAE) of 37 cm. Also taking a Doppler shift into account and using an extended Kalman filter, a tracking system based on the RIPS yields the MAE of 1.68 m in a field test [3]. Another extension of the RIPS is its implementation at a different frequency band. Formerly, the RIPS is implemented on CC1000 RF transceiver at the frequency band below 1 GHz [29]. However, in [11, 12], the RIPS is implemented on CC2430 transceivers, which operate at 2.4 GHz. Due to lack of fine-frequency tuning capability of the CC2430 platform, an inherent offset of LOs is used for the frequency difference, resulting in the MAE of $1.5 - 2$ meters [11]. Using the same platform, a stochastic RIPS (SRIPS) [12] is proposed to improve the accuracy at 2.4 GHz by taking into account some stochastic properties of Q-range measurements.

One of the major issue to consider in the RIPS is the integer ambiguity. Since the range is estimated by unwrapping the phase, a resolvable range without ambiguities in the RIPS is determined by the wavelength of a carrier wave. In other words, when the RIPS operates at the high frequency band, the Q-range is likely to be larger than the carrier wavelength, which results in unknown integer in the phase measurements. There are mainly two existing approaches to perform localizations with ambiguous

measurements. First approach resolves the ambiguities in the Q-range prior to localization by using methods such as the maximum likelihood estimator (MLE) [23], the Chinese remainder theorem (CRT) [61, 60], or lattice reduction method [25]. Second approach directly uses ambiguous measurements to perform the localization [24, 9]. In both approaches, multiple transmissions at different frequencies are required. To avoid excess power consumptions in resource-limited devices, a number of transmissions should be kept minimal. Consequently, the transmitting signal model can be modified to avoid the ambiguous measurements. In [73, 74], linear frequency modulation (LFM) waves are employed to expand the resolvable range so that ambiguities are unlikely to occur. However, the LFM-based RIPS requires perfect frequency synchronization among the nodes, and this requirement may be demanding for cost-limited sensors. Frequency synchronization is required in the original RIPS as well [70], and frequencies among all the nodes are synchronized by exchanging messages prior to ranging [29].

Sensitivity to multipath is another concern in the original RIPS [29]. Authors in [70, 22] shows that the localization accuracy of the RIPS degrades by few meters under multipath. In [65], dual-tone RIPS (DRIPS) using dual-tone signaling is proposed to combat the fading. With undersampling techniques, the uDRIPS [64] further enhances the system performance and improves the flexibility in parameter design. Moreover, by simultaneously transmitting the ranging signals from anchor nodes, the DRIPS and the uDRIPS directly localize the target node, thereby complex node-scheduling is avoided and latency is reduced. To obtain the robustness to fading, the frequency difference less than few kHz is required, and high signal-to-noise ratio (SNR) is required for the systems to reach submeter accuracy. The similar approach is adopted to the RIPS in [73] by transmitting at multiple frequencies. The basic idea comes from [26], where super-resolution techniques are used to identify the first arriving path from a set of phase measurements. The proposed scheme requires

a number of frequencies transmitted to be greater than a number of paths in the environment. Naturally, required bandwidth increases with a number of paths, and similarly to [26], the system complexity remains as an issue.

In this dissertation, we first perform theoretical and experimental analysis on the RIPS. Then, we investigate different receiver design, and ranging model to cope with some drawbacks in the RIPS already described. Using the results from these investigations, we develop indoor localization systems that is robust to the multipath. By employing the STC, the proposed systems can avoid integer ambiguities despite of transmissions at the millimeter carrier wavelength. Furthermore, with the STC, an unknown phase offset due to fading is canceled, and accurate range information is achieved under multipath. Using the ranging model with three nodes, the localization complexity is reduced from that of the original RIPS. The details of the proposed systems and performance evaluations are found in Chapters 5 and 6.

CHAPTER III

RADIO INTERFEROMETRIC POSITIONING SYSTEM USING UNDERSAMPLING TECHNIQUES

In this section, we present the undersampling receiver for the RIPS. The original RIPS uses a square-law detector to extract a low-frequency differential signal, but a squaring operation increases the noise power [52]. Also, the estimated Q-range in the original RIPS contains an approximation error as shown in (7). For this approximation to be valid, two transmitting frequencies have to be close, which limits the choice of parameters in the RIPS. For the rest of this disseration, we follow the notations in [52, 54] and denote the original RIPS that employs a square-law detector as the RIPS-sq and the RIPS with undersampling receivers as the RIPS-u. The RIPS-u and the RIPS-sq share a common ranging model illustrated in Figure 1, and the transmitter model is as described in (3). We present the receiver model of the RIPS-u in Section 3.1. To facilitate the analysis of the RIPS-sq, a mathematical framework similar to that of the RIPS-u is developed for the RIPS-sq. Theoretical analysis is presented in Section 3.2, where we derive the CRLBs of Q-range location estimates for both the RIPS-u and the RIPS-sq. We consider the cases where the additive noise is white and colored, and we propose methods to enhance the ranging performance when the noise correlation information is available. Numerical results are presented in Section 3.2.3 to corroborate the derived bounds and to confirm the efficiency of the proposed RIPS-u. Furthermore, we implement both system on hardware, and experimental setup and results are presented in Section 3.3.

3.1 System Model

The RIPS-u share a same transmitter model with the RIPS-sq described in Section 2.2. Hence, two receiver nodes in Figure 1 are assumed to be synchronized in time, and frequency synchronization is assumed at all the participating nodes. The receiver design of the RIPS-u is illustrated as a block diagram in Figure 2. In the RIPS-u, the received signal $r_m(t)$ in (4) is directly sampled. Sampling $r_m(t)$ at the rate f_s, we obtain

$$r_m[n] = a_1 \cos\left(2\pi \bar{f}_1 n - \varphi_{1,m}\right) + a_2 \cos\left(2\pi \bar{f}_2 n - \varphi_{2,m}\right) + v_m[n],\ n = 0, 1, ..., N-1, \quad (9)$$

where $\bar{f}_k = (f_k - f_0)/f_s$. Vertically stacking N samples collected at the mth receiver, we can express the sampled received signal $r_m[n]$ in a matrix-vector form as

$$\mathbf{r}_m = \mathbf{H}(\mathbf{f})\mathbf{z}_m + \mathbf{v}_m, \quad (10)$$

where

$$\begin{aligned}
\mathbf{r}_m &= [r_m[0],\ r_m[1],\ ...,\ r_m[N-1]]^T, \\
\mathbf{v}_m &= [v_m[0],\ v_m[1],\ ...,\ v_m[N-1]]^T, \\
\mathbf{H}(\mathbf{f}) &= \frac{1}{2}[\mathbf{h}_N(\bar{f}_1),\ \mathbf{h}_N^*(\bar{f}_1),\ \mathbf{h}_N(\bar{f}_2),\ \mathbf{h}_N^*(\bar{f}_2)], \\
\mathbf{h}_N(f) &= [1,\ e^{j2\pi f},\ ...,\ e^{j2\pi f(N-1)}]^T, \\
\mathbf{f} &= [\bar{f}_1,\ \bar{f}_2], \\
\mathbf{z}_m &= [a_1 e^{-j\varphi_{1,m}},\ a_1 e^{j\varphi_{1,m}},\ a_2 e^{-j\varphi_{2,m}},\ a_2 e^{j\varphi_{2,m}}]^T.
\end{aligned} \quad (11)$$

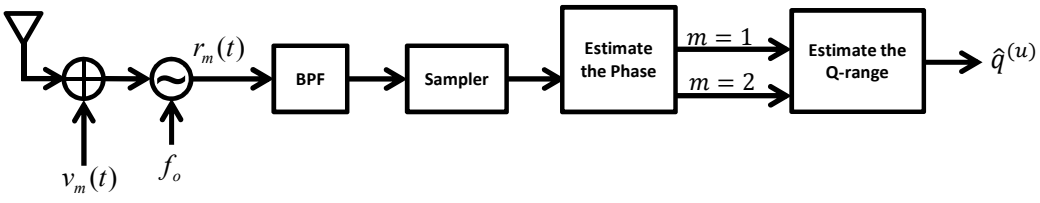

Figure 2: Block diagram of the receivers in the RIPS-u.

Since we assume that the frequencies are synchronized among all the participating

nodes, the matrix $\mathbf{H}(\mathbf{f})$ is accurately constructed at the receivers. Employing least-squares estimator (LSE), we estimate the phase vector $\mathbf{z}_m$ as

$$\widehat{\mathbf{z}}_m = \mathbf{H}^{\dagger}(\mathbf{f})\mathbf{r}_m. \tag{12}$$

Recall that $\varphi_{k,m} = 2\pi f_k(d_{k,m}/c + t_k) - \theta_k$. The difference between the aggregated phase corresponding to the kth transmitter at two receivers is

$$\begin{aligned} \varphi_{k,1} - \varphi_{k,2} =& 2\pi f_k \left(\frac{d_{k,1}}{c} + t_k\right) - \theta_k - 2\pi f_k \left(\frac{d_{k,2}}{c} + t_k\right) + \theta_k \\ =& 2\pi f_k \frac{d_{k,1} - d_{k,2}}{c}. \end{aligned} \tag{13}$$

Notice that nuisance terms such as t_k and θ_k are successfully canceled out, and we are left with range information. From (13), the relationship between the aggregated phase and the Q-range $q = d_{1,1} - d_{2,1} - d_{1,2} + d_{2,2}$ is given as

$$q = \frac{c}{2\pi}\left(\frac{\varphi_{1,1} - \varphi_{1,2}}{f_1} - \frac{\varphi_{2,1} - \varphi_{2,2}}{f_2}\right), \tag{14}$$

and thus, the Q-range is estimated in the RIPS-u as

$$\widehat{q}^{(u)} = \frac{c}{2\pi f_1}\arg\left\{\left([\widehat{\mathbf{z}}_1]_1^* + [\widehat{\mathbf{z}}_1]_2\right)\left([\widehat{\mathbf{z}}_2]_1 + [\widehat{\mathbf{z}}_2]_2^*\right)\right\} - \frac{c}{2\pi f_2}\arg\left\{\left([\widehat{\mathbf{z}}_1]_3^* + [\widehat{\mathbf{z}}_1]_4\right)\left([\widehat{\mathbf{z}}_2]_3 + [\widehat{\mathbf{z}}_2]_4^*\right)\right\}. \tag{15}$$

3.1.1 Ranging in the RIPS-sq

In [29], the phase difference is estimated analogously with peak detection. To compare the RIPS-u and the RIPS-sq theoretically, we develop the mathematical framework for the RIPS-sq analogous to that of the RIPS-u and present the LSE-based Q-range estimator.

The block diagram of the receivers in the RIPS-sq is shown in Figure 3. Sampling the low-frequency differential signal $y_m(t)$ in (6) at the rate $f_s > 2f_d$, we obtain

$$y_m[n] = a_1 a_2 \cos\left(2\pi \bar{f}_d n - \phi_m\right) + \widetilde{v}_m[n],\ n = 0, 1, ..., N-1, \tag{16}$$

where $\bar{f}_d = f_d/f_s$, and $\widetilde{v}_m[n]$ is the sampled aggregated noise. Stacking N samples collected at the mth receiver vertically, we arrive at

$$\mathbf{y}_m = \mathbf{H}(\bar{f}_d)\widetilde{\mathbf{z}}_m + \widetilde{\mathbf{v}}_m, \tag{17}$$

where

$$\begin{aligned} \mathbf{y}_m =& [y_m[0],\ y_m[1],\ ...,\ y_m[N-1]]^T, \\ \widetilde{\mathbf{v}}_m =& [\widetilde{v}_m[0],\ \widetilde{v}_m[1],\ ..., \widetilde{v}_m[N-1]]^T, \\ \widetilde{\mathbf{z}}_m =& a_1 a_2 [e^{j\phi_m},\ e^{-j\phi_m}]^T. \end{aligned} \tag{18}$$

Similarly to (12), we estimate the phase vector $\widetilde{\mathbf{z}}_m$ with LSE as

$$\widehat{\widetilde{\mathbf{z}}}_m = \mathbf{H}^{\dagger}(\bar{f}_d)\mathbf{y}_m. \tag{19}$$

According to the relationship given in (7), the Q-range estimator for the RIPS-sq is derived as

$$\widehat{q}^{(sq)} = \frac{c}{2\pi g} \arg\left\{ \left(\left[\widehat{\widetilde{\mathbf{z}}}_1\right]_1^* + \left[\widehat{\widetilde{\mathbf{z}}}_1\right]_2 \right) \left(\left[\widehat{\widetilde{\mathbf{z}}}_2\right]_1 + \left[\widehat{\widetilde{\mathbf{z}}}_2\right]_2^* \right) \right\}. \tag{20}$$

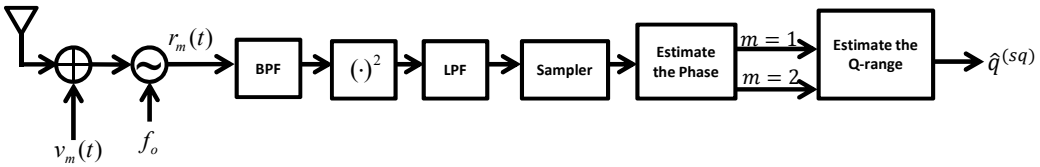

Figure 3: Block diagram of the receivers in the RIPS-sq.

3.1.2 Localization with Q-range measurements

As described in Section 2.2.2, the Q-range-based localization tends to be complicated due to nonlinearity of the Q-range w.r.t. node locations. It should be noted, however, that when locations of three out of four nodes are known, the Q-range can be converted to the RD [20]. Because the RD only involves two distances, RD measurements is easier to handle than the Q-range. The RD-based localization techniques are already available in [56, 63].

Let us describe how we employ the RD-based algorithms with Q-range measurements. In Figure 1, assume that TX2, RX1, and RX2 are at known positions, and TX1 is the target node to be localized. We choose TX1 as the target node because of the time synchronization requirement at the receivers. In such a case, the last two terms in the Q-range $q = d_{1,1} - d_{1,2} - d_{2,1} + d_{2,2}$ can be pre-calculated. Moving the unknown terms to the left-hand side (LHS), we arrive at the RD measurement between TX1 and two receivers as

$$d_{1,1} - d_{1,2} = q + d_{2,1} - d_{2,2}. \tag{21}$$

Let us denote the coordinates of the target node and the mth receiver as $\mathbf{x}$ and $\mathbf{x}_m$, respectively. Choosing the first receiver node as the origin of the coordinate system ($\mathbf{x}_1 = \mathbf{0}$), (21) can be rewritten as

$$\|\mathbf{x}\| - \|\mathbf{x} - \mathbf{x}_2\| = R, \tag{22}$$

where $R = q + d_{2,1} - d_{2,2}$ is the right-hand side (RHS) of (21). Rearranging the terms and squaring both sides as

$$\|\mathbf{x} - \mathbf{x}_2\|^2 = \left(\|\mathbf{x}\| - R\right)^2, \tag{23}$$

we arrive at

$$2R\|\mathbf{x}\| - 2\mathbf{x}_2^T\mathbf{x} = R^2 - \|\mathbf{x}_2\|^2, \tag{24}$$

where the unknown terms are collected on the LHS, and the known terms are on the RHS. When we consider a 2D scenario, the dimension of $\mathbf{x}$ is 2. Keeping $\mathbf{x}_1$ fixed as the reference node over multiple RD measurements, we have $\mathbf{x}$ and $\|\mathbf{x}\|$ as unknowns. Hence, with at least three independent RD measurements, we have a set of linear equations to solve the location vector $\mathbf{x}$. In this dissertation, we employ the constrained-LSE, and details are found in [56].

3.1.3 Parameter Design

Integer Ambiguity According to (20), the Q-range estimates in the RIPS-sq is free of integer ambiguity when $|q| < c/2g$. Throughout this dissertation, we refer to this upper-bound as resolvable range. Since the resolvable range of the RIPS-sq depends on g, when the signal is transmitted at high frequency, it becomes more likely for integer ambiguity to occur. In the RIPS-u, from (15) we require $|d_{k,1} - d_{k,2}| < c/2f_k$ for $k = 1, 2$. When $f_d \ll g$ such that $g \approx f_1 \approx f_2$, then the resolvable range of the RIPS-u and the RIPS-u becomes approximately the same.

Sampling Rate Although the maximum frequency of the received signal $r_m(t)$ is $\bar{f}_1$, which is larger than f_d, the received signal can be sampled below $2\bar{f}_1$. When $f_s < 2(f_k - f_0)$, frequencies of the sampled signal are aliased. For accurate phase estimation, we need independent columns in $\mathbf{H}(\mathbf{f})$. Hence, we need $\mathbf{h}_N(\bar{f}_1)$ and $\mathbf{h}_N(\bar{f}_2)$ to be independent as

$$\begin{aligned} \mathbf{h}_N^T(\bar{f}_1)\mathbf{h}_N^*(\bar{f}_2) &= \sum_{n=0}^{N-1} e^{j2\pi\frac{f_1-f_0}{f_s}n} e^{-j2\pi\frac{f_2-f_0}{f_s}n} \\ &= \sum_{n=0}^{N-1} e^{j2\pi\frac{f_d}{f_s}n} \approx 0. \end{aligned} \tag{25}$$

The last condition is satisfied when $mod(f_d, f_s) \neq 0, \frac{1}{2}$. When the condition is violated, aliased frequencies in the sampled signal are too close that individual phase estimates cannot be obtained. In [52], it is shown that as long as two aliased frequencies are well separated, we can estimate the phase accurately at two tones even when $f_s < f_k - f_0$.

Frequency Difference One of the advantages of the RIPS-u over the RIPS-sq is that it has more flexibility in choosing parameters. In (20), the Q-range estimator in the RIPS-u does not have an approximation error. Moreover, the received signal is directly sampled without extracting a low-frequency differential signal. Hence, we no longer have a constraint $f_d \ll f_s$. This is meritorious when devices lacks fine

frequency-tuning capability, such as in CC2430 [11], and small f_d cannot be realized.

3.2 Theoretical Analysis

As a range-based system, the positioning accuracy of the RIPS is highly dependent on the accuracy of estimated Q-ranges. Yet, existing theoretical analysis related to the RIPS concerns with the performance of the Q-range based localization schemes [15, 75]. In [15], authors analyze how errors in range estimates propagate to node location estimates by modeling a range estimation error as Gaussian. Authors in [75] derive the performance bound of localization estimates in the RIPS by deriving the method of interval error (MIE). Here, they also assume that the error in range estimates follows a Gaussian distribution. However, in the RIPS, the range is calculated from the phase, and the noise of the phase estimates can be approximated as Gaussian only when the noise is additive white Gaussian noise (AWGN) and the SNR is relatively high [59]. Hence, the results from [15, 75] are not applicable when the SNR is low. Moreover, the signal noise may not be white due to filtering at receivers, which makes the Gaussian approximation invalid even when the SNR is high. Consequently, it is important to evaluate the localization performance of the RIPS through its ranging performance.

3.2.1 Cramér-Rao Lower Bounds of Q-range Estimates

We derive the CRLBs for the Q-range estimates in the RIPS-u and the RIPS-sq and consider the case when the additive noise $v_m(t)$ is white and colored as the correlation of the noise is inevitable due to filtering in practical scenarios. In the following analysis, we assume that the noise is circularly symmetric Gaussian. When the noise is colored, we use the first-order autoregressive (AR1) model, which is expressed as

$$v_m[n] = \rho v_m[n-1] + u_m[n], \tag{26}$$

where $u_m[n] \sim \mathcal{N}(0, \kappa_m^2)$ and ρ is a parameter such that $|\rho| < 1$ since we assume that $v_m[n]$ is wide-sense stationary (WSS).

Ranging performance of the RIPS-u Since we assume that $v_m[n]$ is circularly symmetric Gaussian, the Fischer information matrix (FIM) of the phase $\boldsymbol{\varphi}_m = [\varphi_{1,m},\ \varphi_{2,m}]^T$ estimated in the RIPS-u is given as [57]

$$\mathbf{F}(\boldsymbol{\varphi}_m) = \mathbf{A}\mathbf{P}^T\mathbf{K}_m^{-1}\mathbf{P}\mathbf{A}, \tag{27}$$

where

$$\begin{aligned} \mathbf{A} =& \text{diag}\{a_1, a_2\}, \\ \mathbf{K}_m \triangleq& E\left\{(\mathbf{v}_m - E(\mathbf{v}_m))(\mathbf{v}_m - E(\mathbf{v}_m))^T\right\}, \\ \mathbf{P} =& [\mathbf{p}_N(\bar{f}_1)\ \mathbf{p}_N(\bar{f}_2)], \\ \mathbf{p}_N(f) =& [0,\ \sin(2\pi f),\ ...,\ \sin(2\pi f(N-1))]^T. \end{aligned} \tag{28}$$

When $v_m[n]$ is the AWGN with zero mean and variance σ_m^2, the covariance matrix $\mathbf{K}_m$ in (27) is a diagonal matrix

$$\mathbf{K}_m^{white} = \sigma_m^2\mathbf{I}_N. \tag{29}$$

When $v_m[n]$ is colored that follows the AR1 model, we employ the autocorrelation function (ACF) of the AR1 process derived in Appendix A and express the covariance matrix $\mathbf{K}_m$ as

$$\left[\mathbf{K}_m^{AR1}\right]_{n,l} = \frac{\kappa_m^2\rho^{|n-l|}}{1-\rho^2}. \tag{30}$$

We obtain the CRLB of the phase $\varphi_{k,m}$ along its diagonal of the inverse of (27) as

$$CRLB(\varphi_{k,m}) = \left[\mathbf{F}(\boldsymbol{\varphi}_m)^{-1}\right]_{k,k}. \tag{31}$$

From the relationship between the Q-range and $\varphi_{k,m}$ given in (13), the CRLB for the Q-range estimates in the RIPS-u is calculated as

$$CRLB(q^{(u)}) = \sum_{k=1}^{2}\left(\frac{c}{2\pi f_k}\right)^2\left\{CRLB(\varphi_{k,1}) + CRLB(\varphi_{k,2})\right\}. \tag{32}$$

Ranging performance of the RIPS-sq Deriving the CRLB for the Q-range estimates in the RIPS-sq is not as straightforward as in the RIPS-u since we first need to model the aggregated noise. To ease the derivation, let us assume the aggregated noise $\widetilde{\mathbf{v}}_m$ as circularly symmetric Gaussian. Then, the CRLB of the aggregated phase of a low-frequency differential signal in the RIPS-sq ϕ_m can be expressed as

$$CRLB(\phi_m) = \frac{1}{(a_1 a_2)^2 \mathbf{p}_N^T(\bar{f}_d)\widetilde{\mathbf{K}}_m^{-1}\mathbf{p}_N(\bar{f}_d)}, \tag{33}$$

where

$$\widetilde{\mathbf{K}}_m \triangleq E\left[(\widetilde{\mathbf{v}}_m - E(\widetilde{\mathbf{v}}_m))(\widetilde{\mathbf{v}}_m - E(\widetilde{\mathbf{v}}_m))^T\right] = E\left[\widetilde{\mathbf{v}}_m\widetilde{\mathbf{v}}_m^T\right] - E\left[\widetilde{\mathbf{v}}_m\right]E\left[\widetilde{\mathbf{v}}_m\right]^T \tag{34}$$

is the covariance matrix of the aggregated noise $\widetilde{\mathbf{v}}_m$. From (33) and the relationship between ϕ_m and the Q-range given in (7), the CRLB of the Q-range estimates in the RIPS-sq is calculated as

$$CRLB(q^{(sq)}) = \left(\frac{c}{2\pi g}\right)^2 (CRLB(\phi_1) + CRLB(\phi_2)). \tag{35}$$

Now, let us investigate the covariance matrix $\widetilde{\mathbf{K}}_m$ of the aggregated noise $\widetilde{v}_m[n]$. The vector $\widetilde{\mathbf{v}}_m$ can be expressed as

$$\widetilde{\mathbf{v}}_m = 2\mathbf{D}_m\mathbf{v}_m + \mathbf{w}_m, \tag{36}$$

where

$$\begin{aligned}\mathbf{D}_m =& \text{diag}\left\{s_m[0],\ s_m[1],\ ...,\ s_m[N-1]\right\},\\ s_m[n] =& \sum_{k=1}^{2} a_k \cos\left(2\pi\bar{f}_k n - \varphi_{k,m}\right),\\ \mathbf{w}_m =& \mathbf{v}_m \odot \mathbf{v}_m.\end{aligned} \tag{37}$$

Substituting (36) into (34), we arrive at

$$\begin{aligned}\widetilde{\mathbf{K}}_m \triangleq& E\left[(\widetilde{\mathbf{v}}_m - E\left[\widetilde{\mathbf{v}}_m\right])(\widetilde{\mathbf{v}}_m - E\left[\widetilde{\mathbf{v}}_m\right])^T\right]\\ =& 4\mathbf{D}_m\mathbf{K}_m\mathbf{D}_m + \mathbf{D}_m E\left[\mathbf{v}_m\mathbf{w}_m^T\right] + E\left[\mathbf{w}_m(\mathbf{D}_m\mathbf{v}_m)^T\right] + E\left[\mathbf{w}_m\mathbf{w}_m^T\right] - E\left[\widetilde{\mathbf{v}}_m\right]E\left[\widetilde{\mathbf{v}}_m\right]^T.\end{aligned} \tag{38}$$

In the following, we find the expressions for $\widetilde{\mathbf{K}}_m$ term-by-term under white and colored noise.

1) Covariance matrix of the aggregated white noise

Let us skip the first term for now and start with the second term in (38). Since the odd moments of a zero-mean Gaussian random variable are zero, it is straight forward that the second and third terms in (38) are zero matrices as

$$\left[\mathbf{D}_m E\left[\mathbf{v}_m \mathbf{w}_m^T\right]\right]_{n,l} = s_m[n] E\left[v_m[n] v_m^2[l]\right] = 0, \ \forall n, l, \tag{39}$$

and

$$\left[E\left[\mathbf{w}_m (\mathbf{D}_m \mathbf{v}_m)^T\right]\right]_{n,l} = s_m[l] E\left[v_m^2[n] v_m[l]\right] = 0, \ \forall n, l. \tag{40}$$

The fourth term in (38) consists of the even moments of Gaussian random variables as

$$E\left[\mathbf{w}_m \mathbf{w}_m^T\right] = 2\sigma_m^4 \mathbf{I}_N + \sigma_m^4 \mathbf{1}_N \mathbf{1}_N^T. \tag{41}$$

From (36), we observe that the expectation of the aggregated white noise is

$$E\left[\widetilde{\mathbf{v}}_m\right] = 2\mathbf{D}_m E\left[\mathbf{v}_m\right] + E\left[\mathbf{v}_m \odot \mathbf{v}_m\right] = \sigma_m^2 \mathbf{1}_N, \tag{42}$$

and thus, the last term in (38) is

$$E\left[\widetilde{\mathbf{v}}_m\right] E\left[\widetilde{\mathbf{v}}_m\right]^T = \sigma_m^4 \mathbf{1}_N \mathbf{1}_N^T. \tag{43}$$

Let us now come back to the first term in (38). Due to $\mathbf{D}_m$, the term varies w.r.t. time. In other words, $\widetilde{\mathbf{v}}_m$ is not WSS. From the assumptions made in the CRLB given in (35), we approximate $\widetilde{\mathbf{v}}_m$ as circularly symmetric Gaussian by taking the expectation of $\widetilde{\mathbf{K}}_m$ over a random parameter. We begin by rewriting the first term in (38) as

$$4\mathbf{D}_m \mathbf{K}_m \mathbf{D}_m = 4\mathbf{\Gamma} \odot \mathbf{K}_m, \tag{44}$$

where $[\mathbf{\Gamma}_m]_{n,l} = s_m[n]s_m[l]$. The element of $\mathbf{\Gamma}_m$ at the nth row and lth column is rewritten explicitly as

$$\begin{aligned}
[\mathbf{\Gamma}_m]_{n,l} =& \left(\sum_{k=1}^{2} a_k \cos\left(2\pi \bar{f}_k n + \varphi_{k,m}\right)\right)\left(\sum_{k=1}^{2} a_k \cos\left(2\pi \bar{f}_k l + \varphi_{k,m}\right)\right) \\
=& a_1^2 \cos\left(2\pi \bar{f}_1 n + \varphi_{1,m}\right)\cos\left(2\pi \bar{f}_1 l + \varphi_{1,m}\right) \\
&+ a_2^2 \cos\left(2\pi \bar{f}_2 n + \varphi_{2,m}\right)\cos\left(2\pi \bar{f}_2 l + \varphi_{2,m}\right) \\
&+ a_1 a_2 \cos\left(2\pi \bar{f}_1 n + \varphi_{1,m}\right)\cos\left(2\pi \bar{f}_2 l + \varphi_{2,m}\right) \\
&+ a_1 a_2 \cos\left(2\pi \bar{f}_1 l + \varphi_{1,m}\right)\cos\left(2\pi \bar{f}_2 n + \varphi_{2,m}\right) \\
=& \frac{a_1^2}{2}\left\{\cos\left(2\pi \bar{f}_1 (n+l) + 2\varphi_{1,m}\right) + \cos\left(2\pi \bar{f}_1 (n-l)\right)\right\} \\
&+ \frac{a_2^2}{2}\left\{\cos\left(2\pi \bar{f}_2 (n+l) + 2\varphi_{2,m}\right) + \cos\left(2\pi \bar{f}_2 (n-l)\right)\right\} \\
&+ \frac{a_1 a_2}{2}\left\{\cos\left(2\pi(\bar{f}_1 n + \bar{f}_2 l) + \varphi_{1,m} + \varphi_{2,m}\right)\right. \\
&\qquad \left. + \cos\left(2\pi(\bar{f}_1 n - \bar{f}_2 l) + \varphi_{1,m} - \varphi_{2,m}\right)\right\} \\
&+ \frac{a_1 a_2}{2}\left\{\cos\left(2\pi(\bar{f}_1 l + \bar{f}_2 n) + \varphi_{1,m} + \varphi_{2,m}\right)\right. \\
&\qquad \left. + \cos\left(2\pi(\bar{f}_1 l - \bar{f}_2 n) + \varphi_{1,m} - \varphi_{2,m}\right)\right\}.
\end{aligned} \tag{45}$$

Recall that the aggregated phase $\varphi_{k,m} = 2\pi f_k(d_{k,m}/c + t_k) - \theta_k$ contains the unknown initial phase offset θ_k. We treat this unknown θ_k as random that makes $\varphi_{k,m}$ uniformly distributed over $(-\pi/2, \pi/2)$. Taking the expectation of $\mathbf{\Gamma}_m$ over $\varphi_{k,m} \sim \mathcal{U}(-\pi/2, \pi/2)$, we arrive at

$$\begin{aligned}
\left[\overline{\mathbf{\Gamma}}\right]_{n,l} =& \left[E_{\varphi_{1,m},\varphi_{2,m}}\left\{\mathbf{\Gamma}_m\right\}\right]_{n,l} \\
=& \frac{1}{(2\pi)^2}\int_{-\pi/2}^{\pi/2}\int_{-\pi/2}^{\pi/2} \varphi_{1,m}\varphi_{2,m}\left[\mathbf{\Gamma}_m\right]_{n,l} d\varphi_{1,m} d\varphi_{2,m} \\
=& \frac{1}{(2\pi)^2}\int_{-\pi/2}^{\pi/2}\int_{-\pi/2}^{\pi/2} \varphi_{1,m}\varphi_{2,m}\left\{\frac{a_1^2}{2}\cos\left(2\pi \bar{f}_1 (n-l)\right) + \frac{a_2^2}{2}\cos\left(2\pi \bar{f}_2 (n-l)\right)\right\} d\varphi_{1,m} d\varphi_{2,m} \\
=& \frac{a_1^2}{2}\cos\left(2\pi \bar{f}_1 (n-l)\right) + \frac{a_2^2}{2}\cos\left(2\pi \bar{f}_2 (n-l)\right),
\end{aligned} \tag{46}$$

which only depends on the lag $|n-l|$. Thus, by expressing the first term in (38) as

$$4\mathbf{D}_m\mathbf{K}_m\mathbf{D}_m = 4\overline{\mathbf{\Gamma}} \odot \mathbf{K}_m, \tag{47}$$

we can approximate $\widetilde{\mathbf{v}}_m$ as a circularly symmetric Gaussian random process. From (29), $\mathbf{K}_m^{white} = \sigma_m^2 \mathbf{I}_N$, so (47) simplifies to

$$4\overline{\mathbf{\Gamma}} \odot \mathbf{K}_m^{white} = 2\sigma_m^2(a_1^2 + a_2^2)\mathbf{I}_N, \tag{48}$$

when the noise is white. Substituting (39)-(41), (43) and (48) into (38), we obtain the covariance matrix $\widetilde{\mathbf{K}}_m$ of the aggregated white noise as

$$\begin{aligned} \widetilde{\mathbf{K}}_m^{white} =& 2\sigma_m^2(a_1^2 + a_2^2)\mathbf{I}_N + 2\sigma_m^4 \mathbf{I}_N \\ =& \widetilde{\sigma}_m^2 \mathbf{I}_N. \end{aligned} \tag{49}$$

In other words, when $\mathbf{v}_m$ is white and $\widetilde{\mathbf{v}}_m$ is approximated as circularly symmetric Gaussian, $\widetilde{\mathbf{v}}_m$ is also modeled as white noise with variance $\widetilde{\sigma}_m^2 = 2\sigma_m^2(a_1^2 + a_2^2\sigma_m^2)$.

2) Covariance matrix of the aggregated colored noise Similarly to the derivation we performed with the white noise, we use the expression (47) to approximate the aggregated colored noise. Hence, the first term in (38) with the colored noise modeled as an AR1 process is expressed as $\overline{\mathbf{\Gamma}} \odot \mathbf{K}_m^{AR1}$, where $\mathbf{K}_m^{AR1}$ is given in (30). The second term in (38) is rewritten as

$$\begin{aligned} \left[\mathbf{D}_m E\left[\mathbf{v}_m \mathbf{w}_m^T\right]\right]_{n,l} =& s_m[n] E\left[v_m[n] v_m^2[l]\right] \\ =& s_m[n] E\left[\left(\sum_{i_1=1}^{n} \rho^{n-i_1} u_{i_1}\right)\left(\sum_{i_2=1}^{l} \rho^{l-i_2} u_{i_2}\right)\left(\sum_{i_3=1}^{l} \rho^{l-i_3} u_{i_3}\right)\right], \end{aligned} \tag{50}$$

where $v_m[n] \approx \sum_{i=1}^{n} \rho^{n-i} u_i$ from (136). When we expand this product of summations, we obtain a sum of products of u_{i_1}, u_{i_2}, and u_{i_3}. Since u_{i_1}, u_{i_2}, and u_{i_3} are independent zero-mean Gaussian random variables, all the three possible cases become zero:

- Case 1: $i_1 = i_2 = i_3 \rightarrow E\left[u_{i_1} u_{i_2} u_{i_3}\right] = 0$,
- Case 2: $i_1 = i_2 \neq i_3 \rightarrow E\left[u_{i_1} u_{i_2}\right] E\left[u_{i_3}\right] = 0$,
- Case 3: $i_1 \neq i_2 = i_3 \rightarrow E\left[u_{i_1}\right] E\left[u_{i_2} u_{i_3}\right] = 0$.

As a result, (50) is zero. Likewise, it can be shown that the third term in (38) is also a zero matrix. The fourth term is an autocorrelation matrix of the squared AR1 process $\mathbf{v}_m \odot \mathbf{v}_m$. Using the ACF of the squared AR1 process derived in Appendix A, the fourth term in (38) is expressed as

$$\left[E\left[\mathbf{w}_m \mathbf{w}_m^T\right]\right]_{n,l} = \kappa_m^4 \left\{ \frac{1 + 2\rho^{|n-l|}}{(1-\rho^2)^2} \right\}. \tag{51}$$

Finally, from $E\left[\widetilde{\mathbf{v}}_m\right] = \kappa_m^2/(1-\rho^2)$, the last term in (38) becomes $\kappa_m^4/(1-\rho^2)^2 \mathbf{1}_N \mathbf{1}_N^T$. Consequently, the covariance matrix $\widetilde{\mathbf{K}}_m$ of the aggregated colored noise is given by

$$\left[\widetilde{\mathbf{K}}_m^{AR1}\right]_{n,l} = 4\left[\bar{\mathbf{\Gamma}} \odot \mathbf{K}_m^{AR1}\right]_{n,l} + \frac{2\kappa_m^4 \rho^{|n-l|}}{(1-\rho^2)^2}. \tag{52}$$

Closed-form expressions for the CRLBs When the noise is white, the CRLBs of the Q-range estimates for the RIPS-u in (32) and for the RIPS-sq in (35) can be simplified with few assumptions [54]. As long as $mod(f_k - f_0, f_s) \neq 0, \frac{1}{2}$, we find following approximations:

$$\begin{aligned} \mathbf{p}_N^T(\bar{f}_k)\mathbf{p}_N(\bar{f}_k) &= \sum_{n=0}^{N-1} \sin^2(2\pi \bar{f}_k n) = \frac{N}{2} + \sum_{n=0}^{N-1} \sin(4\pi \bar{f}_k n) \approx \frac{N}{2}, \\ \mathbf{p}_N^T(\bar{f}_d)\mathbf{p}_N(\bar{f}_d) &= \sum_{n=0}^{N-1} \sin^2(2\pi \bar{f}_d n) = \frac{N}{2} + \sum_{n=0}^{N-1} \sin(4\pi \bar{f}_d n) \approx \frac{N}{2}. \end{aligned} \tag{53}$$

Likewise, with $mod(f_d, f_s) \neq 0, \frac{1}{2}$ and $mod(g - f_0, f_s) \neq 0, \frac{1}{4}$, we find

$$\mathbf{p}_N^T(\bar{f}_1)\mathbf{p}_N(\bar{f}_2) \sum_{n=0}^{N-1} \sin(2\pi \bar{f}_1 n) \sin(2\pi \bar{f}_2 n) \approx 0. \tag{54}$$

Using (53), we can simplify the FIM of the phase estimates for the RIPS-u in (27) as

$$\mathbf{A}\mathbf{P}^T \mathbf{K}_m^{-1} \mathbf{P}\mathbf{A} = \frac{N}{2\sigma_m^2} \begin{bmatrix} a_1^2 & 0 \\ 0 & a_2^2 \end{bmatrix}. \tag{55}$$

Trace of the inverse of (55) yields the CRLB of the Q-range estimates in the RIPS-u as

$$CRLB(q^{(u)}) = \left(\frac{c}{2\pi}\right)^2 \frac{2}{N} \left(\frac{1}{a_1^2 f_1^2} + \frac{1}{a_2^2 f_2^2}\right)(\sigma_1^2 + \sigma_2^2). \tag{56}$$

In the RIPS-sq, the covariance matrix of the aggregated noise can be expressed as $\widetilde{\mathbf{K}}_m^{white} = \widetilde{\sigma}_m^2$, where $\widetilde{\sigma}_m^2 = 2\sigma_m^2(a_1^2 + a_2^2 + \sigma_m^2)$. Then, with the approximation in (54), the CRLB of ϕ_m in (33) is simplified as

$$CRLB(\phi_m) = \frac{2\widetilde{\sigma}_m^2}{a_1^2 a_2^2 N}. \tag{57}$$

Hence, the closed-form CRLB of the Q-range estimates in the RIPS-sq under white noise is expressed as

$$CRLB(q^{(sq)}) = \left(\frac{c}{2\pi}\right)^2 \frac{2}{N} \left(\frac{1}{a_1^2 a_2^2 g^2}\right) (\widetilde{\sigma}_1^2 + \widetilde{\sigma}_2^2). \tag{58}$$

3.2.2 Cramér-Rao Lower Bounds of Location Estimates

Using the CRLBs for the Q-ranges derived thus far, the CRLB of the location estimates in the RIPS-u and the RIPS-sq are derived. Following the localization procedure described in Section 3.1.2, the first transmitter is fixed as the target node. Considering a 2D scenario, we denote the coordinates of the target node and the mth receiver node as $\mathbf{x} = [x,\ y]^T$ and $\mathbf{x}_m = [x_m,\ y_m]^T$, respectively. Although we only consider a 2D scenario here, the same derivation is applied for a 3D scenario. The Q-range $q = d_{1,1} - d_{2,1} - d_{1,2} + d_{2,2}$ can be represented as a function of x and y as

$$q = \sqrt{(x - x_1)^2 + (y - y_1)^2} - \sqrt{(x - x_2)^2 + (y - y_2)^2} - d_{2,1} + d_{2,2}. \tag{59}$$

Taking a partial derivative of q with respect to x and y, we arrive at

$$\begin{aligned} \frac{\partial q}{\partial x} &= \frac{x - x_1}{d_{1,1}} - \frac{x - x_2}{d_{1,2}}, \\ \frac{\partial q}{\partial y} &= \frac{y - y_1}{d_{1,1}} - \frac{y - y_2}{d_{1,2}}. \end{aligned} \tag{60}$$

Suppose there are M anchor nodes, and the first receiver is fixed for all ranging sessions. Then, $M - 1$ independent measurements can be achieved, and assume that these estimates are obtained independently using an efficient estimator. In such a case, denoting the Q-range measurement at the lth ranging session as q_l for $l = 1, ..., M-1$,

the FIM of $\mathbf{x}$ is given as [16]

$$\mathbf{F}(\mathbf{x}) = \begin{bmatrix} \frac{\partial q_1}{\partial x} & \frac{\partial q_1}{\partial y} \\ \vdots & \vdots \\ \frac{\partial q_{M-1}}{\partial x} & \frac{\partial q_{M-1}}{\partial y} \end{bmatrix}^T \begin{bmatrix} CRLB(q_1) & & \\ & \ddots & \\ & & CRLB(q_{M-1}) \end{bmatrix} \begin{bmatrix} \frac{\partial q_1}{\partial x} & \frac{\partial q_1}{\partial y} \\ \vdots & \vdots \\ \frac{\partial q_{M-1}}{\partial x} & \frac{\partial q_{M-1}}{\partial y} \end{bmatrix}. \tag{61}$$

Performing the matrix multiplications, (61) becomes

$$\mathbf{F}(\mathbf{x}) = \sum_{l=1}^{M-1} CRLB(q_l)^{-1} \begin{bmatrix} \left(\frac{\partial q_l}{\partial x}\right)^2 & \left(\frac{\partial q_l}{\partial x}\right)\left(\frac{\partial q_l}{\partial y}\right) \\ \left(\frac{\partial q_l}{\partial x}\right)\left(\frac{\partial q_l}{\partial y}\right) & \left(\frac{\partial q_l}{\partial y}\right)^2 \end{bmatrix}. \tag{62}$$

Finally, the CRLB of x and y are achieved along the diagonal of the inverse of $\mathbf{F}(\mathbf{x})$ as

$$CRLB(x) = \left[\mathbf{F}^{-1}(\mathbf{x})\right]_{1,1}, \tag{63}$$

and

$$CRLB(y) = \left[\mathbf{F}^{-1}(\mathbf{x})\right]_{2,2}. \tag{64}$$

3.2.3 Numerical Results

In this section, we evaluate the CRLBs and compare the performance of the RIPS-u and the RIPS-sq through numerical examples. We choose $g = 8$ MHz and $f_d = 1.2$ kHz, and thus $f_1 = g + f_d/2$ and $f_2 = g - f_d/2$. In both systems, the received signal is sampled at the rate $f_s = 4.8$ kHz. The LO frequency is $f_0 = 6$ MHz, and the signal length is $T_s = 0.025$ sec, which allows us to collect $N = 121$ samples per Q-range estimate. For simplicity, we let $a_1 = a_2 = 1$, $\sigma_m^2 = \sigma^2$ and $\kappa_m^2 = \kappa^2$ for $m = 1, 2$. When we consider the colored noise, we let $\rho = 0.99$. Throughout this dissertation, we define the SNR as

$$SNR = \frac{P_T}{P_N} \tag{65}$$

where P_T and P_N are the total transmission and noise power at transmitted tones. In the RIPS-u and the RIPS-u, the total transmission power is

$$P_T = \frac{a_1^2}{2} + \frac{a_2^2}{2}, \tag{66}$$

and the noise power is

$$P_N = 2P_v\left(\bar{f}_1\right) + 2P_v\left(\bar{f}_2\right), \tag{67}$$

where $P_v(f)$ is the power-spectral density (PSD) of the additive noise $v_m[n]$. When the noise is white, the PSD of $v_m[n]$ is given as

$$P_v(f) = \sigma^2, \tag{68}$$

and the PSD of the AR1 process is

$$P_v(f) = \frac{\kappa^2}{1 - 2\rho\cos(2\pi f) + \rho^2}. \tag{69}$$

CRLB of the Q-range estimates Figures 4 and 5 show a square-root of the CRLB of the Q-range estimates vs. SNR under white and colored noise, respectively. For the white noise case, we also plotted the closed-form CRLBs. The closed-form CRLBs match well with the exact CRLBs, and we confirm that the closed-form CRLBs in (56) and (58) provide good approximations for those in (32) and (35) for the RIPS-u and the RIPS-sq, respectively. In both figures, the RIPS-u outperforms the RIPS-sq regardless of the noise statistics as expected from [54]. Furthermore, a gap between the curves widens as the SNR decreases. This is due to σ_m^4 term in (49) and (52) dominating when the SNR is low (i.e. the noise variance is high). Moreover, the performance gap between two systems is wider when the noise is colored. Notice that the performance of the RIPS-u is unchanged under both the white and colored noise case, while the RIPS-sq experiences the performance degradation when the noise becomes colored. Therefore, the RIPS-u is more robust to the noise correlation than the RIPS-sq.

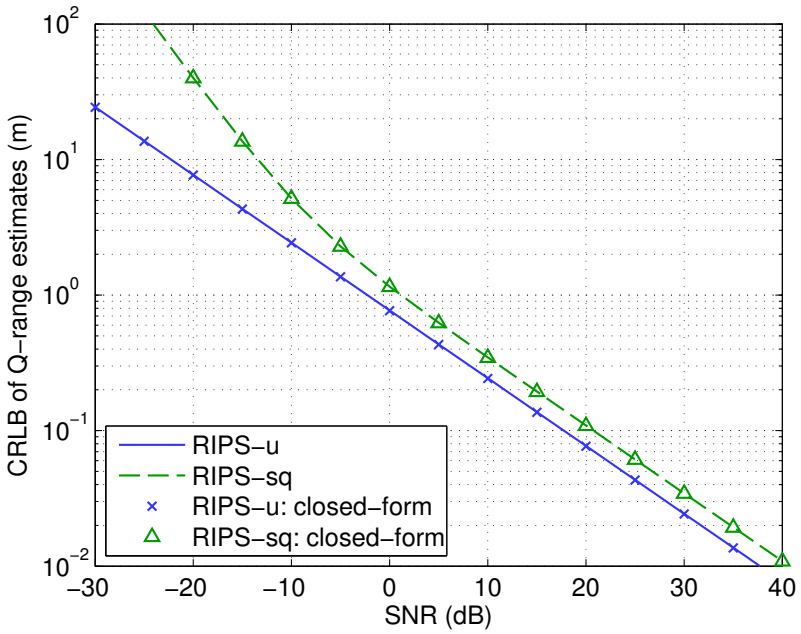

Figure 4: CRLB of the Q-range estimates under white noise vs. SNR.

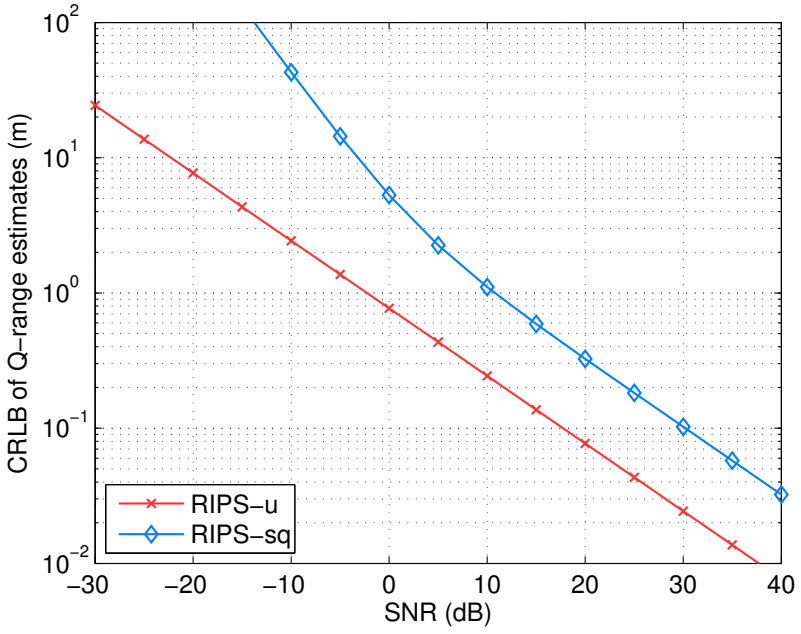

Figure 5: CRLB of the Q-range estimates under colored noise vs. SNR.

In Figures 6 and 7, we plot the CRLB vs. the carrier frequency g under white and colored noise, respectively. The SNR is fixed at 10 dB. The general trend here is the performance improves as g increases. However, this is at the cost of diminishing resolvable range as described in Section 3.1.3, and when g increases, it is likely that the Q-range estimates to have a unknown integer. Moreover, notice that Figure 7(d), the CRLB for the RIPS-sq is not smooth. This is because $\widetilde{\mathbf{K}}_m^{AR1}$ in (52) depends on g. As ρ increases, the noise correlation becomes stronger, making the irregularities in the curve corresponding to the CRLB of the RIPS-sq severe. Nevertheless, the CRLB of the RIPS-u is always under that for the RIPS-sq, which confirms the efficiency of the RIPS-u.

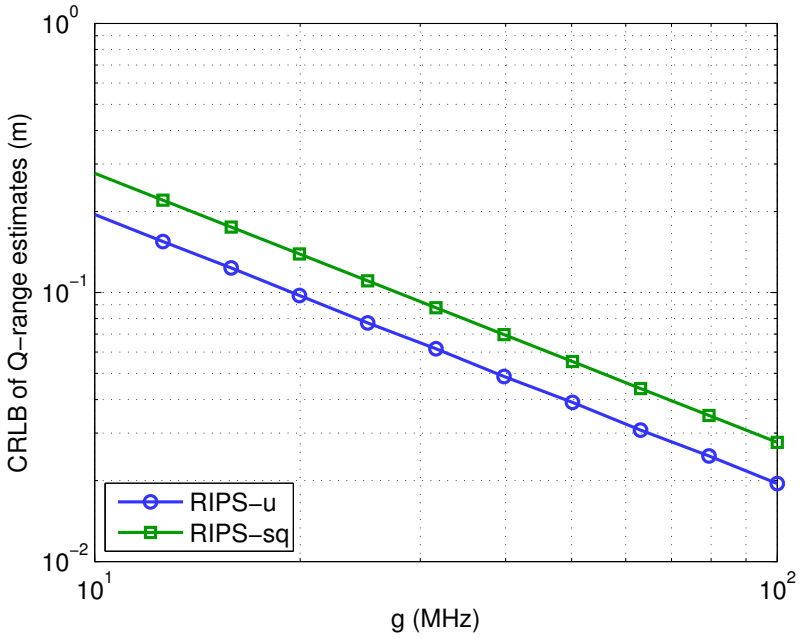

Figure 6: CRLB of the Q-range estimates under white noise vs. the carrier frequency g.

In Figures 8 and 9, we varied the frequency difference f_d and plotted the CRLBs under white and colored noise, respectively. In Figure 8, CRLB curves are flat and show that f_d does not affect the CRLB as much as g since $f_d \ll g$. Yet, a small f_d is desirable for the RIPS-sq due to the dependence of the approximated term in

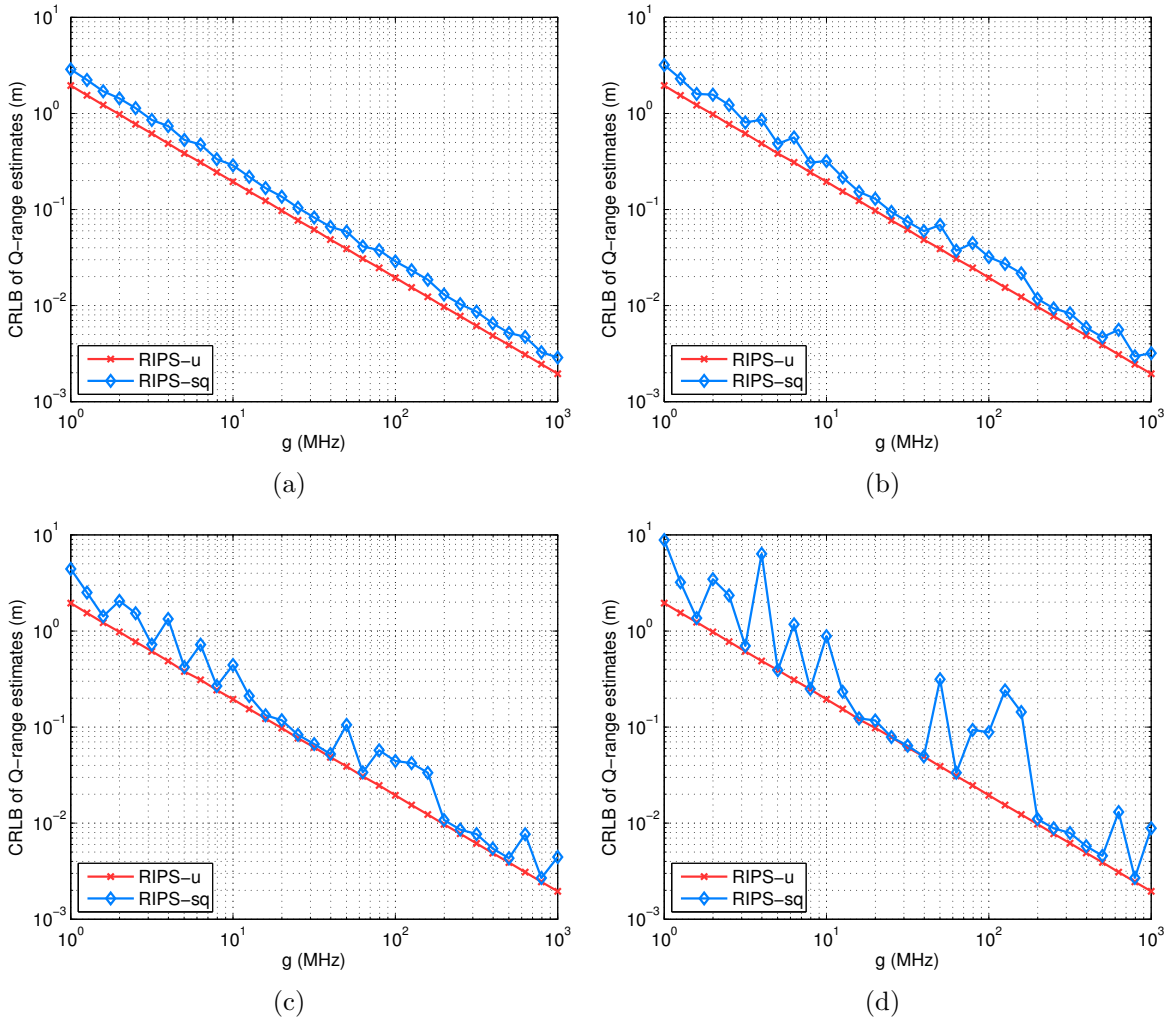

Figure 7: CRLB of the Q-range estimates under colored noise vs. the carrier frequency g with (a) $\rho = 0.1$, (b) $\rho = 0.3$, (c) $\rho = 0.6$, and (d) $\rho = 0.99$.

(7). When f_d is large with respect to g, the approximated term becomes a dominant source of error in the RIPS-sq. Similarly to Figure 7(d), the CRLB corresponding to the RIPS-sq shows irregularities, and the irregularities increase with ρ. Yet, the CRLB of the RIPS-u is better than that of the RIPS-sq in general.

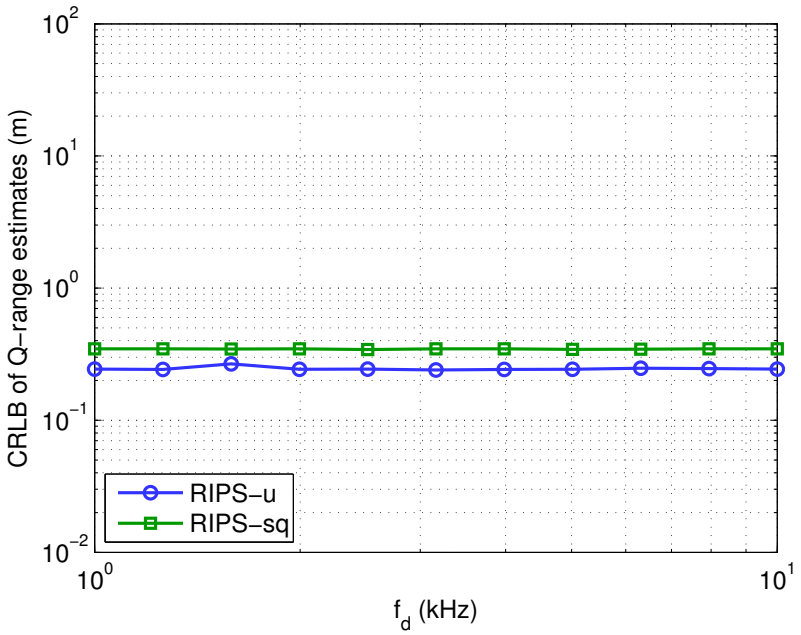

Figure 8: CRLB of the Q-range estimates under white noise vs. the frequency difference f_d.

CRLB of the location estimates To analyze the localization performance of the RIPS, we set the anchor nodes at the corners and the center of 10×10 square. We use the same frequencies from previous simulations. The localization is performed as described in Section 3.1.2, where the Q-range is converted to the RD measurements. The target node and the anchor node at the center are fixed as the first and second transmitters, respectively. The rest of the four anchor nodes take turns to obtain four independent Q-range measurements.

A square-root of the trace of $\mathbf{F}^{-1}(\mathbf{x})$, $\sqrt{CRLB(x) + CRLB(y)}$, for the RIPS-u and the RIPS-sq at various target node locations are shown as a color map in Figures 10(a) and 10(b), respectively. The SNR is fixed at 10 dB. White circles denote the

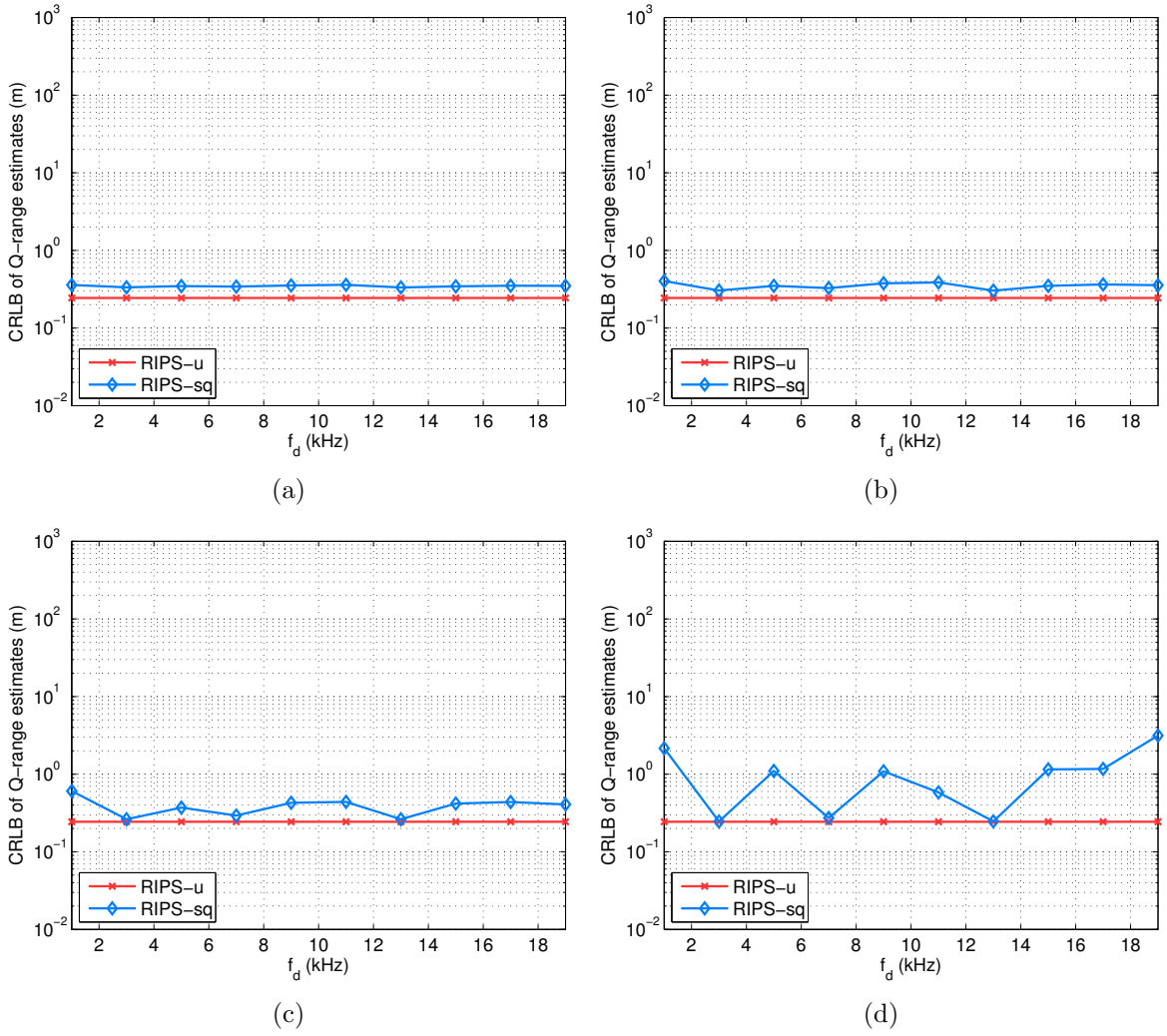

Figure 9: CRLB of the Q-range estimates under colored noise vs. the frequency difference f_d with (a) $\rho = 0.1$, (b) $\rho = 0.3$, (c) $\rho = 0.6$, and (d) $\rho = 0.99$.

locations of the anchor nodes. In both figures, the CRLB increases as the target node moves away from the origin. For brevity, figures for colored noise are not plotted here, but similar trend is observed. Figure 11 plots the CRLB of the location estimates vs. SNR at six different target node locations specified with $\triangle$ marks in Figure 10. Solid lines represent the CRLBs corresponding to the RIPS-u and dashed lines correspond to that of the RIPS-sq. At any given location, the RIPS-u has the CRLB 3 dB lower than that of the RIPS-sq. Comparing the curves corresponding to positions inside ($L1 \sim L3$) and outside ($L4 \sim L6$) the square, we observe that the latter has higher bounds compared to the former as we have already observed in Figure 10.

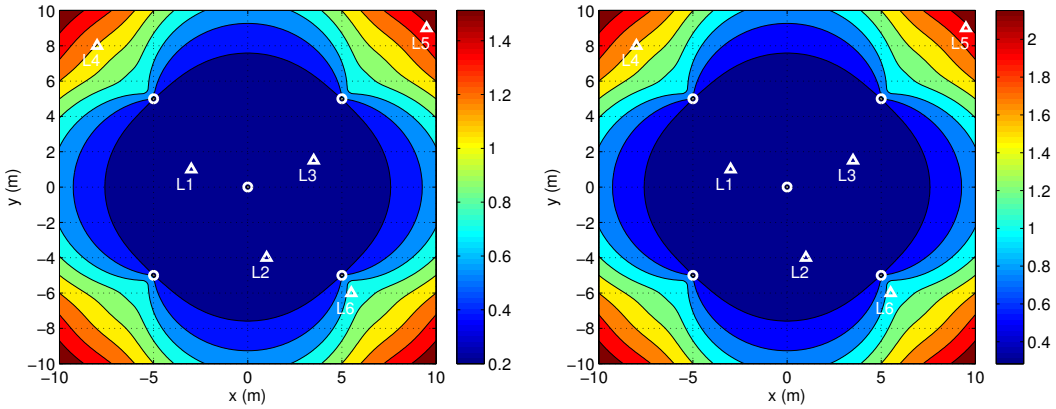

Figure 10: CRLB of the location estimates of (a) the RIPS-u and (b) the RIPS-sq under the white noise with symmetric anchor arrangements.

Color maps in Figure 10 are symmetric since the anchor node are placed symmetrically. In Figures 12(a) and 12(b), we moved one of the anchor nodes closer to the center. As a result, the CRLB color map becomes asymmetric in both the figures. Hence, anchor node locations have impact on the localization performance. Impact of anchor node arrangements is not investigated deeply in this dissertation. We leave this topic for future research.

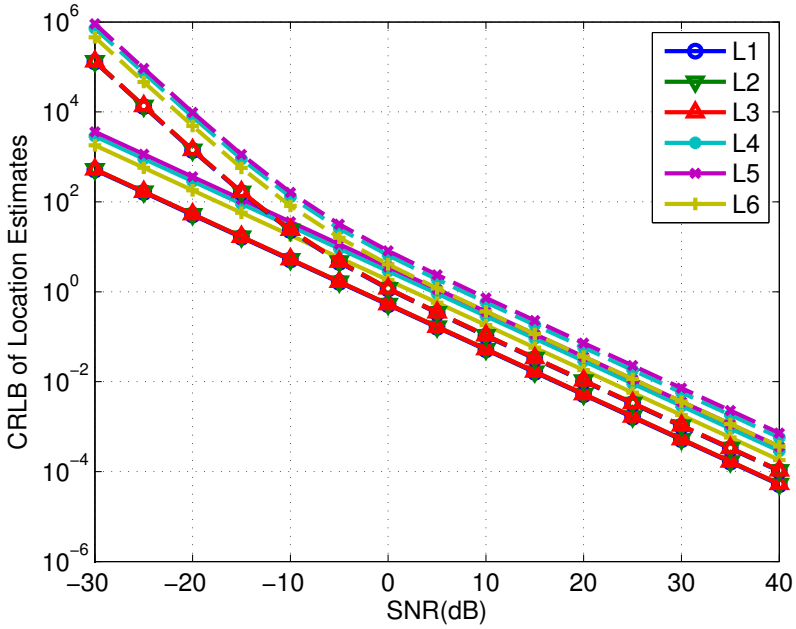

Figure 11: CRLB of the location estimates under white noise vs. SNR. Solid lines represent the CRLBs corresponding to the RIPS-u and dashed lines correspond to that of the RIPS-sq.

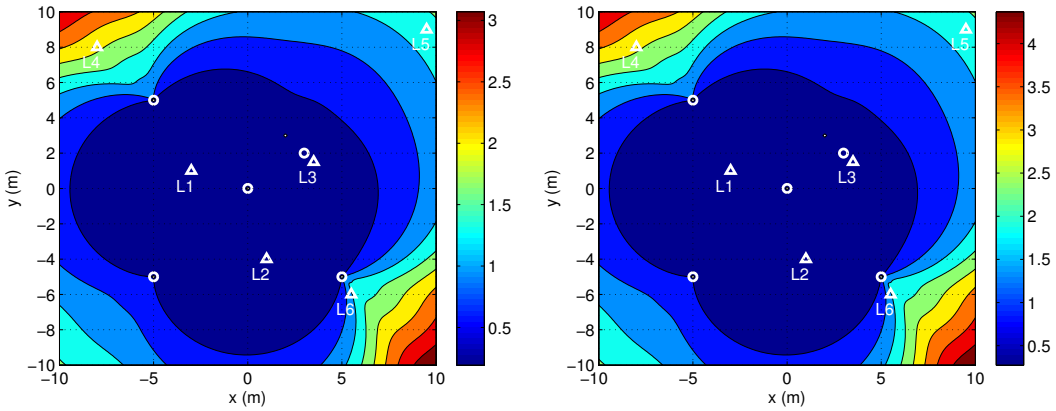

(a) (b)

Figure 12: CRLB of the location estimates of (a) the RIPS-u and (b) the RIPS-sq under the white noise with asymmetric anchor arrangements.

Monte-Carlo Simulations Using the same parameters, we performed the Monte-Carlo simulations to corroborate the derived CRLBs and confirm the efficiency of the proposed RIPS-u. We randomly deploy four nodes in 10×10 meters square, and the Q-range is estimated with the RIPS-u and the RIPS-sq. The root-mean-square error (RMSE) of the Q-range estimates vs. SNR under white and colored noise are plotted in Figures 13 and 14, respectively. The resolvable range for the RIPS-sq ($c/2g = 18.75$ m) is plotted here. For comparison, we simulated the cases where $f_d = 120$, 1.2 kHz, and 120 kHz. The CRLB plotted in the figures is when $f_d = 1.2$ kHz. The CRLBs of the Q-range estimates with the RIPS-u match closely with corresponding RMSE curves when the SNR > -10 dB when the noise is white and SNR > 0 dB when the noise is colored. With the RIPS-sq, we observe the error floor at the high-SNR region in the corresponding RMSE curves. This is due to the approximation in the Q-range estimation with the RIPS-sq and non-ideal LPF used to extract a low-frequency differential signal. Although the error from LPF is more prominent here, the error due to approximation error is well-presented in [54], where the RIPS is presented with a complex-passband signal model. In the low-SNR region, the RMSE curves of both systems reach an upper bound. Since the Q-range is estimated by unwrapping the phase, the magnitude of the Q-range estimates is always less than c/f_k in the RIPS-u and c/g in the RIPS-sq. In this simulation setup, the true Q-range is also bounded, which makes the RMSEs to have upper-bounds. As we have seen in Figure 8, f_d does not impact the performance when the noise is white. When the noise is colored, the performance of the RIPS-sq changes with different values of f_d, which agrees with the results shown in Figure 9.

To analyze the localization performance, we used the same parameters and anchor setup as Figure 10. As the CRLBs of location estimates depend on the target node location, we take an average of the CRLBs over the area. The frequency difference is set to $f_d = 1.2$ kHz. Figures 15 and 16 show the RMSE of the location estimates

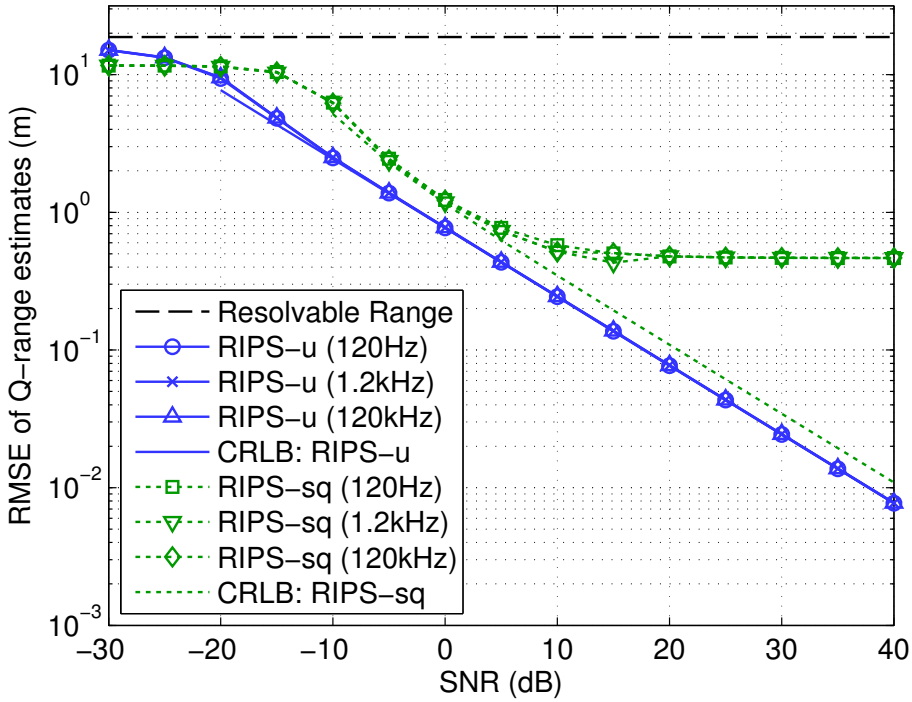

Figure 13: RMSE of the Q-range estimates under white noise.

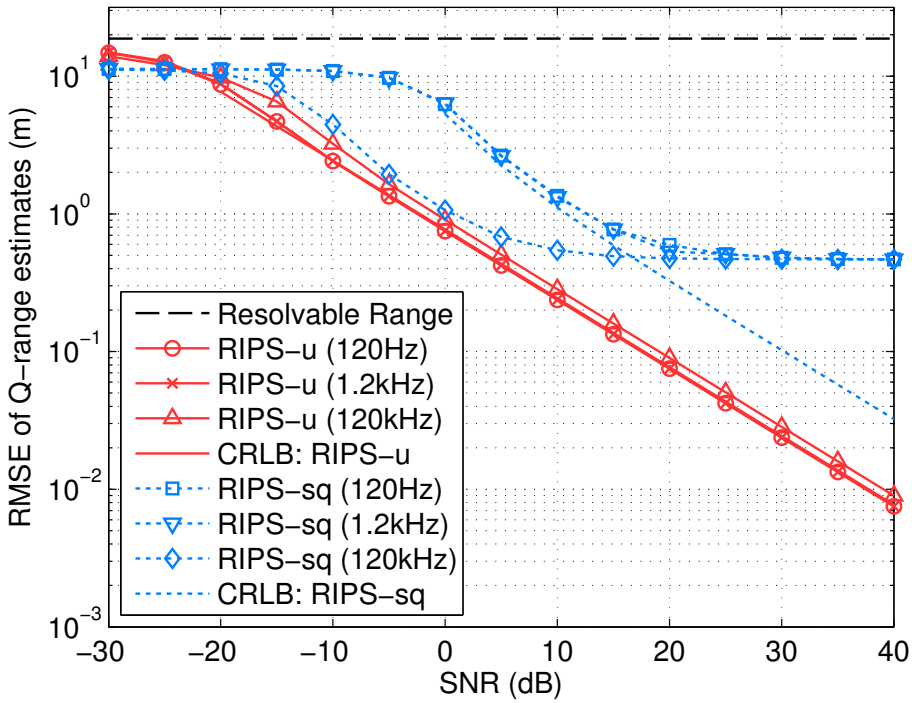

Figure 14: RMSE of the Q-range estimates under colored noise.

under white and colored noise, respectively. In the RIPS-u, a submeter accuracy (RMSE < 1 m) is achieved when SNR > 0 dB regardless of the noise color. With the RIPS-sq, SNR > 3 dB under white noise and SNR > 12 dB under colored noise are required to yield the RMSE less than one meter.

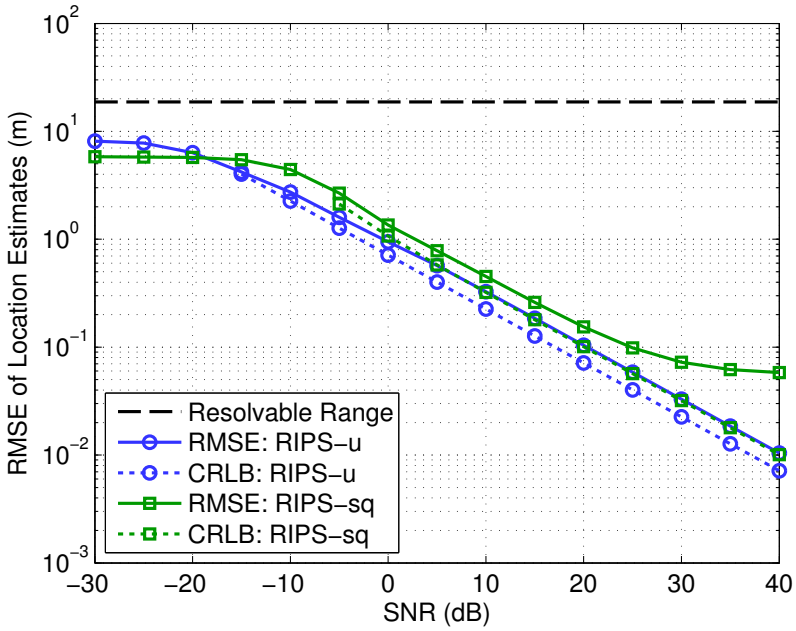

Figure 15: RMSE of location estimates with the RIPS under white noise.

3.2.4 Exploiting the Noise Correlation Information

When the noise correlation is known, we can exploit the information and improve the ranging performance in the RIPS-u and the RIPS - sq. Here, we consider the cases when the noise correlation information is available at the transmitter and the receiver separately.

Noise correlation information available at the transmitters Let us first observe how transmission power affect the ranging performance of the systems. For analysis, we constrain $a_1^2 + a_2^2 = 1$. Keeping the rest of the parameters as the same as the preceding simulations, we plot the CRLBs vs. a_1^2 under white Gaussian noise in Figure 17. In both the RIPS-u and the RIPS-sq, the CRLB is at minimum when

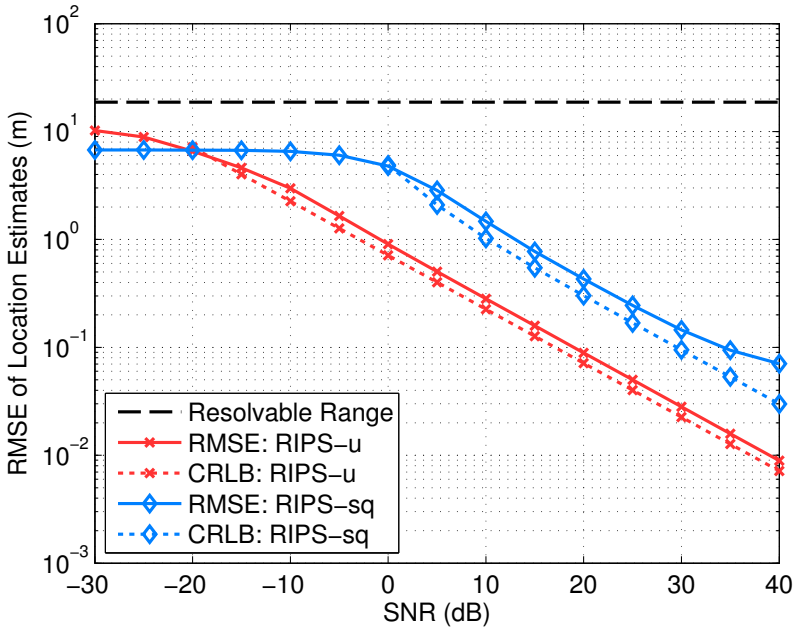

Figure 16: RMSE of location estimates with the RIPS under colored noise.

$a_1^2 = a_2^2$. Hence, it is optimal to distribute the power equally at two transmitter when the noise is white. Refer to Appendix B for mathematical proof. In the rest this chapter, we define the optimal power distribution as that attains the minimum CRLB.

In Figure 18, the CRLBs vs. a_1^2 under colored noise is plotted. Unlike the case when the noise is white, the equal transmission power does not yield the minimum CRLBs when the noise is colored. This can be explained by looking at the PSD of the noise. In the RIPS-u, the noise of the sampled signal $r_m[n]$ in (9) is the colored noise modeled as AR1, and the PSD given in (69) is plotted against the normalized frequency in Figure 19. The dashed and dotted vertical lines are where the tones corresponding to $\bar{f}_1$ and $\bar{f}_2$ are located, respectively. According to the PSD, the noise has more energy toward lower frequencies. As a result, more power should be allocated in the RIPS-u to the first transmitter to improve the accuracy of the phase $\varphi_{1,m}$ estimated from the corresponding tone at $\bar{f}_1$.

In the RIPS-sq, the noise of the sampled signal $y_m[n]$ in (16) is the aggregated

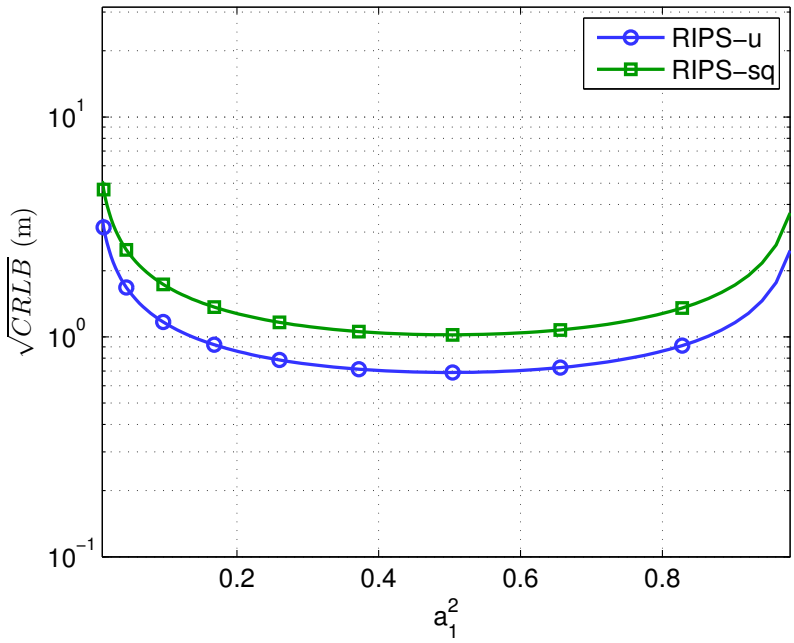

Figure 17: CRLB the Q-range estimates vs. a_1^2 under white noise ($a_1^2 + a_2^2 = 1$).

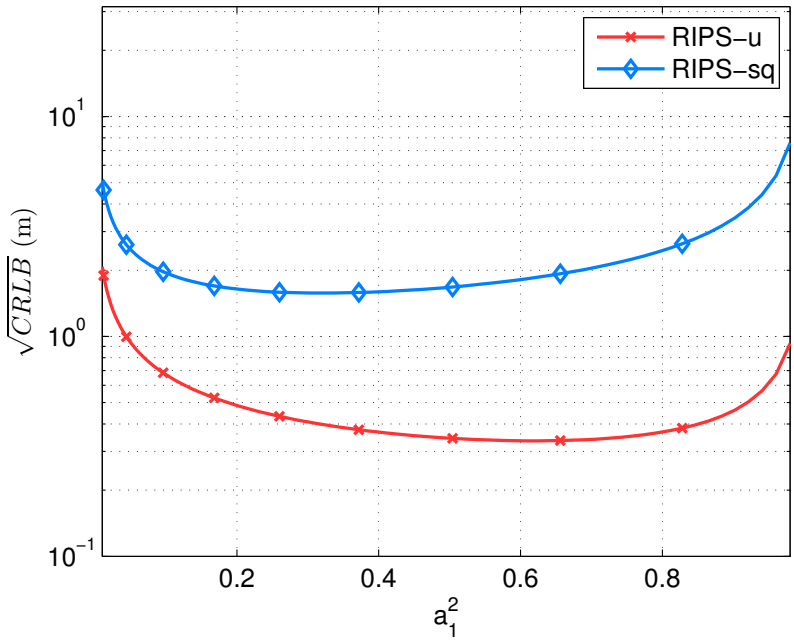

Figure 18: CRLB of the Q-range estimates vs. a_1^2 under colored noise ($a_1^2 + a_2^2 = 1$).

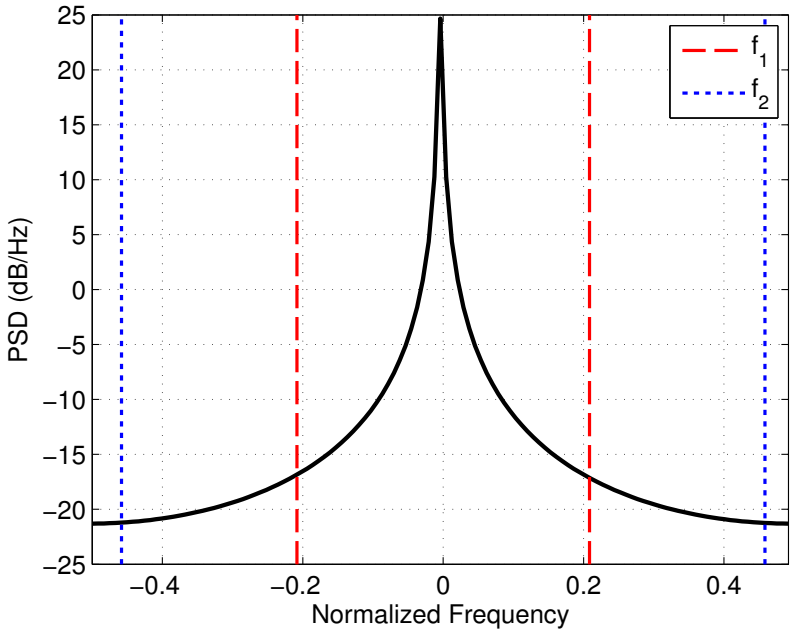

Figure 19: PSD of the colored noise in the RIPS-u.

noise given in (36). From (52), the ACF of the aggregated colored noise can be rewritten as

$$R_{\tilde{v}_m}(\tau) = \left(2a_1^2\cos(2\pi\bar{f}_1\tau) + 2a_2^2\cos(2\pi\bar{f}_2\tau) + \frac{2\kappa_m^2}{1-\rho^2}\right)\frac{\kappa_m^2\rho^{|\tau|}}{1-\rho^2}. \tag{70}$$

Notice that (70) is the product of the ACF of the AR1 noise and the sum of cosines and DC term. The Fourier transform of (70) is then a sum of the copies of the PSD given in (69) shifted to $f = 0$, $\pm\bar{f}_1$, and $\pm\bar{f}_2$ with gains $2\kappa_m^2/(1-\rho^2)$, a_1^2, and a_2^2, respectively. An example of the PSD of the aggregated noise is plotted in Figure 20. The solid vertical line in the figure is where the tone $\bar{f}_d$ is located, and the phase of this tone is what we estimate in the RIPS-sq. Notice that the tone is closer to the peak at $\pm\bar{f}_1$. To improve the accuracy of the estimated phase of the tone at $\bar{f}_d$, therefore, we want to reduce the energy around the peak at $\bar{f}_1$ by allocating a less power toward the first transmitter. As a result, the minimum CRLB in Figure 18 for the RIPS-sq is at $a_1^2 < 0.5$.

For the RIPS-u, the optimal power distribution under the colored noise is derived in Appendix B. For the RIPS-sq, however, finding the minimum CRLB w.r.t. a_1^2 is a

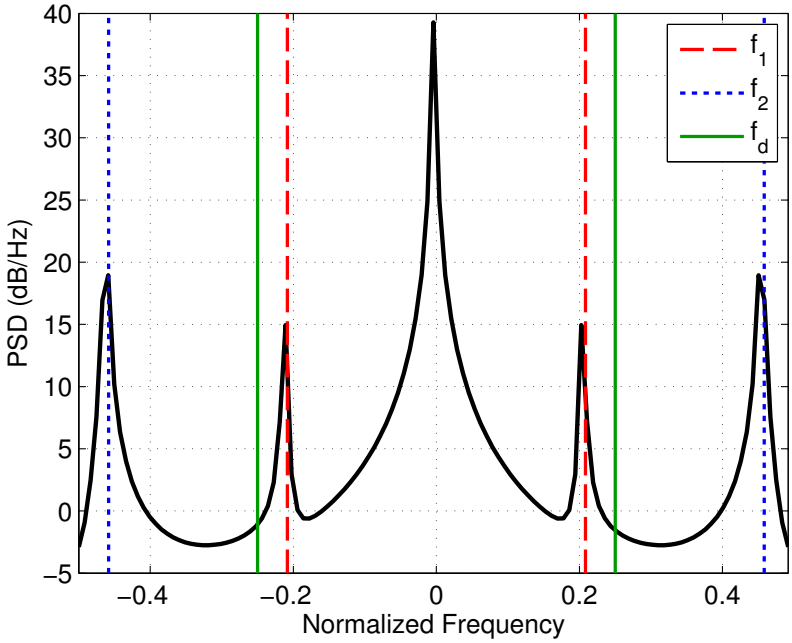

Figure 20: PSD of the aggregated colored noise in the RIPS-sq.

difficult task as the covariance matrix of the aggregated colored noise $\widetilde{\mathbf{K}}_m^{AR1}$ in (52) depends on a_1^2. From Figure 20, it is intuitive that we want to have a signal energy at $\bar{f}_d$ high while keeping the energy from the noise at $\bar{f}_d$ as low as possible. In other words, we want to maximize the local SNR at $\bar{f}_d$ defined as

$$SNR(\bar{f}_d) = \frac{a_1^2 a_2^2/2}{2P_{\widetilde{v}}(\bar{f}_d)}, \tag{71}$$

where the numerator is the energy of the tone at $\bar{f}_d$ and $P_{\widetilde{v}}(f)$ is the PSD of the aggregated noise $\widetilde{v}$. For simplicity, we assume that the noise statistics stay the same over two time slots, and hence we dropped the subscript m in (71). From (70), the PSD of the aggregated colored noise at $\bar{f}_d$ is expressed as

$$\begin{aligned} P_{\widetilde{v}}(\bar{f}_d) =& a_1^2 \left\{P_v(\bar{f}_d + \bar{f}_1) + P_v(\bar{f}_d - \bar{f}_1)\right\} + a_2^2 \left\{P_v(\bar{f}_d + \bar{f}_2) + P_v(\bar{f}_d - \bar{f}_2)\right\} + \frac{2\kappa^2}{1-\rho^2} P_v(0) \\ =& a_1^2 \widetilde{n}_1 + a_1^2 \widetilde{n}_2 + \widetilde{n}_0, \end{aligned} \tag{72}$$

where $P_v(f)$ is the PSD of the colored noise given in (69). Substituting (72) and the

total power constraint into (71), the local SNR at $\bar{f}_d$ is rewritten as

$$SNR(\bar{f}_d) = \frac{1}{4}\frac{a_1^2 a_2^2}{a_1^2\widetilde{n}_1 + (1-a_1^2)\widetilde{n}_2 + \widetilde{n}_0}. \tag{73}$$

Taking a derivative of (73) w.r.t. a_1^2 and equating to zero, we obtain

$$a_1^2 = \frac{\widetilde{n}_2 + \widetilde{n}_0 \pm \sqrt{(\widetilde{n}_2 + \widetilde{n}_0)(\widetilde{n}_1 + \widetilde{n}_0)}}{\widetilde{n}_2 - \widetilde{n}_1}. \tag{74}$$

The solutions are narrowed down by using the condition $0 < a_1^2 < 1$. Figure 21 compares (74) and the solution found by searching over $a_1^2 = [0.1, 0.99]$ with a step-size of 0.0001. From the figure, we conclude that (74) provides a reasonable approximation for the optimal power loading.

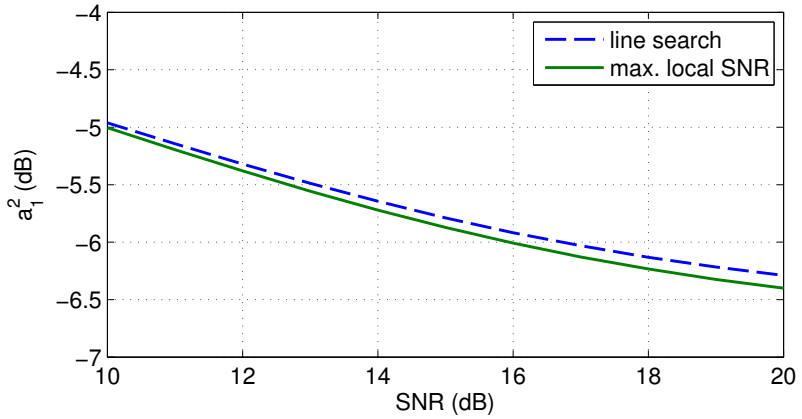

Figure 21: Optimal power allocated to the first transmitter vs. SNR.

Noise correlation information available at the receivers When the noise correlation information is available at the receiver, we can replace the LSE with the weighted-LSE (WLSE) in (12) and (19) for the RIPS-u and the RIPS-sq, respectively. The WLSE of the phase vector in the RIPS-u is given as

$$\widehat{\mathbf{z}}_m = \left(\mathbf{H}^T(\mathbf{f})\left(\mathbf{K}_m^{AR1}\right)^{-1}\mathbf{H}(\mathbf{f})\right)^{-1}\mathbf{H}^T(\mathbf{f})\left(\mathbf{K}_m^{AR1}\right)^{-1}\mathbf{r}_m, \tag{75}$$

and for the RIPS-sq is

$$\widehat{\widetilde{\mathbf{z}}}_m = \left(\mathbf{H}^T(\bar{f}_d)\left(\widetilde{\mathbf{K}}_m^{AR1}\right)^{-1}\mathbf{H}(\bar{f}_d)\right)^{-1}\mathbf{H}^T(\bar{f}_d)\left(\widetilde{\mathbf{K}}_m^{AR1}\right)^{-1}\mathbf{y}_m. \tag{76}$$

Then, the Q-range is calculated from the estimated phase vectors by using the estimators in (15) and (20) for the RIPS-u and the RIPS-sq, respectively.

We illustrate how the power loading and the WLSE affect the ranging performance of the RIPS-u and the RIPS-sq through simulations. In Figures 22 and 23, we plot the RMSE of the Q-range estimates vs. SNR for the RIPS-u and the RIPS-sq under the colored noise, employing either the power loading, the WLSE, or both. The optimal power distribution in the RIPS-u is found using (145) in Appendix B, and we employ the solution in (74) for the RIPS-sq. In both figures, when neither the transmitter nor the receiver has the knowledge of the noise covariance information, the corresponding curves are furthest from the CRLBs. This is equivalent to the case when the system assumes the noise is white. The ranging performance improves when either the power loading or the WLSE is employed. When both the transmitters and the receivers know the noise correlation information, the performance is the best. Moreover, the WLSE with power loading attains the CRLB in the RIPS-u.

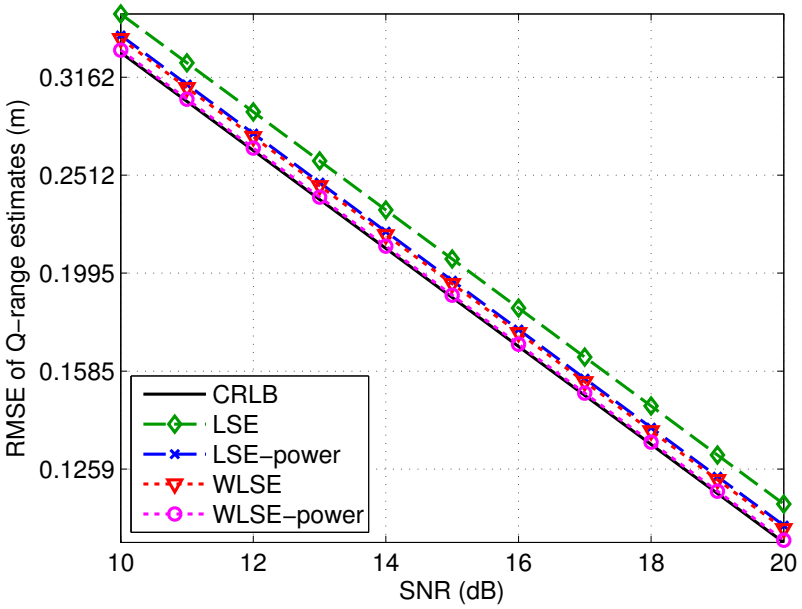

Figure 22: RMSE of the Q-range estimates using the RIPS-u vs. SNR with and without knowledge of noise correlations.

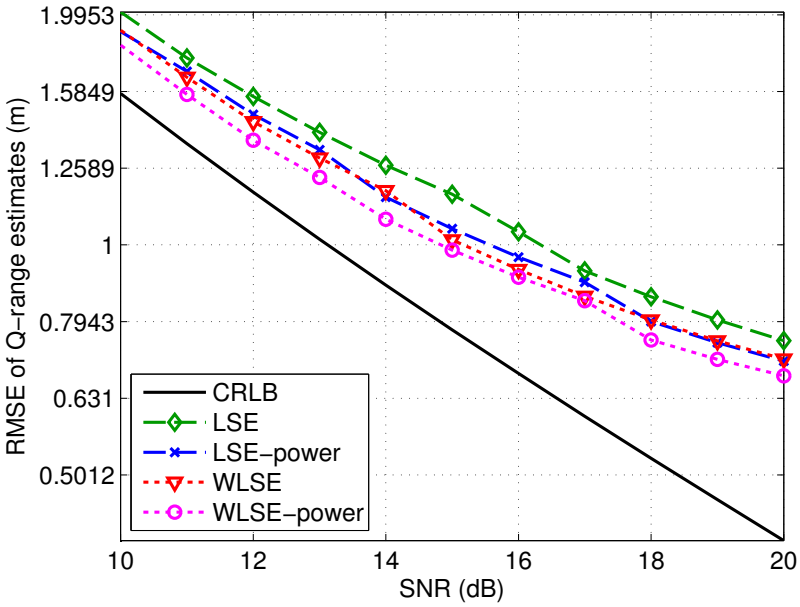

Figure 23: RMSE of the Q-range estimates using the RIPS-sq vs. SNR with and without knowledge of noise correlations.

3.3 Hardware Implementation

To further compare the performance of two systems, the RIPS-u and the RIPS-sq are implemented on the NI USRP [1] transceivers.

3.3.1 System Model

Figure 24 shows the hardware setup in the experiments. Four NI USRP 2920 are employed to estimate the Q-range using the RIPS-u and the RIPS-sq. Two USRPs are used as the transmitters, and two others are used as the receivers. Although one USRP transceiver is capable of both transmitting and receiving, separate devices are used to allow different spatial arrangements. The internal clock of the first receiver USRP is used as the reference clock, and a MIMO cable connects two receivers for synchronization. All the USRPs are connected to the host PC through Ethernet cables. The labVIEW is running in the host PC to control the USRPs and to perform Q-range estimations. Unfortunately, a squared-law device is not equipped in the

[1] NI stands for National Instruments, and USRP stands for universal software radio peripheral.

USRP, so the signal is squared after sampling in the RIPS-sq.

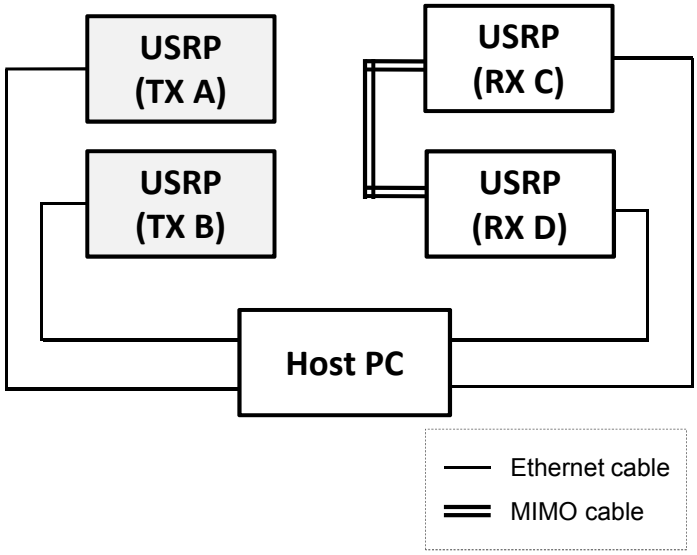

Figure 24: Experimental setup of the RIPS.

Let nodes A and B be denoted as transmitters and nodes C and D be receivers. Two USRPs transmit a pure sinusoid. At the receivers, the signal is downconverted by f_0, it is sampled at the rate $f_{s1} = 4$ MHz. Collected $N = 100,000$ samples are returned to the host PC. With the RIPS-sq, the signal is squared and decimated to f_s whereas for the RIPS-u, the signal is directly decimated to obtain the final sampled received signal.

3.3.2 Receiver Synchronization

Recall that the RIPS requires a perfect synchronization in time at two receivers, but the internal clock of the USRP used as the reference to synchronize two receivers can only provides a coarse synchronization. As a result, the phase difference between two receivers contains two unknowns: a distance metric and a time offset between the receivers. To compensate for the time offset, true distances are physically measured, and this true distances are used to calculate the time offset at the beginning of the ranging session. Assuming the offset between receivers is constant over a period of time, the estimated time offset is used to calibrate the signal prior to the Q-range

estimation.

3.3.3 Frequency Estimation

In the RIPS, the perfect synchronization of frequencies among all the nodes is assumed. However, as mentioned, only a coarse synchronization between receivers is achieved with a current setup, and local oscillators at two transmitters can further produce frequency offsets. The frequencies are estimated from the sampled received signal at the host PC using the frequency detector function in the labVIEW to measure the offset, and frequency offsets up to 20 Hz are observed. Since how CFOs affect the Q-range estimation performance is different between the RIPS-sq and the RIPS-u, the relative performance of the two systems varies with the CFOs.

3.3.4 Experimental Results

Frequencies used in the experiment are $f_2 = 80$ MHz, $f_d = 14$ kHz, $f_1 = f_2 + f_d$ and $f_0 = 79$ MHz. The received signal is first sampled at $f_{s1} = 4$ MHz and then downsampled to $f_s = 400$ kHz for both the RIPS-u and the RIPS-sq. The resolvable range in the RIPS-sq and the RIPS-u is $\frac{c}{2g} \approx \frac{c}{2f_k} \approx 1.875$ m. Since the length of the MIMO cable is less than one meter, the experimental setup cannot have the Q-range exceeding the bound. With chosen parameters, the approximation error in the RIPS-sq is less than 0.001 meters.

The USRPs are placed in three different arrangements, and these setups are listed in Table 1. A number below each setup is the true Q-range. In each setup, the USRP labeled "node D (RX2)" is connected to the one labeled "node C (RX1)" through the MIMO cable for a coarse synchronization. The receiver and frequency offsets are assumed to be constant over a period of time required to obtain 100 Q-range estimates, and the offsets are recalculated every 100 Q-range estimates. Repeating this process for 10 times, 1000 Q-range estimates are achieved.

The cumulative distribution function (CDF) of the Q-range estimation errors for

three setups is presented in Figure 25. As mentioned earlier, the RIPS is sensitive to the CFOs, and the CFOs randomly fluctuate over time. This instability caused the difference in the relative performance of the two systems among three cases, but the performance gain of the RIPS-u over the RIPS-sq is noticeable, especially in Case 2. Furthermore, the RIPS-u achieves smaller standard deviation compared to the RIPS-sq as shown in Table 2. Hence, the experimental results confirm that the RIPS-u has better performance than the RIPS-sq.

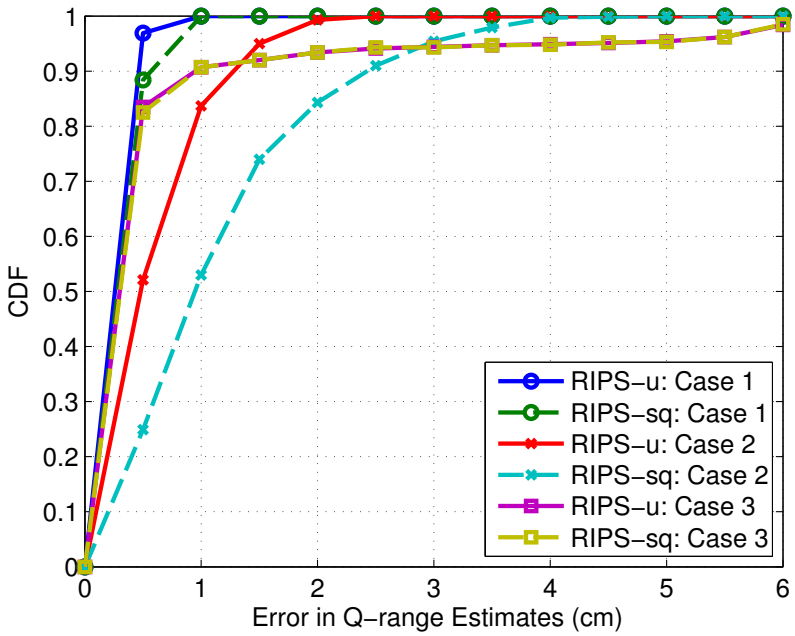

Figure 25: CDF of the Q-range estimates of the RIPS from the experiments.

Table 1: Three experimental setups of NI USRPs for the RIPS.

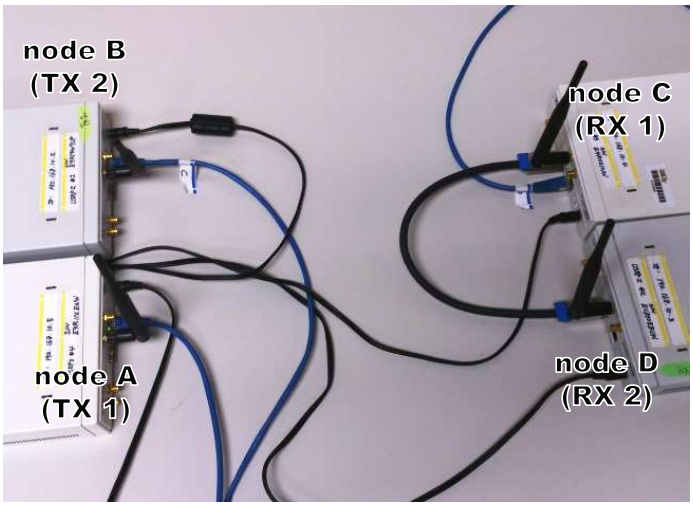

Case 1: $q = 4$ cm

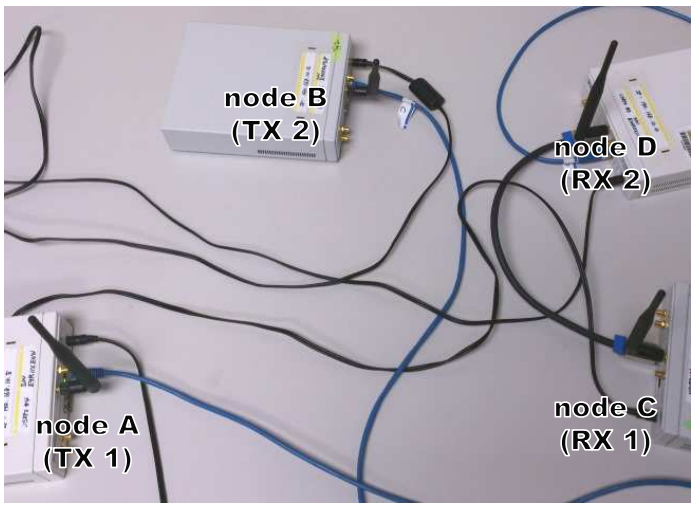

Case 2: $q = 20$ cm

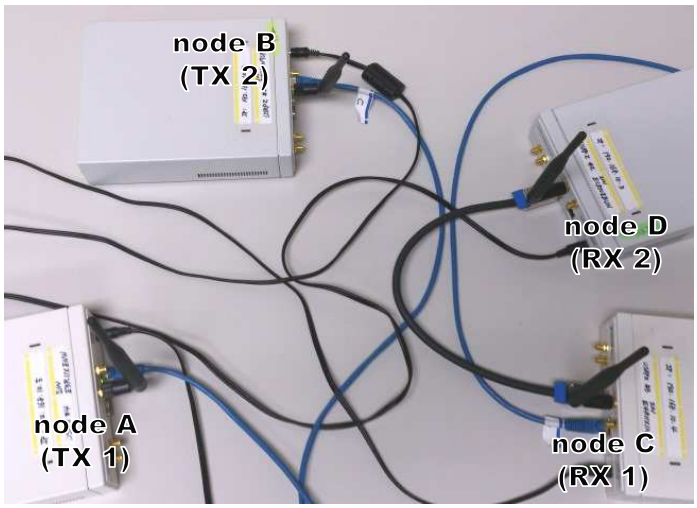

Case 3: $q = -15$ cm

Table 2: Medians and standard deviations of the estimated Q-ranges in the RIPS from the experiments.

	RIPS-u		RIPS-sq	
	median (cm)	st. dev. (cm)	median (cm)	st. dev. (cm)
case 1 (4cm)	4.0046	0.2272	3.9948	0.3181
case 2 (20cm)	19.8753	0.7349	19.9539	1.4232
case 3 (-15cm)	-14.9317	1.3274	-14.9383	1.3341

CHAPTER IV

ASYNCHRONOUS RADIO INTERFEROMETRIC POSITIONING SYSTEM

In this chapter, we present the ARIPS [66] employing dual-tone signaling. The dual-tone signals are designed to accommodate the CFOs and to expand the resolvable range. The range estimates of the RIPS experiences integer ambiguity when the Q-range is larger than the carrier wavelength. For instance, when the carrier frequency of the ranging signal is 2.4 GHz, the resolvable range is 6 cm. Hence, it is necessary for the RIPS to transmit at multiple frequencies to resolve the unknown integer. This increases computational time, which is prohibitive in resource-limited WSNs. With dual-tone signaling, the ARIPS is able to expand the resolvable range and thereby avoids heavy computations required with typical integer ambiguity resolution techniques such as CRT [61, 60] and lattice reduction [25]. In Section 4.1, the signal model and the ranging algorithm of the ARIPS are presented. We develop the frequency estimation technique based on the ESPRIT [1] algorithm [42] to calculate the CFO. Simulation results are presented in Section 4.2 to corroborate the performance of the ARIPS with and without CFOs.

In the ARIPS, each ranging session involves two anchor nodes at known locations as transmitters and the target node as the receiver. Figure 26 shows the ranging model with two transmitters and one receiver. Notice that a number of participating node in a ranging session is reduced from that of the RIPS. When we employ the ranging model with three nodes, we denote the distance between the kth transmitter and the receiver as d_k. We assume that transmitters are perfectly synchronized in

[1] ESPRIT stands for estimation of signal parameters via rotation invariance techniques.

time, but the oscillators may have frequency offsets. No synchronization requirement is imposed on the receiver. At each ranging session, the RD defined as $RD = d_1 - d_2$ is obtained.

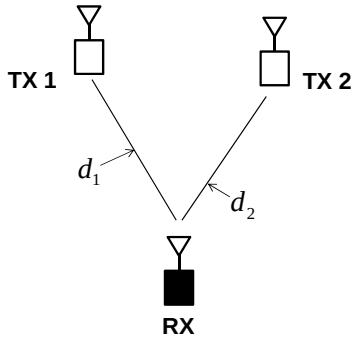

Figure 26: Ranging model with two transmitters and one receiver.

4.1 System Model

Figure 27 shows the block diagram of the ARIPS. Dual-tone signals transmitted at two transmitter nodes are modeled as

$$\begin{aligned} s_1(t) =& a_1 \left\{\cos\left(2\pi f_c t + \theta_1\right) + \cos\left(2\pi(f_c + f_d)t + \theta_1\right)\right\}, \\ s_2(t) =& a_2 \left\{\cos\left(2\pi(f_c + \epsilon)t + \theta_2\right) + \cos\left(2\pi(f_c + f_d + 2\epsilon)t + \theta_2\right)\right\}, \end{aligned} \tag{77}$$

where ϵ is the differential frequency, which can be viewed as the intentional CFO. Frequencies are designed so that $f_c \gg f_d > 3\epsilon$. At a given transmitter, two tones are generated by one oscillator, and thus we assume that two tones from the same transmitter have the same initial phase offset θ_k.

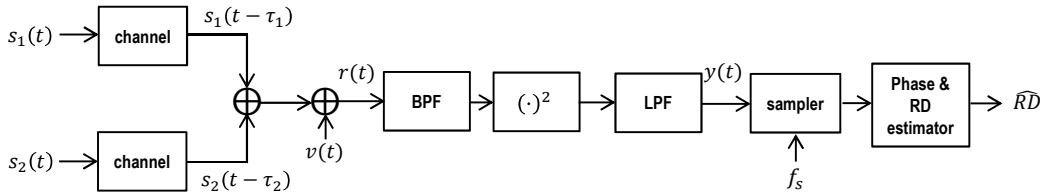

Figure 27: Block diagram of the ARIPS.

The received signal is the composite of two transmitted signals with phase shifts

modeled as

$$r(t) = s_1(t-\tau_1) + s_2(t-\tau_2) + v(t), \tag{78}$$

where $\tau_k = \frac{d_k}{c} + t_0$ with t_0 representing the unknown transmitted time, and $v(t)$ is the additive noise. Since the transmitters are synchronous in time, t_0 is the same at two transmitters. Following the same procedure as the RIPS, the signal is passed through a square-law device as

$$r^2(t) = s_1^2(t-\tau_1) + s_2^2(t-\tau_2) + 2s_1(t-\tau_1)s_2(t-\tau_2) + \widetilde{v}(t), \tag{79}$$

where $\widetilde{v}(t)$ is an aggregated noise. The signal in (79) consists of muliple frequency components along with the DC component. From the first term, $s_1^2(t-\tau_1)$ yields frequency components at $\pm 2f_c$, $\pm 2(f_c+f_d)$, $\pm(2f_c+f_d)$, and $\pm f_d$; $s_2^2(t-\tau_2)$ contains the frequency components at $\pm 2(f_c+\epsilon)$, $\pm 2(f_c+f_d+2\epsilon)$, $\pm(2f_c+f_d+3\epsilon)$, and $\pm(f_d+\epsilon)$; and $s_1(t-\tau_1)s_2(t-\tau_2)$ consists of tones at $\pm\epsilon$, $\pm 2\epsilon$, $\pm(2f_c+\epsilon)$, $\pm(2f_c+f_d+\epsilon)$, $\pm(2f_c+f_d+2\epsilon)$, $\pm 2(f_c+f_d+\epsilon)$, $\pm(f_d-\epsilon)$, and $\pm(f_d+2\epsilon)$. Since we design $f_c \gg f_d > 3\epsilon$, we remove any frequency components beyond 2ϵ by passing the signal through an LPF. Further removing the DC components, a low-frequency differential signal of the ARIPS is achieved as

$$\begin{aligned} y(t) =& a_1a_2\cos(2\pi\epsilon t + 2\pi\left(f_c(\tau_1-\tau_2) - \epsilon\tau_2\right) + \theta_{12}) \\ &+ a_1a_2\cos(4\pi\epsilon t + 2\pi\left((f_c+f_d)(\tau_1-\tau_2) - 2\epsilon\tau_2\right) + \theta_{12}) + \widetilde{v}(t) \\ =& a_1a_2\cos(2\pi\epsilon t - \zeta_1) + a_1a_2\cos(4\pi\epsilon t - \zeta_2) + \widetilde{v}(t), \end{aligned} \tag{80}$$

where $\zeta_1 = -2\pi\left(f_c(\tau_1-\tau_2) - \epsilon\tau_2\right)$, $\zeta_2 = -2\pi\left((f_c+f_d)(\tau_1-\tau_2) - 2\epsilon\tau_2\right)$, and $\theta_{12} = \theta_1 - \theta_2$.

Sampling $y(t)$ at the rate $f_s > 4\epsilon$ and collecting N samples, the sampled signal in the vector format is represented as

$$\mathbf{y} = \mathbf{H}(\boldsymbol{\epsilon})\mathbf{u} + \widetilde{\mathbf{v}}, \tag{81}$$

where $\mathbf{y}$ and $\widetilde{\mathbf{v}}$ are the column vectors consisting of samples from $y(t)$ and $\widetilde{v}(t)$,

respectively,

$$\begin{aligned}\boldsymbol{\epsilon} =& [\epsilon/f_s,\ 2\epsilon/f_s]\,,\\ \mathbf{u} =& a_1 a_2 [e^{-j\zeta_1}, e^{j\zeta_1}, e^{-j\zeta_2}, e^{j\zeta_2}]^T.\end{aligned} \tag{82}$$

4.1.1 With Accurate Knowledge of ϵ

When the value of ϵ is known at the receiver, $\mathbf{H}(\epsilon)$ in (81) is accurately constructed, and an LSE is employed to estimate the phase vector $\mathbf{u}$ as

$$\widehat{\mathbf{u}} = \mathbf{H}^{\dagger}(\boldsymbol{\epsilon})\mathbf{y}. \tag{83}$$

Notice that the phase difference at two tones in $y(t)$ is

$$\begin{aligned}\zeta_1 - \zeta_2 =& 2\pi f_c(\tau_1 - \tau_2) + 2\pi\epsilon\tau_2 - \theta_{12} + 2\pi(f_c + f_d)(\tau_1 - \tau_2) - 2\pi 2\epsilon\tau_2 + \theta_{12}\\ =& 2\pi f_d(\tau_1 - \tau - 2) - 2\pi\epsilon\tau_2\\ =& 2\pi(f_d + \epsilon/2)(\tau_{12}) - 2\pi(\epsilon/2)(\tau_1 + \tau_2).\end{aligned} \tag{84}$$

Since we design the parameters as $f_d \gg \epsilon$, (84) becomes

$$\begin{cases}\zeta_1 - \zeta_2 = -2\pi\epsilon\tau_2 \approx 0, & \tau_1 = \tau_2\\ \zeta_1 - \zeta_2 \approx 2\pi(f_d + \epsilon/2)\tau_{12} = 2\pi(f_d + \epsilon/2)\frac{d_1 - d_2}{c}, & \tau_1 \neq \tau_2.\end{cases} \tag{85}$$

and hence, we arrive at

$$\frac{RD}{c} = \frac{\zeta_1 - \zeta_2}{2\pi(f_d + \epsilon/2)}. \tag{86}$$

Using (86), the RD estimator for the ARIPS is given as

$$\widehat{RD} = \frac{c}{2\pi(f_d + \epsilon/2)} \arg\left\{\left([\widehat{\mathbf{u}}]_1^* + [\widehat{\mathbf{u}}]_2\right)\left([\widehat{\mathbf{u}}]_3 + [\widehat{\mathbf{u}}]_4^*\right)\right\}. \tag{87}$$

According to (87), the resolvable range of the ARIPS is $c/2(f_d + \epsilon/2)$. Notice that this is independent of the carrier frequency f_c unlike that in the RIPS. Therefore, with the ARIPS, the carrier frequency can be chosen freely without affecting the resolvable range. The frequencies f_d and ϵ are chosen so that we cover the area of interest. In other words, given d_{max} that is the maximum range that we are interested in estimating, we choose the parameters such that $c/2(f_d + \epsilon/2) < d_{max}$.

4.1.2 Without Accurate Knowledge of ϵ

When ϵ is unknown at the receiver, the value of ϵ has to be estimated prior to the phase estimation. To estimate ϵ, the ESPRIT-based technique is presented here as it provides a closed-form solution [42]. The sampled vector $\mathbf{y}$ is rearranged into a matrix $\mathbf{Y}$ as

$$\mathbf{Y} = \begin{bmatrix} [\mathbf{y}]_1 & [\mathbf{y}]_2 & \cdots & [\mathbf{y}]_{N-L+1} \\ [\mathbf{y}]_2 & [\mathbf{y}]_3 & \cdots & [\mathbf{y}]_{N-L+2} \\ \vdots & & \ddots & \vdots \\ [\mathbf{y}]_L & [\mathbf{y}]_{L+1} & \cdots & [\mathbf{y}]_N \end{bmatrix}. \tag{88}$$

A parameter L is generally chosen as $N/3 < L < N/2$ [44]. Let $\mathbf{Y}_1$ and $\mathbf{Y}_2$ be defined as $\mathbf{Y}$ with the last and the first row removed, respectively. Then, it is shown that the eigenvalues of $\mathbf{Y}_1^{\dagger}\mathbf{Y}_2$ are given as $\lambda_1 = e^{j2\pi\epsilon/f_s}$, $\lambda_2 = e^{j2\pi 2\epsilon/f_s}$, $\lambda_3 = e^{-j2\pi\epsilon/f_s}$, and $\lambda_4 = e^{-j2\pi 2\epsilon/f_s}$ [42]. Since $f_s > 4\epsilon$, the estimate of ϵ is achieved as

$$\widehat{\epsilon} = \frac{f_s}{2\pi} \arg(\lambda_2\lambda_3 + \lambda_1^*\lambda_4^*). \tag{89}$$

Using the estimated CFO $\widehat{\epsilon}$, $\mathbf{H}(\widehat{\boldsymbol{\epsilon}})$ where $\widehat{\boldsymbol{\epsilon}} = [\widehat{\epsilon}/f_s,\ 2\widehat{\epsilon}/f_s]^T$ is constructed to estimate the phase vector $\mathbf{u}$, and the RD is calculated by replacing ϵ with $\widehat{\epsilon}$ in (87).

To calculate the location of the receiver, multiple RD measurements are obtained by using different pairs of anchor nodes as transmitters. The RD-based localization algorithm is summarized in Section 3.1.2.

4.2 Simulation Results

The performance of the ARIPS is evaluated through the Monte Carlo simulations. Parameters are chosen as $f_c = 10$ MHz, $f_d = 320$ kHz, and $\epsilon = 120$ Hz. Therefore, the RD can be estimated without ambiguity up to $|c/(2f_d + \epsilon)| = 469$ meters. Furthermore, an approximation error is below 0.053 meters, which is negligibly small compared to the estimating range. The signal length is 100 ms, and for simplicity, we let $a_1 = a_2 = 1$. According to (77), the total transmission power of the ARIPS

is $P_T = a_1^2 + a_2^2$. In the simulation, we assume the noise is AWGN modeled as $v[n] \sim \mathcal{N}(0, \sigma^2)$, and the total noise power is $P_N = 8\sigma^2$. We use the SNR definition in (65). The simulation setup consists of five anchor nodes that are placed at four corners and the center of 100×100 meters square, and the target node is randomly placed inside the square. The RMSE of the RD estimates vs. SNR shown in Figure 28. At each SNR, 2000 iterations are performed. The curve with $\triangle$ marks corresponds to the case where exact ϵ is known, and the line with $\circ$ marks corresponds to the case where estimated ϵ is used for the phase estimation. The performance of the RD estimates with accurate knowledge of ϵ is better than that with estimated ϵ, but both of them achieve a submeter accuracy at high SNR.

The RMSE of the location estimates vs. the SNR is shown in Figure 29. For localization, the constrained-LSE presented in [56] is employed here. The first transmitter node is fixed as the one at the center (the origin) of the square, and the rest of the anchor nodes take turns until the receiver achieves four RD estimates. The result is consistent with Figure 28, and the simulation results confirm that the ARIPS is robust to the CFOs.

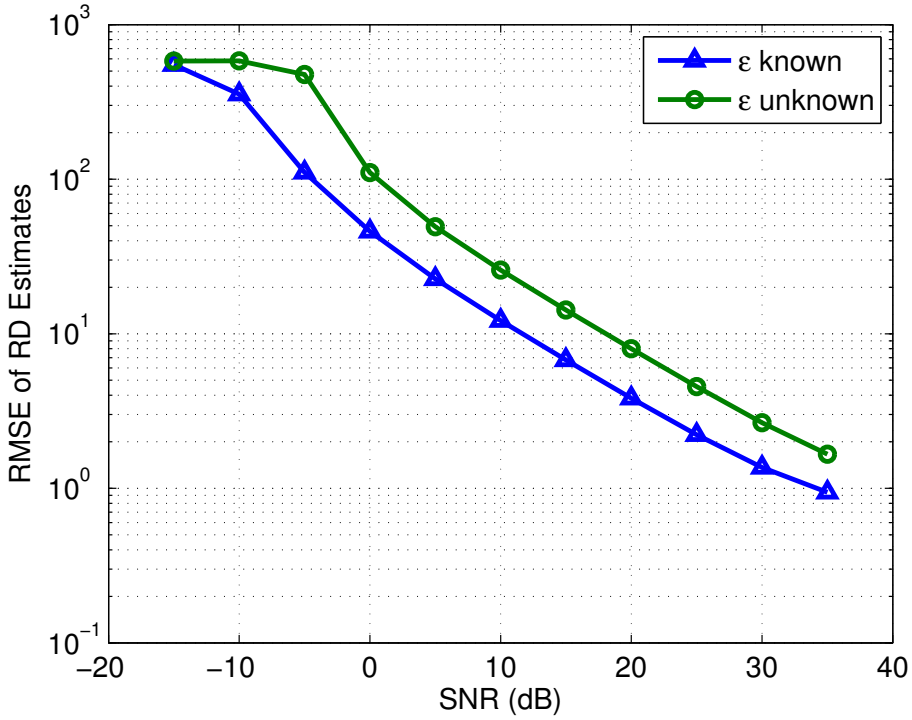

Figure 28: RMSE of RD estimates vs. SNR with the ARIPS.

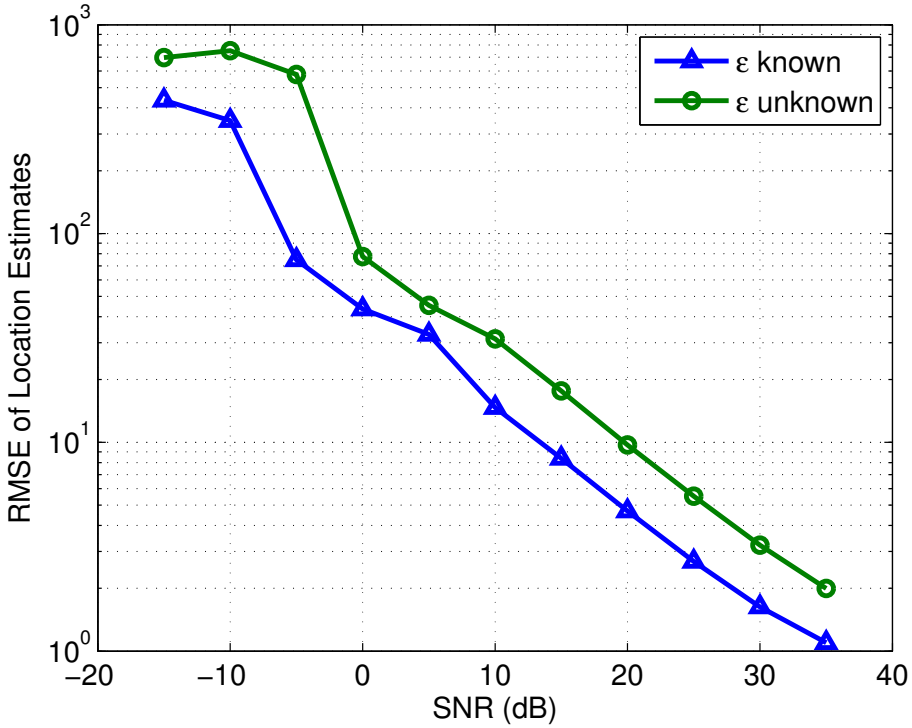

Figure 29: RMSE of location estimates vs. SNR with the ARIPS.

CHAPTER V

SPACE-TIME RADIO INTERFEROMETRIC POSITIONING SYSTEM

In Chapter 4, the ARIPS that uses dual-tone signaling is developed. The estimated RD measurements from two transmitters and a receiver is free of integer ambiguities, and the dual-tone signal is effectively designed to cope with the CFOs. Using the ideas from the ARIPS, we develop the STRIPS [53] in this chapter. The STRIPS employs STC and MMW signaling to accurately estimate the range under fading. In Section 5.1, we describe the system model, the ranging algorithm and parameter design requirements of the STRIPS. Simulation results are presented in Section 5.2, where we compare the STRIPS and the RIPS and confirm the robustness of the STRIPS against fading. Moreover, the STRIPS is implemented on hardware, and experiments performed in [51] are summarized in Section 5.3.

5.1 System Model

In the STRIPS, we employ the ranging model with two transmitters and a receiver in Figure 26. The transmitters are anchor nodes at known locations, and the receiver is the target node. Anchor nodes are assumed to be perfectly synchronized in time, and they transmit sinusoidal signals at two time slots with different frequencies. At the first time slot, TX 1 and TX 2 transmit at frequencies f_c and $f_c + f_d$, respectively, where f_c is the carrier frequency, f_d is the frequency difference between signals transmitted by two nodes. At the second time slot, TX 1 transmits at $f_c - f_d$, and TX 2 transmits at f_c. For brevity, let us denote designed transmitting frequencies at the kth anchor node at the ith time slot as $f_{k,i}$. Hence, at the first time slot,

$f_{1,1} = f_c + f_d$ and $f_{2,1} = f_c$. The sequence of transmitted frequencies is summarized in Table 3. Here, the carrier frequency is $f_c \sim 60$ GHz and we design frequencies as $f_c \gg f_d$. Details of the parameter design in the STRIPS is discussed later.

Table 3: Transmitting frequencies in the STRIPS.

	TX 1	TX 2
time slot 1	$f_c + f_d$	f_c
time slot 2	f_c	$f_c - f_d$

The transmitting signals at the ith time slot from the kth anchor node is modeled as

$$s_{k,i}(t) = a_k \cos\left(2\pi(f_{k,i} + \epsilon_k)t + \theta_k\right), \tag{90}$$

where a_k and θ_k are the amplitude and initial phase offset of the signal transmitted by the kth node, and ϵ_k is the unknown frequency offset at the kth node due to the unreliability of the oscillator.

Block diagram of the STRIPS is illustrated in Figure 30. Transmitted signals go through the channel and are delayed by a respective propagation delay. The received signal at the target node is the sum of those two faded signals plus an additive noise.

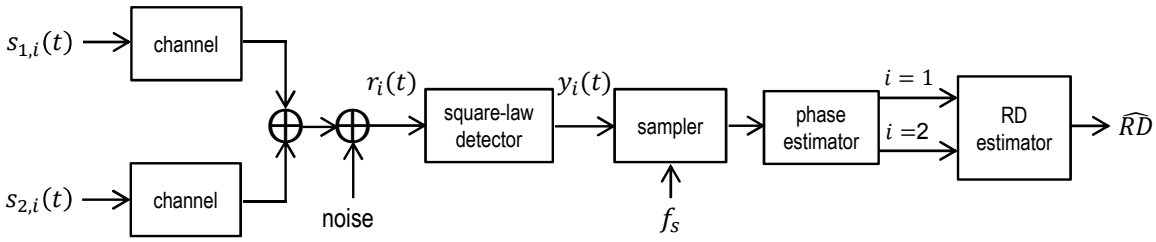

Figure 30: Block diagram of the STRIPS.

5.1.1 Range Estimation

The received signals at the ith time slot is expressed as

$$\begin{aligned} r_i(t) &= \sum_{k=1}^{2} a_k h_k \cos\left(2\pi(f_{k,i}+\epsilon_k)t - 2\pi(f_{k,i}+\epsilon_k)\left(\frac{d_k}{c}+t_0+(i-1)T_0\right)+\beta_k+\theta_k\right)+v_i(t) \\ &= \sum_{k=1}^{2} a_k h_k \cos\left(2\pi(f_{k,i}+\epsilon_k)t-\eta_{k,i}\right)+v_i(t), \end{aligned} \tag{91}$$

where $\eta_{k,i} = 2\pi(f_{k,i}+\epsilon_k)\left(\frac{d_k}{c}+t_0+(i-1)T_0\right)-\beta_k-\theta_k$ with h_k and β_k represent the gain and the phase of the channel between the kth transmitter and the receiver, respectively, T_0 is the known time interval between two time slots, and $v_i(t)$ is the additive noise at the ith time slot. As the transmitters are assumed to be synchronous in time, the transmitting instance t_0 is the same at two transmitted signals. According to Figure 30, the received signal is squared as

$$\begin{aligned} r_i^2(t) =& \sum_{k=1}^{2} a_k^2 h_k^2 \cos^2\left(2\pi(f_{k,i}+\epsilon_k)t-\eta_i\right) \\ &+ 2a_1a_2h_1h_2\cos\left(2\pi(f_{1,i}+\epsilon_1)t-\eta_{1,i}\right)\cos\left(2\pi(f_{2,i}+\epsilon_2)t-\eta_{2,i}\right)+\widetilde{v}_i(t) \\ =& \sum_{k=1}^{2}\frac{a_k^2h_k^2}{2}\left\{1+\cos\left(4\pi(f_{k,i}+\epsilon_k)t-\eta_{k,i}\right)\right\} \\ &+ a_1a_2h_1h_2\cos\left(2\pi(f_{1,i}+f_{2,i}+\epsilon_1+\epsilon_2)t-\eta_{1,i}-\eta_{2,i}\right) \\ &+ a_1a_2h_1h_2\cos\left(2\pi(f_d+\epsilon_0)t-\psi_i\right)+\widetilde{v}_i(t) \end{aligned} \tag{92}$$

where $\tilde{v}_i(t)$ is the aggregated noise at the ith time slot, $\psi_i = \eta_{1,i}-\eta_{2,i}$ and $\epsilon_0 = \epsilon_1-\epsilon_2$. The squared signal in (92) contains the frequency components at $\pm2(f_{k,i}+\epsilon_k)$, $\pm(f_{1,i}+f_{2,i}+\epsilon_1+\epsilon_2)$, and $\pm(f_d+\epsilon_0)$. The CFO is typically much smaller than the carrier frequency s.t. $f_c \gg \epsilon_0$. Since $f_c \gg f_d$, the LPF following the square-law device removes the frequency components beyond $\pm(f_d+\epsilon_0)$. Also removing the DC terms from (92), we obtain a low-frequency differential signal of the STRIPS as

$$y_i(t) = a_1a_2h_1h_2\cos\left(2\pi(f_d+\epsilon_0)t-\psi_i\right)+\widetilde{v}_i(t). \tag{93}$$

The signal $y_i(t)$ in (93) is sampled at the rate $f_s > 2f_d$. Collected N samples at each time slot is expressed in a matrix-vector form as

$$\mathbf{y}_i = \mathbf{H}(\overline{f}_d + \overline{\epsilon}_0)\mathbf{w}_i + \widetilde{\mathbf{v}}_i, \tag{94}$$

where $\overline{\epsilon}_0 = \epsilon_0/f_s$ and

$$\mathbf{w}_i = a_1 a_2 h_1 h_2 [e^{-j\psi_i},\ e^{j\psi_i}]^T. \tag{95}$$

5.1.2 Synchronous Transmitters

When the transmitters are synchronized, $\epsilon_0 = \epsilon_1 - \epsilon_2 = 0$, and $\mathbf{H}(\overline{f}_d + \overline{\epsilon}_0) = \mathbf{H}(\overline{f}_d)$ in (94) is accurately constructed at the receiver. Thus, we employ an LSE to estimate the phase vector $\mathbf{w}_i$ as

$$\widehat{\mathbf{w}}_i = \mathbf{H}^{\dagger}(\overline{f}_d)\tilde{\mathbf{y}}_i. \tag{96}$$

From $\eta_{k,i} = 2\pi(f_{k,i} + \epsilon_k)\left(\frac{d_k}{c} + t_0 + (i-1)T_0\right) - \beta_k - \theta_k$, notice that

$$\begin{aligned}
\psi_1 - \psi_2 =& \eta_{1,1} - \eta_{2,1} - \eta_{1,2} + \eta_{2,2} \\
=& 2\pi(f_{1,1} + \epsilon_1)\left(\frac{d_1}{c} + t_0\right) - 2\pi(f_{2,1} + \epsilon_2)\left(\frac{d_2}{c} + t_0\right) \\
& - 2\pi(f_{1,2} + \epsilon_1)\left(\frac{d_1}{c} + t_0 + T_0\right) + 2\pi(f_{2,2} + \epsilon_2)\left(\frac{d_2}{c} + t_0 + T_0\right) \\
=& 2\pi(f_d + \epsilon_1)\left(\frac{d_1}{c} + t_0\right) - 2\pi(f_d + \epsilon_2)\left(\frac{d_2}{c} + t_0\right) \\
& - 2\pi(f_c + \epsilon_1)T_0 + 2\pi(f_c - f_d + \epsilon_2)T_0 \\
=& 2\pi(f_d + \epsilon)\frac{RD}{c} - 2\pi(f_d + \epsilon)T_0,
\end{aligned} \tag{97}$$

where $RD = d_1 - d_2$. Therefore, the general RD estimator of the STRIPS is derived as

$$\widehat{RD} = \frac{c}{2\pi f_d}\arg\{e^{j2\pi(f_d+\epsilon_0)T_0}([\widehat{\mathbf{w}}_1]_1^* + [\widehat{\mathbf{w}}_1]_2)([\widehat{\mathbf{w}}_2]_1 + [\widehat{\mathbf{w}}_2]_2^*)\}. \tag{98}$$

When the transmitters are synchronized, $\epsilon_0 = 0$ in (98).

5.1.3 Asynchronous Transmitters

When transmitters are asynchronous, $\epsilon_0 \neq 0$. In such a case, we first estimate ϵ_0 from the received signal to accurately construct $\mathbf{H}(\overline{f}_d + \overline{\epsilon}_0)$. Since the size of ϵ_0 is small, we employ the ESPRIT-based algorithm to estimate ϵ_0, similarly to the frequency estimation in the ARIPS presented in Section 4.1.2. We first construct a shift-invariant matrix $\mathbf{Y}^{(i)}$ from $\mathbf{y}_i$ as in (88) and remove the first and last rows to construct two matrices $\mathbf{Y}_1^{(i)}$ and $\mathbf{Y}_2^{(i)}$, respectively. The general eignvenvalues of the matrix pair $\left\{\mathbf{Y}_1^{(i)}, \mathbf{Y}_2^{(i)}\right\}$ are given by $\lambda_1^{(i)} = e^{j2\pi(f_d+\epsilon_0)/f_s}$ and $\lambda_2^{(i)} = e^{-j2\pi(f_d+\epsilon_0)/f_s}$. Hence, the CFO estimate based on $\mathbf{y}_i$ is given as

$$\widehat{\epsilon}_0^{(i)} = \frac{f_s}{2\pi} \arg\left\{\lambda_1^{(i)} + \left(\lambda_2^{(i)}\right)^*\right\} - f_d. \tag{99}$$

We take an average of two CFO estimates and obtain the final CFO estimate as $\widehat{\epsilon}_0 = \frac{1}{2}\left(\widehat{\epsilon}_0^{(1)} + \widehat{\epsilon}_0^{(2)}\right)$. Using this estimated CFO $\widehat{\epsilon}_0$, we estimate the phase vector $\widehat{\mathbf{w}}_i$ as

$$\widehat{\mathbf{w}}_i = \mathbf{H}^\dagger(\overline{f}_d + \widehat{\overline{\epsilon}}_0)\tilde{\mathbf{y}}_i, \tag{100}$$

where $\widehat{\overline{\epsilon}} = \widehat{\epsilon}/f_s$. Then, we estimate the RD with the estimator in (98) by replacing ϵ_0 with $\widehat{\epsilon}_0$.

5.1.4 Parameter Design

To achieve the robustness to fading, we need to design parameters in the STRIPS carefully. In the following, we discuss the parameter design requirements based on the resolvable range and channel conditions.

Integer ambiguity From (98), the estimated RD is free of the integer ambiguity when $|RD| < c/2f_d$. Notice that the resolvable range $c/2f_d$ is independent of the carrier wavelength. Hence, despite of the transmission with a carrier wavelength in the order of millimeters, we are able to avoid the integer ambiguity with the STC. Let us denote the maximum range to estimate as d_{max}, which can either be determined

by the maximum distance that the signal can reach or physical constraints such as room size or walls. Then, as long as we set

$$f_d < \frac{c}{2d_{max}}, \tag{101}$$

we can avoid the integer ambiguity in the RD estimates of the STRIPS.

Channel coherence bandwidth Another constraint we need to consider in the system parameter design is based on channel conditions. Frequencies of the signals transmitted at two time slots from a given node are apart by f_d. Hence, to assume that signals transmitted by a given transmitter are experiencing the same fading channel, f_d should be smaller than $\mathcal{B}_l$, where $\mathcal{B}_l$ is the coherence bandwidth of the channel between the lth anchor node and the target node. Thus, we impose a following condition:

$$f_d < \min\{\mathcal{B}_1, ..., \mathcal{B}_M\}, \tag{102}$$

where $l = 1, ..., M$ with M being the total number of anchor nodes. A typical value of $\mathcal{B}_l$ in MMW bands is few MHz [37]. Combining (101) and (102), we arrive at

$$f_d < \min\left\{\frac{c}{2d_{max}}, \mathcal{B}_1, \ ..., \ \mathcal{B}_M\right\}. \tag{103}$$

Channel coherence time While (103) defines the upper bound on the choice of f_d, the lower bound is given in terms of the channel coherence time $\mathcal{T}_l$. To assume that signals at two time slots are experiencing the same fading channel, we have to keep the total time required to complete two transmissions $T_s + T_0$ smaller than $\mathcal{T}_l$. The channel coherence time of MMW bands is few milliseconds in the indoor environment [37]. Since the low-frequency differential signal $y_m(t)$ in (93) is sampled at the rate $f_s > 2f_d$, it is intuitive that $T_s > 1/f_d$. In other words, smaller f_d requires a longer signal length. Assuming that time slots are contiguous (i.e. $T_0 = T_s$) and N samples

are collected at each time slot, the lower bound on the choice of f_d is expressed in terms of $\mathcal{T}_l$ as

$$\frac{2N}{\min\{\mathcal{T}_1,\ ...\mathcal{T}_M\}} < f_d. \tag{104}$$

5.2 Simulation Results

In this section, the performance of the STRIPS is evaluated and compared with the RIPS [29] through Monte-Carlo simulations. Five anchor nodes placed at corners and the center of the 10×10 meters square and the target node randomly placed within the square at each Monte-Carlo run. At each SNR, 2000 iterations are performed. For the STRIPS, we choose $f_c = 60$ GHz, $f_d = 5$ MHz, the signal length of $T_s = 1$ μs, $f_s = 100$ MHz, and $T_0 = T_s$. With $f_d = 5$ MHz, we are able to estimate the RD up to ± 30 meters without the integer ambiguity. Each ranging session takes 2 μs, which is less than the typical coherence time in MMW bands. We assume that the CFO up to 1ppm of the carrier, and hence the maximum CFO is 60 kHz.

To compare the STRIPS with the RIPS, we kept the resolvable range in two systems the same. Therefore, we let the carrier frequency of the RIPS to be 5 MHz. The frequency difference at two transmitters is 1.3 kHz, and the same number of samples as the STRIPS is obtained at the rate 26 kHz. We employed the RD-based localization in [56] for both the RIPS and the STRIPS to estimate the position of the target node. The localization technique using the RD-based algorithm for the Q-range is described in Section 3.1.2. We let the transmitting power at two transmitters to be equal and hence, $a_1 = a_2 = 1$. In both the STRIPS and the RIPS, the total transmitting power is given as $P_T = a_1^2/2 + a_2^2/2$. With the noise $v_i[n] \sim \mathcal{N}(0, \sigma^2)$, the total noise power is $P_N = 4\sigma^2$, and we use the SNR defined in (65).

Performance of the STRIPS and the RIPS without fading We first consider the case where there is only the AWGN and no fading. The RMSE of the location

estimates vs. SNR for the STRIPS and the RIPS is shown in Figure 31. When there is no CFO, the STRIPS and the RIPS achieve similar performance. The STRIPS effectively accommodates CFOs, and both systems achieve a submeter accuracy when SNR > -5 dB.

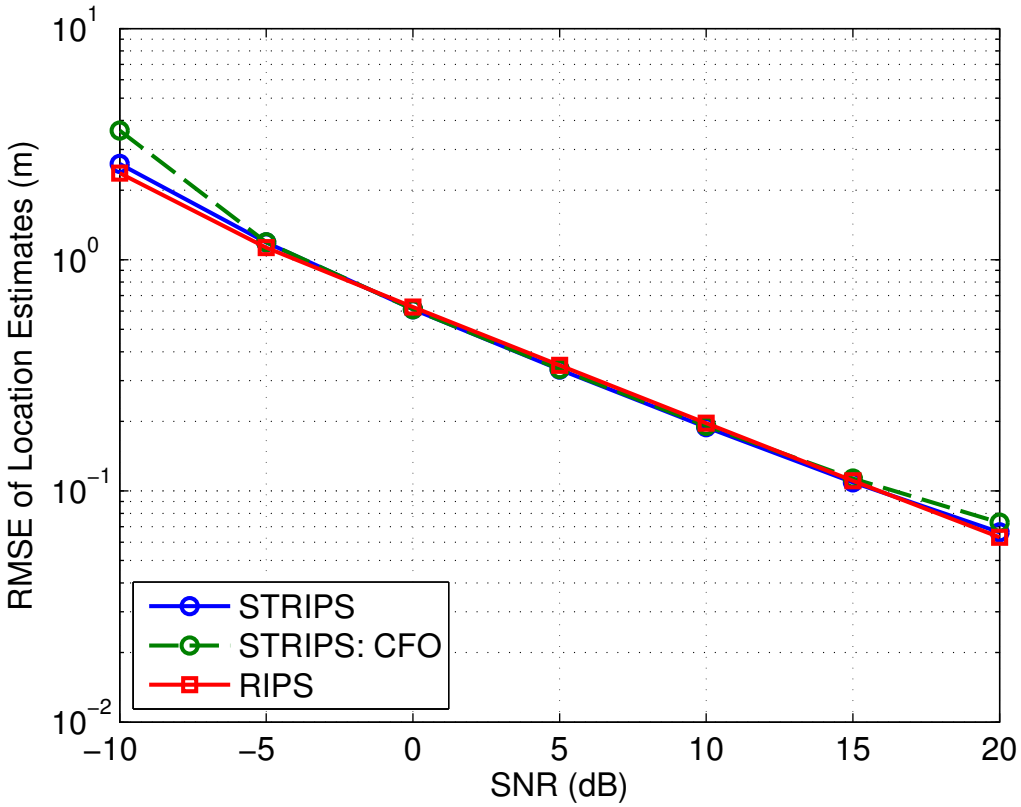

Figure 31: RMSE of location estimate with the STRIPS vs. SNR under the AWGN channel.

Performance of the STRIPS and the RIPS with fading To consider the fading channel, we assume the LOS between the anchors and the target node as the MMWs have strong power attenuation. Thus, we use the Rician channel model. The measurements in a home and an office environments in the 60 GHz band are shown to have high Rician factor in the range of $8 \sim 11$ dB [45]. In the simulation, we set the factor to be 10 dB, and the channel coefficients are randomly generated at

each iteration. The RMSE of the location estimates under fading for the RIPS and the STRIPS is shown in Figure 32. While the RIPS fails to work under the fading scenario, the STRIPS effectively cancels the fading effects and obtains the accurate location information.

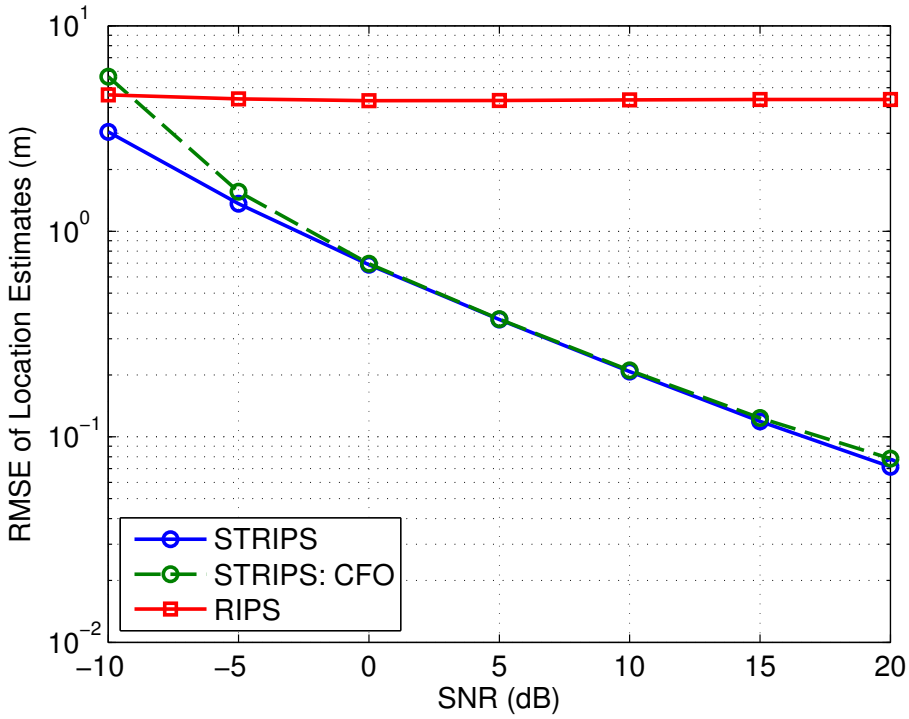

Figure 32: RMSE of location estimates with the STRIPS vs. SNR under the flat-fading channel.

5.3 Hardware Implementation

In this section, we present the hardware implementation of the STRIPS and experimental results.

5.3.1 Hardware Tools and Setup

The overall experimental setup is shown in Figure 33. Transmitters are placed on a desk at fixed locations, and the receiver is placed on a cart for mobility. The close-up picture of the transmitters is shown in Figure 34. A signal generator generates a

sinusoidal signal at designed frequencies. It is connected to the transmitter, where the signal is transmitted with a horn antenna. At each time slot, the frequency at each signal generator is manually adjusted to change from one frequency to the other. Since the signal is highly directional, antenna angles are carefully adjusted to point directly to the receiver horn antenna. Moreover, the initial phase at each transmitter is calibrated to prevent two signals to interfere destructively.

At the receiver, an envelope detector is used to obtain a low-frequency differential signal. The output of the envelope detector is connected to an oscilloscope, which samples the signal at $f_s = 20$ GHz. The sampled signal is saved as data, and the post processing and the RD estimations are performed offline using MATLAB.

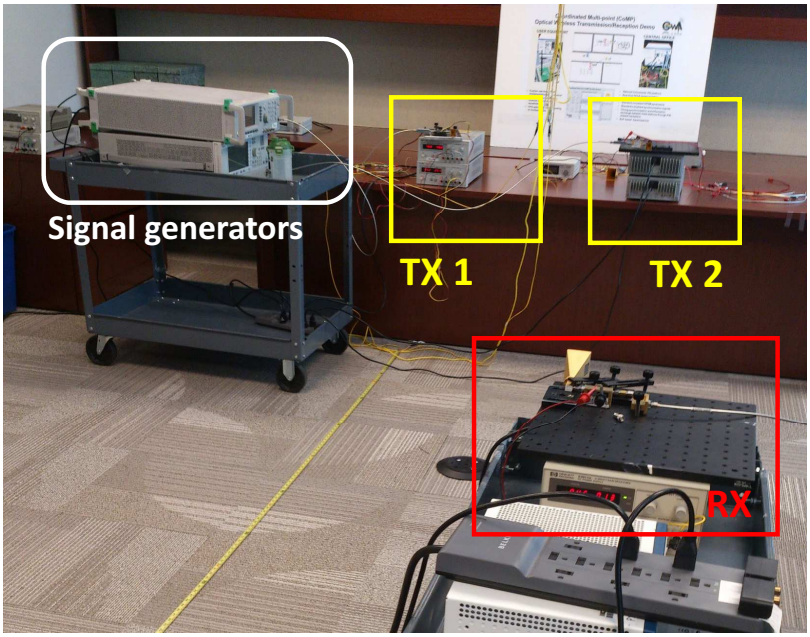

Figure 33: Experimental setup of the STRIPS.

Relative locations of transmitters and the receiver are illustrated in Figure 35. The distance between two transmitters is fixed at 78 cm, and the receiver is always placed straight from TX 2. Three nodes forms a right triangle so that the true RD is easily calculated.

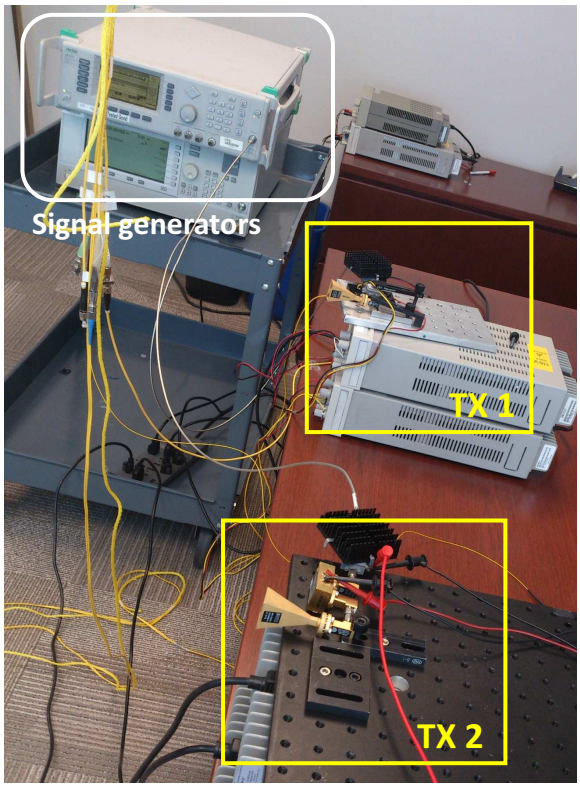

Figure 34: Experimental configurations of the transmitters of the STRIPS.

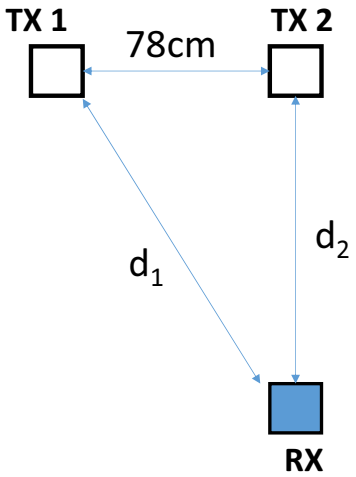

Figure 35: Relative locations of the transmitters and the receiver in the experiments for the STRIPS.

5.3.2 Experimental Results

Ranging performance vs. distance In the first experiment, we change the distance between TX 2 and the receiver (d_2). The parameters used in the experiment are summarized in Table 4. The frequency difference is fixed at $f_d = 40$ MHz. When the environment is rich in multipath, f_d should be kept under a few MHz. However, in this experimental setup, the equipments are placed at the center of the office away from the walls and obstacles, and antennas are raised well above the ground. Therefore, we assume that the effect of multipath is negligibly small in this experiments. Moreover, when the resolvable range is considered, $f_d = 40$ MHz allows the receiver to uniquely estimate the RD up to 7.5 m, which is sufficiently large in this setup.

Table 4: Experimental parameters of the STRIPS.

f_c	59.2 GHz
f_s	20 GHz
N	2184

Since the frequencies are manually adjusted, precise T_0 is not known. Hence, we used first N samples to calibrate the offset from unknown T_0 at each given d_2. Furthermore, changing the location of the receiver requires antenna angles and initial phase at transmitters to be changed accordingly. At given d_2, 60 RD estimates are achieved, and the RMSE of the RD estimates vs. d_2 is plotted in Figure 36. Because the angles of antennas are adjusted at each d_2, the curve is not smooth. However, the general trend can still be observed. Recall that the signals are highly directional in this experiments. Therefore, when the receiver is close to the transmitters, transmitters are spread apart from the receiver's perspective. In other words, the transmitter and receiver horn antennas are not facing to each other, resulting in a low received power at the receiver. As the receiver moves further away from the transmitters, the effect of the path loss becomes more significant than the effect from the antenna angles,

causing the performance to degrade. Since this implementation is merely a prototype, we employ horn antennas to ensure so that the signals reach the receiver. In practical scenarios, approaches such as beamforming [69] can be employed to overcome the strong path loss of the MMWs.

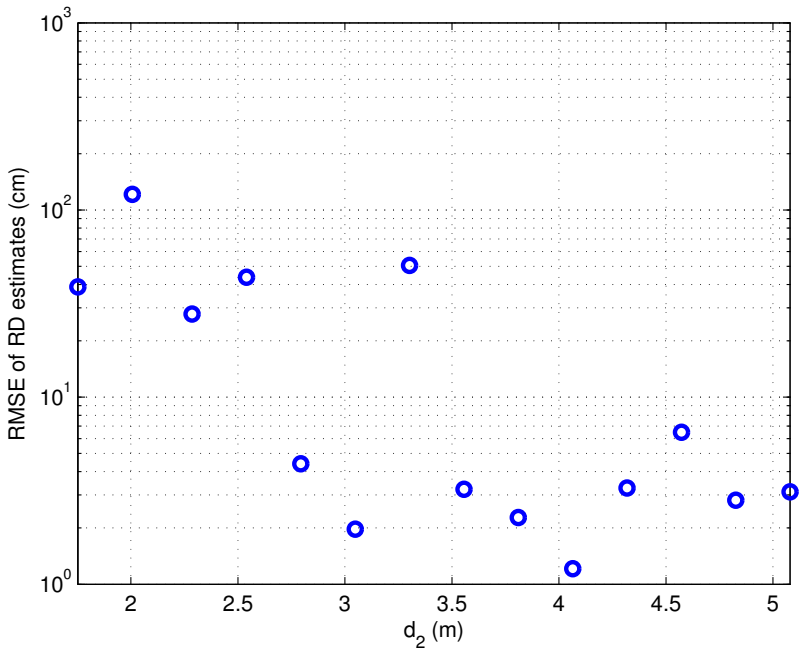

Figure 36: RMSE of the RD estimates vs. d_2 from the experiments of the STRIPS.

Ranging performance vs. f_d In the second experiment, we fixed the receiver location and varied f_d. The distance d_2 is fixed at 4 m, and other parameters are the same as listed in Table 4. Again, 60 RD estimates are obtained at each f_d, and the RMSE of the RD estimates vs. f_d is shown in Figure 37. The performance improves as the value of f_d increases. However, recall that larger f_d results in a smaller resolvable range, and the integer ambiguity is likely to occur. Furthermore, small f_d is desirable when the environment is rich in multipath. Nevertheless, Figure 37 shows that the STRIPS can achieve a submeter accuracy when $f_d > 1$ MHz, and we have successfully validated the superior performance of the STRIPS through experiments.

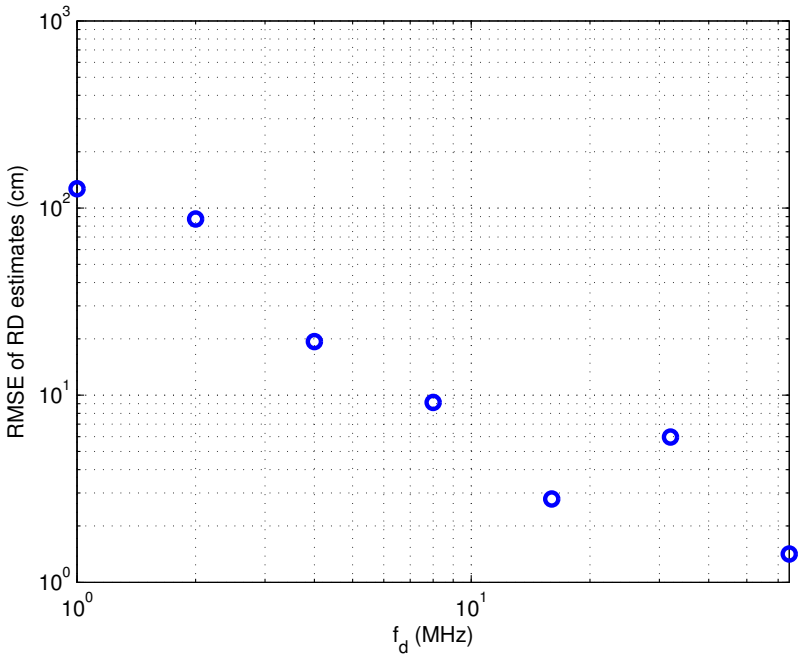

Figure 37: RMSE of the RD estimates vs. f_d from the experiments of the STRIPS.

CHAPTER VI

ACCURATE INDOOR POSITIONING SYSTEM

In Chapter 5, we developed the STRIPS that effectively cancels the fading effect by using STC and MMWs. Recall that for accurate ranging under fading, the STRIPS requires a ranging session to complete within a channel coherence time. To realize this with its system design, LOs at two transmitters have to switch the frequency every milliseconds or less in synchronized manner. This is a difficult task and often prohibitive in conventional communication systems.

In this chapter, we present AIPS to solve the feasibility issue of the STRIPS. Instead of directly generating the MMWs, the signal with a STC is first produced at the IF band, and it is upconverted to the MMW band. We employ the same ranging model as the STRIPS in Figure 26 with three nodes. The ranging procedure of the AIPS is illustrated as a block diagram in Figure 38. Notice that the AIPS follows a generic communication model and thus can be integrated to existing communication devices. A modulating signal is a sinusoidal signal at different frequencies that are designed to cancel the phase shifts due to fading, similarly to the STRIPS. Since the STC is applied in the modulating signal, the LO frequency is fixed. We consider two modulation schemes that can be chosen depending on hardware availability. A ranging signal with a carrier allows the receiver to use a low-complexity envelope detector at the receiver. When a square-law device or a mixer is available at the receiver, a ranging signal with a suppressed carrier can be employed to improve the power efficiency. The first scheme is analogous to amplitude modulation (AM), and the latter produces a double-sideband suppressed carrier (DSB-SC) signal. Details of the ranging signal model is explained in Section 6.1. In Section 6.2, the performance

of the AIPS is confirmed via simulations. We implement the AIPS with an envelope detector on the hardware, and the results are presented in Section 6.3.

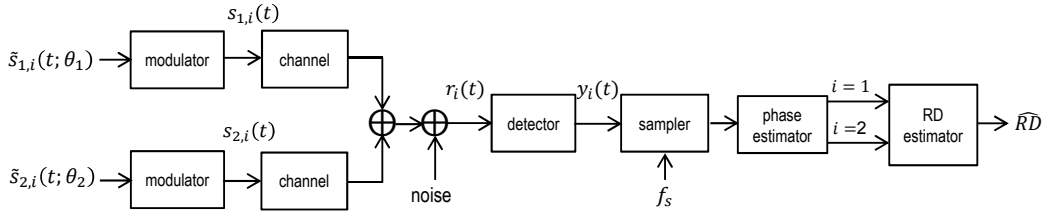

Figure 38: Block diagram of the AIPS.

6.1 System Model in the AIPS

The modulating signal generated at the kth transmitter in the ith time slot $\tilde{s}_{k,i}(t)$ is given as

$$\tilde{s}_{k,i}(t;\theta_k) = \cos(2\pi f_{k,i}t + \theta_k), \tag{105}$$

where θ_k denotes the initial phase offset, and $f_{k,i}$ is the frequency at the kth transmitter at the ith time slot. The frequency $f_{k,i}$ at each transmitter and time slot for the AIPS is summarized in Table 5, where f_0 denotes the center frequency of the IF band, and f_d represents the frequency difference at two transmitters.

Table 5: Frequencies of the modulating signal in the AIPS.

	node 1	node 2
time slot 1	$f_0 + f_d$	f_0
time slot 2	f_0	$f_0 - f_d$

Similarly to the STRIPS, we assume that two transmitters are synchronized in time. The parameter design in the AIPS follows that of the STRIPS described in Section 5.1.4. Hence, the frequency difference f_d is chosen to be less than the coherence bandwidth of the channel, and the ranging session completes within a channel coherence time. Since the STC is used in the modulating signal, the frequency can be changed digitally without changing the LO frequency. Hence, it is easier to fulfill the requirements with the AIPS than with the STRIPS. In addition to the parameter

design requirements in Section 5.1.4, we impose $f_d \ll f_0 \ll f_c$ for accurate detection of signals at the receiver.

6.1.1 Ranging Signal with the Carrier

Let us first consider the ranging signal for envelope detection. A signal transmitted by the kth transmitter at the ith time slot is represented as

$$s_{k,i}(t) = a_k \cos(2\pi f_c t + \overline{\phi}_k) \left(b_k \widetilde{s}_{k,i}(t;\theta_k) + 1\right), \tag{106}$$

where b_k is a modulation index such that $0 < b_k \leq 1$, and $\overline{\theta}_k$ is the initial phase offset of the LO of the kth transmitter. Notice that this is the same as conventional AM. At the receiver, two ranging signals add up, and the composite signal is given as

$$r_i(t) = \sum_{k=1}^{2} a_k h_k \cos\left(2\pi f_c t + \overline{\gamma}_{1,i}\right) \left(b_k \cos\left(2\pi f_{k,i} t + \gamma_{k,i}\right) + 1\right) + v_i(t), \tag{107}$$

where $\overline{\gamma}_{k,i} = -2\pi f_c \left(\frac{d_k}{c} + t_0 + (i-1)T_0\right) + \overline{\phi}_k + \beta_k$, and $\gamma_{k,i} = -2\pi f_{k,i} \left(\frac{d_k}{c} + t_0 + (i-1)T_0\right) + \theta_k$.

To avoid two signals from adding destructively, we need to adjust the initial phase $\overline{\phi}_k$ of the LO at the kth transmitters so that $\overline{\gamma}_{1,i} = \overline{\gamma}_{2,i}$. For simplicity, let us assume that $\overline{\gamma}_{k,i} = 0$. Then, the received signal $r_i(t)$ in (107) is simplified as

$$\begin{aligned} r_i(t) &= \cos\left(2\pi f_c t\right) \sum_{k=1}^{2} a_k h_k \left(b_k \widetilde{s}_{k,i}(t;\gamma_{k,i}) + 1\right) \\ &= \cos\left(2\pi f_c t\right) \left(\overline{s}_i(t) + \sum_{k=1}^{2} a_k h_k\right), \end{aligned} \tag{108}$$

where $\overline{s}_i(t) = \sum_{k=1}^{2} a_k h_k b_k \widetilde{s}_{k,i}(t;\gamma_{k,i})$. For simplicity, the noise term is ignored in (108). Notice that the envelope of $r_i(t)$ in (108) is $\overline{s}_i(t)$ plus the DC component $\sum_{k=1}^{2} a_k h_k$. Thus, removing the DC component from the envelope extracted with the envelope detector yields $\overline{s}_i(t)$.

When $\overline{s}_i(t)$ is sampled at the rate f_s and N samples are collected at each time slot, we obtain

$$\overline{\mathbf{s}}_i = \mathbf{H}(\mathbf{f}_i)\overline{\mathbf{w}}_i, \tag{109}$$

where $\overline{\mathbf{s}}_i$ is a column vector containing N samples from $\overline{s}_i(t)$,

$$\begin{aligned}\mathbf{f}_i =&[\overline{f}_{1,i},\ \overline{f}_{2,i}]^T,\\ \overline{\mathbf{w}}_i =&\left[a_1h_1b_1e^{j\gamma_{1,i}},\ a_1h_1b_1e^{-j\gamma_{1,i}},\ a_2h_2b_2e^{j\gamma_{2,i}},\ a_2h_2b_2e^{-j\gamma_{2,i}}\right]^T.\end{aligned} \tag{110}$$

Assuming that $\mathbf{H}(\mathbf{f}_i)$ can be accurately constructed at the receiver, we estimate the phase vector $\mathbf{z}_i$ with an LSE as

$$\widehat{\overline{\mathbf{w}}}_i = \mathbf{H}^{\dagger}(\mathbf{f}_i)\overline{\mathbf{s}}_i. \tag{111}$$

Recall that $\gamma_{k,i} = -2\pi f_{k,i}\left(\frac{d_k}{c} + t_0 + (i-1)T_0\right) + \theta_k$. From the following relationship,

$$\begin{aligned}&-\gamma_{1,1} + \gamma_{1,2} + \gamma_{2,1} - \gamma_{2,2}\\ &=2\pi(f_{1,1} - f_{1,2})\left(\frac{d_1}{c} + t_0\right) - 2\pi(f_{2,1} - f_{2,2})\left(\frac{d_2}{c} + t_0\right) - 2\pi(f_{1,2} - f_{2,2})T_0\\ &=2\pi f_d\left(\frac{d_1}{c} + t_0\right) - 2\pi f_d\left(\frac{d_2}{c} + t_0\right) - 2\pi(f_{1,2} - f_{2,2})T_0\\ &=2\pi f_d\frac{RD}{c} - 2\pi f_dT_0,\end{aligned} \tag{112}$$

we derive the estimator for the RD from $\widehat{\overline{\mathbf{w}}}_i$ as

$$\widehat{RD} = \frac{c}{2\pi f_d}\arg\left\{e^{j2\pi f_dT_0}\alpha_{1,1}\alpha_{2,1}^*\alpha_{1,2}^*\alpha_{2,2}\right\}, \tag{113}$$

where $\alpha_{i,k} = \left[\widehat{\overline{\mathbf{w}}}_i\right]_{2k-1}^* + \left[\widehat{\overline{\mathbf{w}}}_i\right]_{2k}$.

Let us also consider two other detectors, namely, a square-law and product detectors, to obtain $\overline{s}_i(t)$. With the square-law detector, the received signal $r_i(t)$ is squared as

$$\begin{aligned}r_i^2(t) =&\cos^2(2\pi f_ct)\left(\overline{s}_i(t) + \sum_{k=1}^{2}a_kh_k\right)^2\\ =&\left(\frac{1}{2} + \frac{1}{2}\cos(2\pi 2f_ct)\right)\left(\overline{s}_i(t) + \sum_{k=1}^{2}a_kh_k\right)^2\\ =&\frac{1}{2}\left(\overline{s}_i^2(t) + 2\overline{s}_i(t)\sum_{k=1}^{2}a_kh_k + \left(\sum_{k=1}^{2}a_kh_k\right)^2\right) + \frac{1}{2}\cos(2\pi 2f_ct)\left(\overline{s}_i(t) + \sum_{k=1}^{2}a_kh_k\right)^2.\end{aligned} \tag{114}$$

Again, the noise term is ignored for simplicity. Filtering out the frequency components around $2f_c$ with an LPF and removing the DC components, we arrive at

$$y_i^{(sq)}(t) = \frac{1}{2}\overline{s}_i^2(t) + \overline{s}_i(t)\left(\sum_{k=1}^{2} a_k h_k\right). \tag{115}$$

When $\frac{1}{2}|\overline{s}_i^2(t)| \ll |\overline{s}_i(t)|\left(\sum_{k=1}^{2} a_k h_k\right)$ and thus $|\overline{s}_i(t)|/(2\sum_{k=1}^{2} a_k h_k) \ll 1$, (115) can be approximated as $y_i^{(sq)}(t) \approx \left(\sum_{k=1}^{2} a_k h_k\right)\overline{s}_i(t)$. To analyze this condition, consider the case when $a_k = a$, $b_k = b$ and $h_k = h$. Then, the condition simplifies to

$$\frac{b}{4}\left(\widetilde{s}_{1,i}(t;\gamma_{1,i}) + \widetilde{s}_{2,i}(t;\gamma_{2,i})\right) \ll 1. \tag{116}$$

When this condition is not satisfied, the distortion in the demodulated signal becomes large, leading to a large error in the range estimation.

When the product detector is employed at the receiver, the received signal $r_i(t)$ in (108) is passed through a mixer at the frequency f_c. The output of the mixer is given as

$$\begin{aligned} 2\cos(2\pi f_c t) r_i(t) =& 2\cos^2(2\pi f_c t)\left(\overline{s}_i(t) + \sum_{k=1}^{2} a_k h_k\right) \\ =& \left(1 + \cos(2\pi 2 f_c t)\right)\left(\overline{s}_i(t) + \sum_{k=1}^{2} a_k h_k\right). \end{aligned} \tag{117}$$

The LPF following the mixer removes the frequency components around $2f_c$, and further removing the DC components, we achieve $y^{(mx)} = \overline{s}_i(t)$.

Let us analyze the transmitting power required at each time slot by considering a simple case where $a_k = a$ and $b_k = b$. From (106), the total transmission power is given as

$$P_T = \frac{a_1^2}{4}(b_1^2 + 2) + \frac{a_2^2}{4}(b_2^2 + 2) = \frac{a^2}{2}(b^2 + 2), \tag{118}$$

and the total power of tones that carry range information is

$$P_S = \frac{a_1^2 b_1^2 + a_2^2 b_2^2}{4} = \frac{a^2 b^2}{2}. \tag{119}$$

Hence, the power efficiency of the ranging signal with the carrier is

$$\frac{P_S}{P_T} = \frac{(a^2 b^2)/2}{a^2(b^2 + 2)/2} = \frac{b^2}{b^2 + 2}. \tag{120}$$

Since $b \leq 1$, the maximum efficiency we can achieve is 1/3. Nevertheless, this signal model is advantageous since we can employ simple and low-cost envelope detector at the receiver.

6.1.2 Ranging Signal with the Suppressed Carrier

When a square-law device or a mixer is available at the receiver, we can improve the power efficiency by modifying the transmitting signal model as

$$s_{k,i}(t) = a_k \cos(2\pi f_c t + \overline{\theta}_k)\widetilde{s}_{k,i}(t). \tag{121}$$

The signal no longer has a carrier and has a similar structure as the DSB-SC signal. To differentiate between two ranging signal models, we will call the ranging signal with the carrier as the AM signal and that with the suppressed carrier (SC) as the SC signal. The total transmission power of the SC signal is

$$P_T = \frac{a_1^2}{4} + \frac{a_2^2}{4}. \tag{122}$$

Here, $P_S = P_T$, and the efficiency is 1. The received signal at the ith time slot is given as

$$r_i(t) = \sum_{k=1}^{2} a_k h_k \cos\left(2\pi f_c t + \overline{\gamma}_{k,i}\right) \cos\left(2\pi f_{k,i} t + \gamma_{k,i}\right) + v_i(t), \tag{123}$$

and adjusting $\overline{\theta}_k$ to achieve $\overline{\gamma}_{k,i} = 0$, the received signal becomes

$$\begin{aligned} r_i(t) &= \cos\left(2\pi f_c t\right) \left(a_1 h_1 \widetilde{s}_{1,i}(t;\gamma_{1,i}) + a_2 h_2 \widetilde{s}_{2,i}(t;\gamma_{2,i})\right) + v_i(t) \\ &= \cos\left(2\pi f_c t\right) \breve{s}_i(t) + v_i(t), \end{aligned} \tag{124}$$

where

$$\breve{s}_i(t) = a_1 h_1 \widetilde{s}_{1,i}(t;\gamma_{1,i}) + a_2 h_2 \widetilde{s}_{2,i}(t;\gamma_{2,i}). \tag{125}$$

Previously with the AM signal, a square-law device is used to extract the modulating signal with the phase shift. With the SC signal, we use a square-law device to obtain a low-frequency differential signal of $\breve{s}_i(t)$, similar to the original RIPS [29].

The squared received signal $r_i(t)$ in (124) is given as

$$\begin{aligned} r_i^2(t) &= \cos^2(2\pi f_c t)\, \breve{s}_i^2(t) \\ &= \left(\frac{1}{2} + \frac{1}{2}\cos(4\pi f_c t)\right) \breve{s}_i^2(t). \end{aligned} \tag{126}$$

Again, the noise term in (126) is ignored for brevity. Recall that $\breve{s}_i(t)$ consists of two tones at $f_{1,i}$ and $f_{2,i}$. Thus, $\breve{s}_i^2(t)$ contains the frequency components at $\pm 2f_0$, $\pm f_0$, $\pm 2(f_0 + f_d)$, $\pm 2(f_0 - f_d)$, and $\pm f_d$ along with a DC component. Since we design frequencies such that $f_d \ll f_0 \ll f_c$, we can remove the frequency components beyond f_d with an LPF. Further removing the DC components, we obtain

$$y_i^{(sq)}(t) = \frac{1}{2} a_1 a_2 h_1 h_2 \cos(2\pi f_d t + \gamma_{1,i} - \gamma_{2,i}). \tag{127}$$

Sampling this low-frequency differential signal at the rate f_s and stacking collected N samples vertically, we arrive at

$$\mathbf{y}_i = \mathbf{H}(\bar{f}_d)\widetilde{\mathbf{w}}_i, \tag{128}$$

where

$$\widetilde{\mathbf{w}}_i = \frac{1}{2} a_1 a_2 h_1 h_2 [e^{j(\gamma_{1,i} - \gamma_{2,1})},\ e^{-j(\gamma_{1,i} - \gamma_{2,1})}]^T. \tag{129}$$

Recall that $\bar{f}_d = f_d / f_s$. We estimate the phase vector $\widetilde{\mathbf{w}}_i$ with an LSE as

$$\widehat{\widetilde{\mathbf{w}}}_i = \mathbf{H}^\dagger(\bar{f}_d)\mathbf{y}_i, \tag{130}$$

and from the relationship between the phase $\gamma_{k,i}$ and the RD given in (112), we have the RD estimator for the SC signal with the square-law detector as

$$\widehat{RD} = \frac{c}{2\pi f_d} \arg\left\{ e^{j2\pi f_d T_0} \left(\left[\widehat{\widetilde{\mathbf{w}}}_1\right]_1^* + \left[\widehat{\widetilde{\mathbf{w}}}_1\right]_2 \right) \left(\left[\widehat{\widetilde{\mathbf{w}}}_2\right]_1 + \left[\widehat{\widetilde{\mathbf{w}}}_2\right]_2^* \right) \right\}. \tag{131}$$

The demodulation of the SC signal with a product detector is similar to that of the AM signal. Passing the signal through a mixer and removing the frequency components around $2f_c$ with the LPF, we obtain $\breve{s}_i(t)$. The demodulated signal is sampled at the rate f_s, which can be expressed as

$$\breve{\mathbf{s}}_i = \mathbf{H}(\mathbf{f}_i)\breve{\mathbf{z}}_i, \tag{132}$$

where

$$\breve{\mathbf{z}}_i = [a_1 h_1 e^{j\gamma_{1,i}},\ a_1 h_1 e^{-j\gamma_{1,i}},\ a_2 h_2 e^{j\gamma_{2,i}},\ a_2 h_2 e^{-j\gamma_{2,i}}]^T. \tag{133}$$

Notice that the elements of $\breve{\mathbf{z}}_i$ only differ from those of $\overline{\mathbf{w}}_i$ in (110) by real constants, and the phase is the same. Hence, we can employ the RD estimator in (113) by replacing $\widehat{\overline{\mathbf{w}}}_i$ with $\widehat{\breve{\mathbf{z}}}_i$, where $\widehat{\breve{\mathbf{z}}}_i = \mathbf{H}^{\dagger}(\mathbf{f}_i)\breve{\mathbf{s}}_i$.

6.2 Simulation Results

In this section, we evaluate the performance of the AIPS through Monte-Carlo simulations. Frequencies are $f_c = 60$ GHz, $f_0 = 500$ MHz, $f_d = 5$ MHz, and $f_s = 4(f_0 + f_d) = 2.02$ GHz. With $f_d = 5$ MHz, one can uniquely estimate the RD up to 30 m, which is enough to cover the communication range of typical MMWs. The signal length is $T_s = 1\mu$s. We designed the time slots to be contiguous, and thus $T_0 = T_s$. For comparison, we also simulated the STRIPS with the same parameters. The received signal in (108) and (124) contains the AWGN with zero mean and variance σ^2. We let $a_k = a$ and $b_k = b$, and the SNR is defined as (65). The total transmission power P_T is given in (118) and (122) for the AM and SC signals, respectively. We assume the noise as the AWGN with variance $\sigma_i^2 = \sigma^2$ for $i = 1, 2$, and the total noise power is $P_N = 10\sigma^2$ for the AM signal and $P_N = 8\sigma^2$, for the SC signal. Again, the LOS is assumed, and we used the Rician channel model to simulate the fading channel.

6.2.1 Performance of Range Estimation

Let us first observe the ranging performance of the AIPS. The RMSE of RD estimates vs. SNR as defined in (65) is shown Figure 39. Distances d_1 and d_2 are generated randomly from a uniform distribution over $[0, 10]$ m, and 200 iterations are performed at each SNR. With the AM signal, we tested $b = 0.5$ and $b = 1$, and three detectors: the envelope detector ("AM-en"), the square-law detector ("AM-sq"), and the product detector ("AM-mx"). When the envelope detector is considered, the envelope of

the signal $r_i(t)$ is calculated as [39, p. 21]

$$Env\left\{r_i(t)\right\} = \sqrt{\left(\mathcal{H}\left(r_i(t)\right)\right)^2 + r_i(t)}, \tag{134}$$

where $\mathcal{H}(\cdot)$ is the Hilbert transform. Since we cannot use the envelope detector with the SC signal, only the square-law ("SC-sq") and the product ("SC-mx") detectors are simulated. In Figure 39, the ranging performance with the AM signal is worse than that with the SC signal in general. This is because the SC signal has better power efficiency over the AM signal. Likewise, the AM signal with $b = 1$ outperforms that with $b = 0.5$. Notice that the curve of the STRIPS lies in between that of "AM-mx" with $b = 1$ and those corresponding to SC signals. Overall, the AIPS with SC signals has better performance than the AIPS with AM signals or the STRIPS.

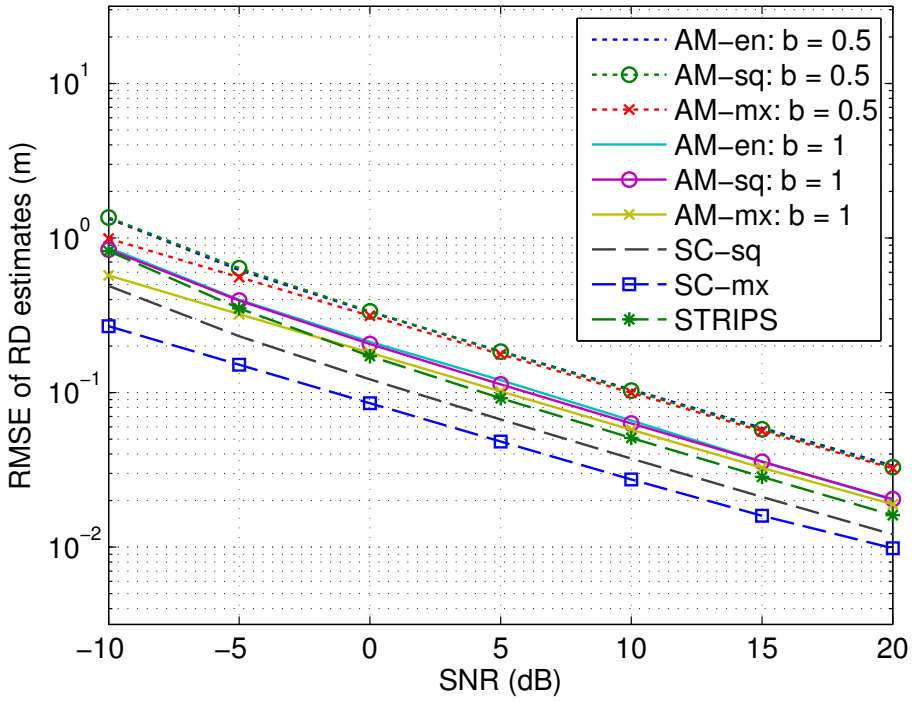

Figure 39: RMSE of the RD estimates with the AIPS vs. SNR.

Comparing different detectors with the AM signal, the envelope and square-law detectors have similar performance and the product detector has a performance gain over the other two. This is because both envelope and square-law detectors suffer

from noise amplification. The effect of the noise amplification can be observed in the low SNR region, where the performance gap between the envelope and square-law detectors and the product detector is wider than at the higher SNR. For the same reason, the product detector performs better than the square-law detector with the SC signal.

Figures 40 and 41 illustrate how parameters affect the ranging performance of the AIPS. In both figures, the SNR is fixed at 10 dB. In Figure 40, the RMSE of the RD estimates vs. SNR is plotted, and the curves are mostly flat. In other words, the performance is not affected by the choice of f_0. This is favorable since it allows us to freely choose the IF band based on the hardware limitations. On the other hand, Figure 41 shows that the performance improves as f_d increases. Hence, f_d should be chosen as close to the upper-bound in (103) as possible.

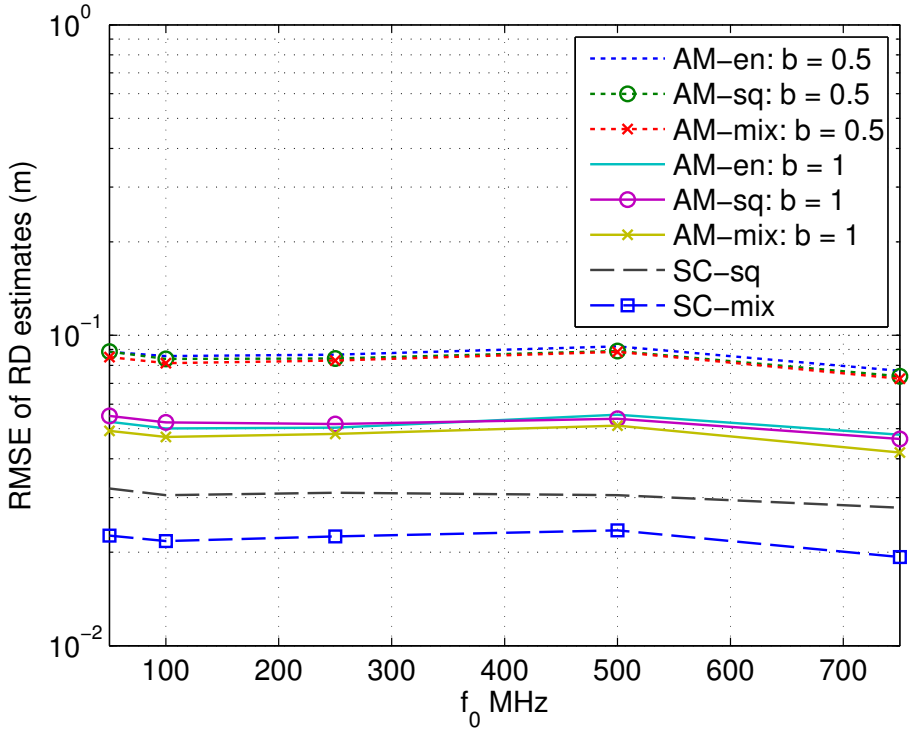

Figure 40: RMSE of the RD estimates with the AIPS vs. f_0.

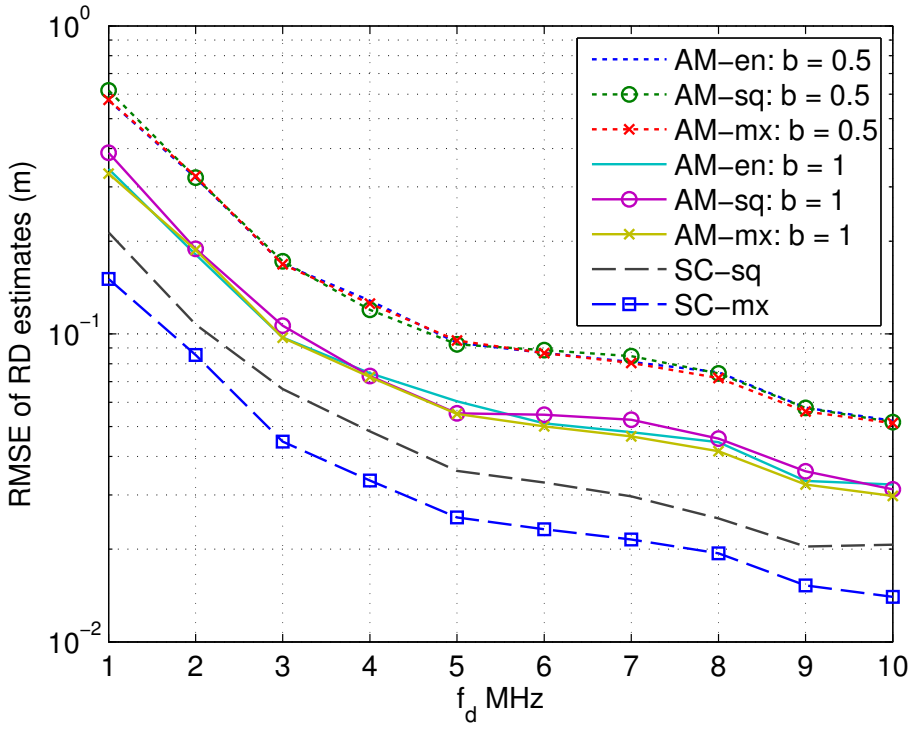

Figure 41: RMSE of the RD estimates with the AIPS vs. f_d.

6.2.2 Performance of Location Estimation

To estimate the location of the target node, we placed five anchor nodes at the center and four corners of 10×10 meters square and deployed the target node randomly inside the square. The anchor node at the center is fixed as the first transmitter, and other four nodes take turns to perform the ranging. Once we obtained four RD measurements, we used a constrained-LS estimator described in [56]. The RMSE of the location estimates vs. SNR is plotted in Figure 42. At each SNR, 200 iterations are performed. The relative performance agrees with the ranging performance shown previously in Figure 39. Figure 43 illustrates an example of the estimated locations. Squares represent the anchors nodes, and circles are target node locations. With the AM signal, we only plotted the case when $b = 1$. Although at some locations, "AM-en" (denoted with $\triangle$ marks) exhibits larger error than other schemes at some locations, all the modulation and detection combinations perform well in general.

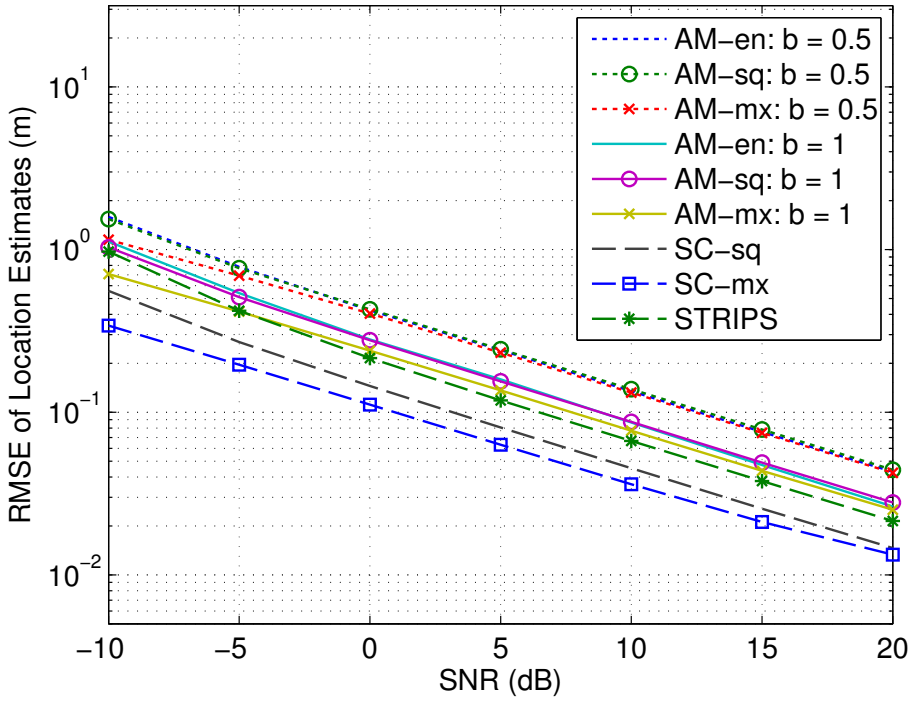

Figure 42: RMSE of the location estimates with the AIPS vs. SNR.

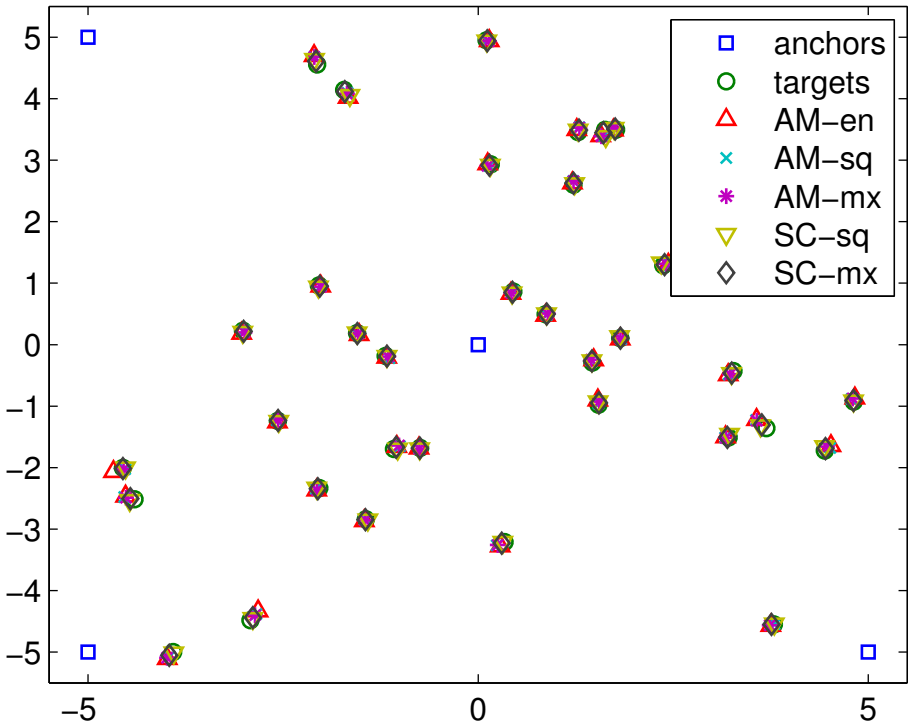

Figure 43: An example of the estimated locations with the AIPS at SNR = 10 dB.

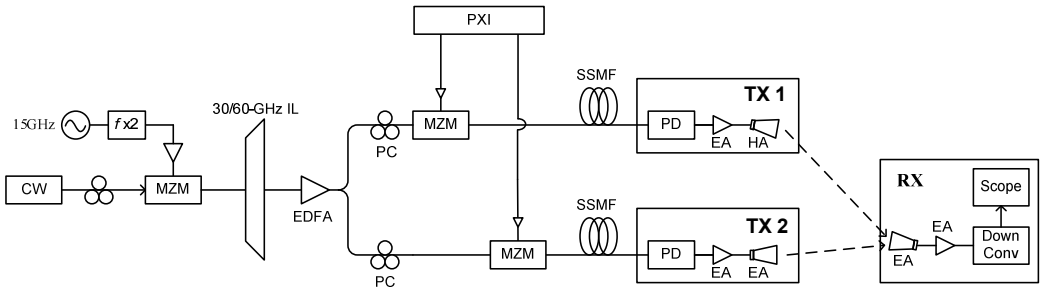

Figure 44: Block diagram of the experimental setup. (CW: continuous-wave laser, MZM: Mach-Zehnder modulator, IL: interleaver, EDFA: Erbium-doped fiber amplifier, PC: polarization controller, SSMF: standard single mode fiber, PD: photodiode, EA: electrical amplifier, HA: horn antenna)

6.3 Hardware Implementation

To further evaluate our proposing system, we implemented the AIPS on hardware. Since we only have an envelope detector in hardware, we employed the AM signal for ranging. We demonstrate the prototype and evaluate the RD estimation performance under various scenarios.

6.3.1 Hardware Setup and System Model

In the experiment, we use the National Instruments PCI eXtensions for Instrumentation (NI PXI) to generate the modulating signal in the IF band. With PXI, we can smoothly transfer between time slots by digitally switching the frequency of the modulating signals. To generate 60 GHz carrier frequency, we use optical components and techniques as shown in Figure 44 similarly to the experimental testbeds demonstrated in [8]. A carrier signal is generated by first applying a Mach-Zehnder modulator (MZM) to a continuous wave (CW) for intensity modulation. The output is then applied to an optical interleaver (IL) and amplified with Erbium-doped fiber amplifier (EDFA). The generated MMW signal is split into two links to be modulated with signals generated by PXI, and radio-over-fiber (RoF) links carry these modulated signals to the transmitters.

Generation modules are placed in the central office away from the lab, where we

have performed the experiments. In the lab, the transmitters and receiver are placed as illustrated in Figure 45. The transmitters are placed on the table, and the receiver horn antenna is directly facing TX 1. An output of the receiver is connected to an oscilloscope as in Figure 46, where the signal samples are collected. The range estimation is performed offline. The initial phase at the transmitters is adjusted to avoid severe destructive interference of the signals at the receiver. The adjustment of the phase is done each time when we initiate a ranging session with a new set of parameters

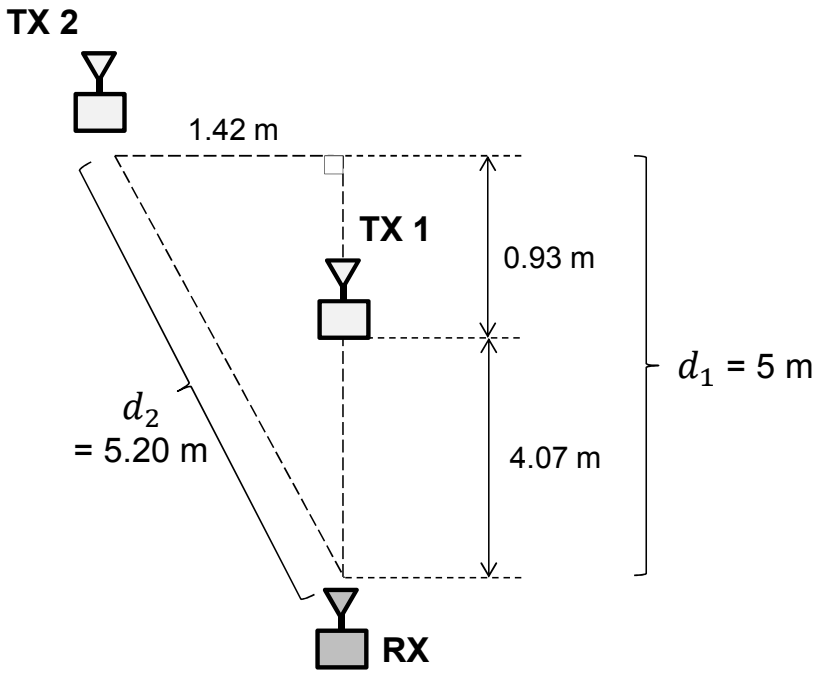

Figure 45: Relative locations of the nodes of the experiments of the AIPS.

6.3.2 Experimental Results

Using this testbed, we conduct three experiments to analyze how f_d, f_0, and optical received power (ORP) impact the ranging performance in the proposed system. We first varied f_d and set $f_c = 60$ GHz, $f_0 = 500$ MHz, $f_s = 10$ GHz, $N = 20000$, and $T_0 = 10\mu$s. Thus, time slots are contiguous. The ORP of TX 1 and TX 2 are 1.72 dBm and 1.36 dBm, respectively. Figure 47 shows the RMSE of the RD

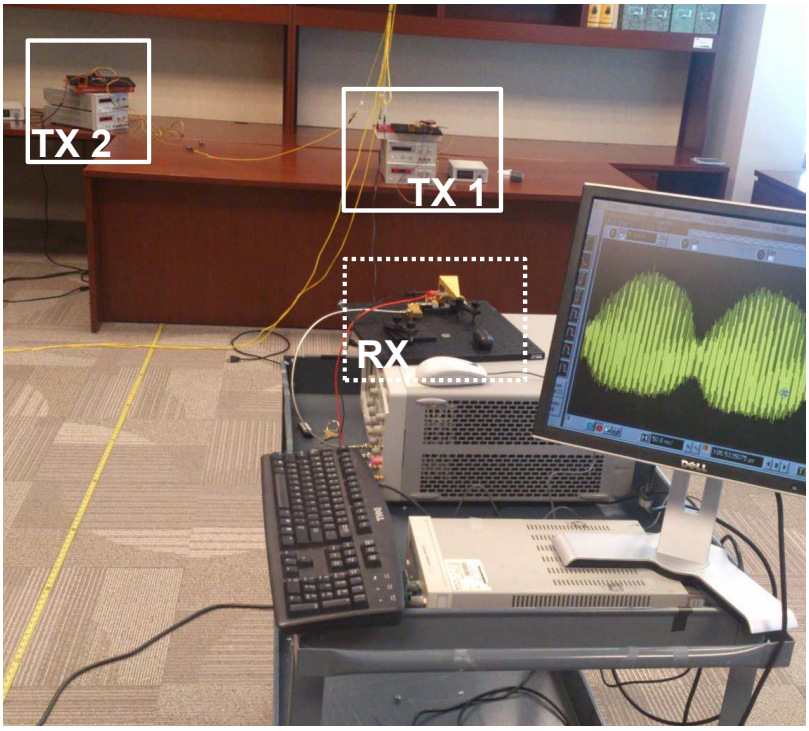

Figure 46: Experimental setup in the lab for the AIPS.

estimates vs. f_d. The ranging performance improves as f_d increases, which agrees with the simulation results in Figure 47. A submeter accuracy is achieved when $f_d > 3$ MHz, which is well below a channel coherent bandwidth of typical offices. Secondly, we varied f_0 and fixed $f_d = 5$ MHz, the RMSE of the RD estimates vs. f_0 is shown in Figure 48. As we have shown with the simulations, f_0 does not have a large impact on the ranging performance. Thirdly, we conducted the experiments varying the ORP, which is shown in Figure 49. The x-axis is the ORP of TX 1, and the ORP of TX 2 is 0.36 dBm less than the corresponding ORP. Frequencies f_0 and f_d are fixed at 500 MHz and 5 MHz, respectively. As expected, higher received power yields better ranging performance.

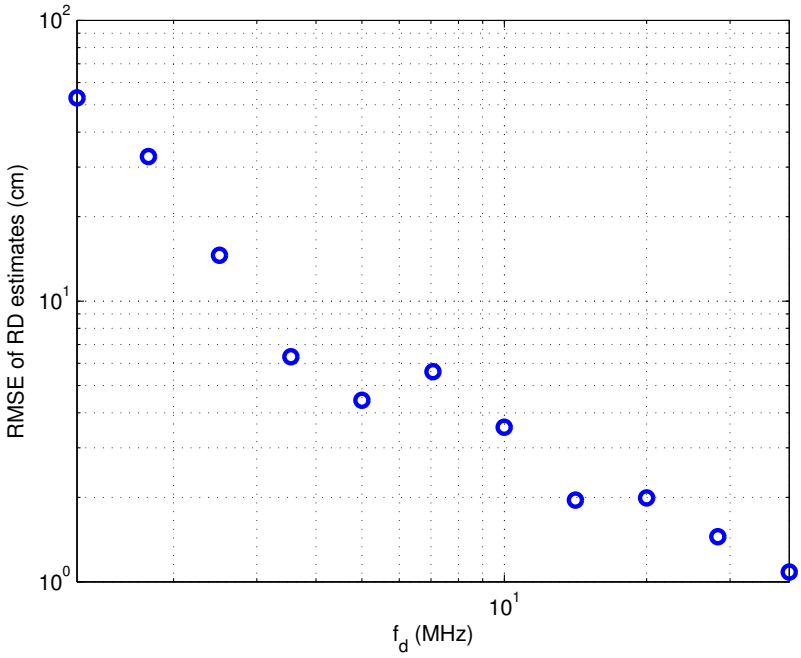

Figure 47: RMSE of the RD estimates vs. f_d from the experiments of the AIPS.

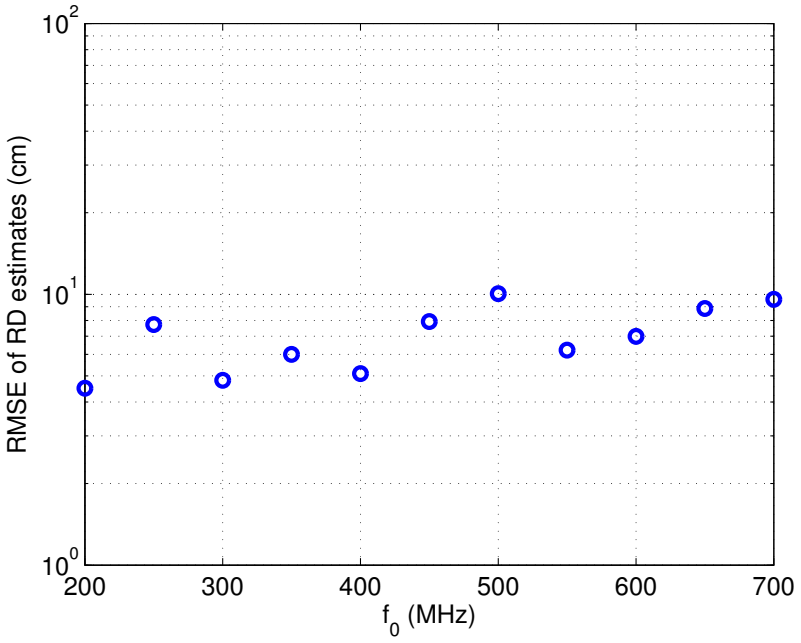

Figure 48: RMSE of the RD estimates vs. f_0 from the experiments of the AIPS.

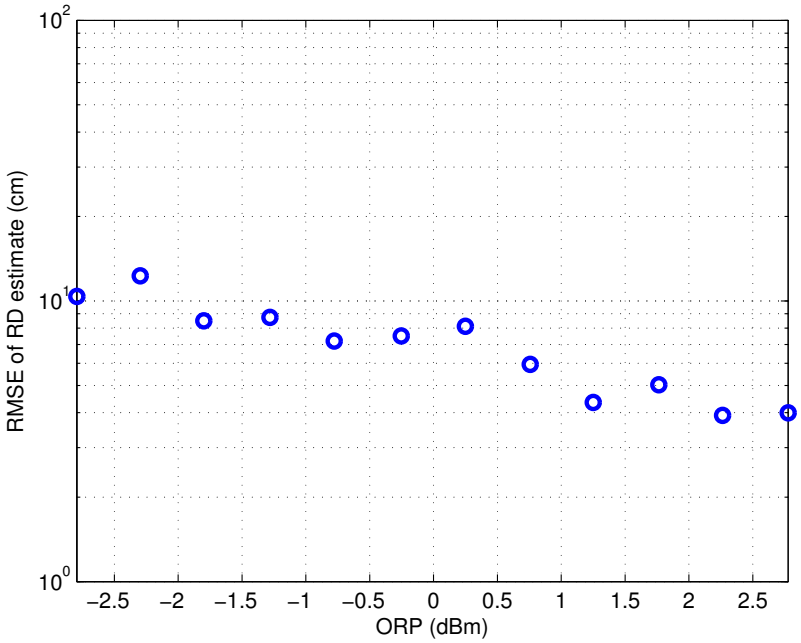

Figure 49: RMSE of the RD estimates vs. ORP from the experiments of the AIPS.

CHAPTER VII

CONCLUSIONS

7.1 Contributions

In this dissertation, we developed indoor localization systems based on the RIPS using STC and MMW signaling. Primary contributions of this dissertation are as follows:

- An undersampling receiver for the RIPS was proposed to enhance the performance of the original RIPS by avoiding noise power augmentation. We developed the mathematical framework for the original RIPS (RIPS-sq) to facilitate the comparison with the proposed RIPS (RIPS-u). Numerical examples were presented to show the performance gain of the RIPS-u over the RIPS-sq. To further confirm the efficiency of our proposed receiver, both the RIPS-u and the RIPS-sq were implemented on USRPs.

- We performed theoretical analysis on the RIPS-u and the RIPS-sq to clarify the relationship between the localization accuracy and parameters. We considered the case the noise is white and colored. We focused on the analysis of the ranging performance of the RIPS, where we derived the CRLBs of the Q-range estimates. The second-order statistics of the aggregated noise in the RIPS-sq were derived for the white and colored noise. Also, closed-form expressions for the CRLBs were derived when the noise is white. Power loading and WLSEs were proposed to enhance the ranging performance by exploiting noise correlations.

- We developed asynchronous RIPS (ARIPS), where dual-tone signaling is utilized to expand the resolvable range beyond the carrier wavelength and to accommodate the CFOs. A number of participating nodes at each ranging session

was reduced to ease the localization. Simulation results were presented to corroborate the proposed system.

- A combination of the STC, MMW signaling, and the RIPS was investigated for indoor positioning system. Proposed space-time RIPS (STRIPS) resolved the unknown phase shifts due to fading by exploiting the channel characteristics of the MMW spectrum and employing the STC. The performance of the STRIPS was analyzed through simulations and experiments.

- We design a practical indoor positioning system that can be implemented on available communication devices. In accurate indoor positioning system (AIPS), we developed two ranging signal models. To allow the receiver to use a low-cost envelope detector, the ranging signal with a carrier was generated with a AM scheme. The power efficiency of the system was improved when a square-law device or a mixer is available at the receiver by using the ranging signal similar to DSB-SC signals. Ranging signals and a type of receiver were to be chosen depending on the hardware availability, and the performance was compared through simulations. The AIPS with an envelope detector was implemented on the hardware to confirm the efficiency of the proposed AIPS.

7.2 Future Research Topics

The following is a list of possible research topics to extend the research conducted in this dissertation:

- Extend the theoretical analysis of the RIPS by considering different noise colors. When the ACF of the colored noise is available, the analysis of the RIPS-u is fairly straight-forward. In the RIPS-sq, it is necessary to model the aggregated colored noise. Analyze optimal anchor node deployment patterns in the RIPS using the CRLBs of location estimates derived in this dissertation.

- Conduct performance analysis of the AIPS to numerically prove the efficiency of the system and show the relationship between the performance and the choice of parameters.
- Implement the AIPS with square-law device and mixer to compare the performance of two ranging signals experimentally.

APPENDIX A

ACF OF AR1 AND SQUARED AR1 PROCESSES

ACF of AR1 process Given a general AR1 process $v_t = \rho v_{t-1} + u_t$ with $u_t \sim \mathcal{N}(0, \kappa^2)$, we can rewrite the AR1 samples as

$$\begin{aligned} v_1 =& \rho v_0 + u_1, \\ v_2 =& \rho(\rho v_0 + u_1) + u_2, \\ &\vdots \\ v_t =& \rho^t v_0 + (u_t + \rho u_{t-1} + \ldots + \rho^{t-1} u_1). \end{aligned} \tag{135}$$

Since $|\rho| < 1$, when t is large, v_t in (135) can be approximated as

$$v_t \approx u_t + \rho u_{t-1} + \ldots + \rho^{t-1} u_1 = \sum_{i=1}^{t} \rho^{t-i} u_i \tag{136}$$

Using this approximation, the ACF of v_t with a lag τ becomes

$$\begin{aligned} E\left[v_t v_{t-\tau}\right] =& E\left[u_{t-\tau}^2 \rho^\tau \rho^0\right] + E\left[u_{t-\tau-1}^2 \rho^{\tau+1} \rho^1\right] + \ldots + E\left[u_1^2 \rho^{\tau-1} \rho^{t-\tau-1}\right] \\ =& \frac{\kappa^2 \rho^{|\tau|}(1-\rho^{2t})}{1-\rho^2}. \end{aligned} \tag{137}$$

And thus, as $t \to \infty$, the ACF only depends on a lag τ as

$$\lim_{t\to\infty} E\left[v_t v_{t-\tau}\right] = \frac{\kappa^2 \rho^{|\tau|}}{1-\rho^2}. \tag{138}$$

ACF of squared AR1 process The ACF for a squared AR1 process can be derived

similarly. From (136), the ACF of v_t^2 with a lag τ can be expressed as

$$\begin{aligned} E\left[v_t^2 v_{t-\tau}^2\right] =& E\left[\left(\sum_{i=1}^{t}\rho^{t-i}u_i\right)^2\left(\sum_{i=1}^{t-\tau}\rho^{t-\tau-i}u_i\right)^2\right] \\ =& \left(\sum_{i=1}^{t}\rho^{2(t-i)}\kappa^2\right)\left(\sum_{i=1}^{t-\tau}\rho^{2(t-\tau-i)}\kappa^2\right) - 3\sum_{i=1}^{t-\tau}\rho^{2(t-i)}\rho^{2(t-\tau-i)}\kappa^4 \\ &+ 2\left(\sum_{i=1}^{t-\tau}\rho^{(t-i)}\rho^{t-\tau-i}\kappa^2\right)^2 + 3\sum_{t=1}^{t-\tau}\rho^{2(t-i)}\rho^{2(t-\tau-i)}\kappa^4 \\ =& \kappa^4\left[\frac{(1-\rho^{2(t-\tau)})(1-\rho^{2t}) + 2\rho^{\tau}(1-\rho^{2(t-\tau)})^2}{(1-\rho^2)^2}\right] \end{aligned} \tag{139}$$

When $t \to \infty$, (139) becomes

$$\lim_{t\to\infty} E\left[v_t^2 v_{t-\tau}^2\right] = \frac{\kappa^4(1+2\rho^{|\tau|})}{(1-\rho^2)^2}. \tag{140}$$

APPENDIX B

OPTIMAL POWER LOADING UNDER THE WHITE NOISE

We prove that the equal power allocation at two transmitters yields the minimum CRLB when the noise is white. Let us constrain the power as $a_1^2 + a_2^2 = 1$.

Optimal power distribution in the RIPS-u The CRLB of the Q-range estimate in (32) can be rewritten as

$$CRLB(q^{(u)}) = \frac{n_1}{a_1^2} + \frac{n_2}{a_2^2} = \frac{n_1}{a_1^2} + \frac{n_2}{1 - a_1^2}, \tag{141}$$

where

$$n_1 = \frac{c}{2\pi f_1} \sum_{m=1}^{2} \frac{\mathbf{p}_N^T(f_2)\mathbf{K}_m^{-1}\mathbf{p}_N^T(f_2)}{\left(\mathbf{p}_N^T(f_1)\mathbf{K}_m^{-1}\mathbf{p}_N(f_1)\right)\left(\mathbf{p}_N^T(f_2)\mathbf{K}_m^{-1}\mathbf{p}_N(f_2)\right) - \left(\mathbf{p}_N^T(f_1)\mathbf{K}_m^{-1}\mathbf{p}_N(f_2)\right)^2}, \tag{142}$$

and

$$n_2 = \frac{c}{2\pi f_2} \sum_{m=1}^{2} \frac{\mathbf{p}_N^T(f_1)\mathbf{K}_m^{-1}\mathbf{p}_N^T(f_1)}{\left(\mathbf{p}_N^T(f_1)\mathbf{K}_m^{-1}\mathbf{p}_N(f_1)\right)\left(\mathbf{p}_N^T(f_2)\mathbf{K}_m^{-1}\mathbf{p}_N(f_2)\right) - \left(\mathbf{p}_N^T(f_1)\mathbf{K}_m^{-1}\mathbf{p}_N(f_2)\right)^2}. \tag{143}$$

Taking the derivative of (141) with respect to a_1^2, we arrive at

$$\frac{\partial}{\partial a_1^2} CRLB(q) = \frac{-n_1}{a_1^4} + \frac{n_2}{(1 - a_1^2)^2}. \tag{144}$$

Equating (144) to zero and using the quadratic formula, the extrema of (141) are found to be at

$$a_1^2 = \frac{n_1 \pm \sqrt{n_1 n_2}}{n_1 - n_2}. \tag{145}$$

The equation (145) is valid regardless of the noise color. When the noise is white,

$\mathbf{K}_m = \sigma_m^2 \mathbf{I}$. Using (53) and (54), n_k is approximated as

$$n_k = \left(\frac{c}{2\pi f_1}\right)^2 \left(\frac{4}{N}\right) \left(\sigma_1^2 + \sigma_2^2\right). \tag{146}$$

Plugging (146) into (145), we obtain

$$\begin{aligned} a_1^2 =& 1 \left(\frac{1/f_1^2 \pm 1/f_1 f_2}{1/f_1^2 - 1/f_2^2}\right) \\ =& 1 \left(\frac{f_2^2 \pm f_1 f_2}{f_2^2 - f_1^2}\right). \end{aligned} \tag{147}$$

Narrowing down the solutions based the condition $0 < a_1^2 < 1$, we arrive at

$$a_1^2 = 1 \left(\frac{g - f_d/2}{2g}\right) \approx \frac{1}{2}. \tag{148}$$

Therefore, the equal transmission power results in the minimum CRLB of the Q-range estimates in the RIPS-u. Notice that this is true even when $\sigma_1^2 \neq \sigma_2^2$.

Optimal power distribution in the RIPS-sq In the RIPS-sq, the CRLB of the Q-range estimates can be rewritten as

$$CRLB(q^{(sq)}) = \frac{n_0}{(a_1 a_2)^2} = \frac{n_0}{1a_1^2 - a_1^4}, \tag{149}$$

where $n_0 = \frac{c}{2\pi g} \sum_{m=1}^{2} \left(\mathbf{p}_N^T(f_d) \widetilde{\mathbf{K}}_m^{-1} \mathbf{p}_N(f_d)\right)^{-1}$. Taking the derivative of (149) w.r.t a_1^2, we arrive at

$$\frac{\partial}{\partial a_1^2} CRLB(q^{(sq)}) = \frac{-n_0(1 - 2a_1^2)}{a_1^2(1 - a_1^2)}. \tag{150}$$

With $a_1^2 \neq 0, 1$, the optimal transmission power at the first transmitter is given as

$$a_1^2 = \frac{1}{2}. \tag{151}$$

Hence, the equal-power distribution is optimal in the RIPS-sq as well.

REFERENCES

[1] "Performance characteristics of 60-GHz communication systems," tech. rep., Terabeam, Oct. 2002.

[2] Akyildiz, I., Su, W., Sankarasubramaniam, Y., and Cayirci, E., "A survey on sensor networks," *IEEE Commun. Mag.*, vol. 40, pp. 102–114, Aug. 2002.

[3] Amundson, I., Koutsoukos, X., and Sallai, J., "Mobile sensor localization and navigation using RF doppler shifts," in *Proc. ACM MELT*, (San Francisco, CA), pp. 97–102, Sept. 2008.

[4] Bahl, P. and Padmanabhan, V. N., "Enhancements to the RADAR user location and tracking system," tech. rep., Microsoft Research, 2000.

[5] Bahl, P. and Padmanabhan, V. N., "RADAR: an in-building RF-based user location and tracking system," in *Proc. IEEE INFOCOM*, (Tel Aviv), pp. 775–784, Mar. 2000.

[6] Bocquet, M., Loyez, C., Fryziel, M., and Rolland, N., "Millimeter-wave broadband positioning system for indoor applications," in *Proc. IEEE MTT*, (Montreal, QC, Canada), pp. 1–3, June 2012.

[7] Chang, H.-l., Tian, J.-b., Lai, T.-T., Chu, H.-H., and Huang, P., "Spinning beacons for precise indoor localization," in *Proc. ACM SenSys*, (Raleigh, NC), pp. 127–140, Nov. 2008.

[8] Cheng, L., Zhu, M., Gul, M., Ma, X., and Chang, G.-K., "Adaptive photonics-aided coordinated multipoint transmissions for next-generation mobile fronthaul," *J. Lightw. Technol.*, vol. 32, pp. 1907–1914, May 2014.

[9] Cheng, Y., Wang, X., Caelli, T., Li, X., and Moran, B., "Optimal nonlinear estimation for localization of wireless sensor networks," *IEEE Trans. Signal Process.*, vol. 59, pp. 5674–5685, Dec. 2011.

[10] Dardari, D., Conti, A., Ferner, U., Giorgetti, A., and Win, M., "Ranging with ultrawide bandwidth signals in multipath environments," *Proc. IEEE*, vol. 97, pp. 404–426, Feb. 2009.

[11] Dil, B. J. and Havinga, P. J. M., "A feasibility study of RIP using 2.4 GHz 802.15.4 radios," in *Proc. IEEE MASS*, (San Francisco, CA), pp. 690–696, Nov. 2010.

[12] Dil, B. J. and Havinga, P. J. M., "Stochastic radio interferometric positioning in the 2.4 GHz range," in *Proc. ACM SenSys*, (Seattle, WA), pp. 108–120, Nov. 2011.

[13] Fang, H. R., Cao, G. P., Gharavol, E. A., Tom, K., and Mouthaan, K., "60GHz short range planar RSS localization," in *Proc. IEEE APMC*, (Yokohama, Japan), pp. 1396–1399, Dec. 2010.

[14] Hansen, C. J., "WiGiG: Multi-gigabit wireless communications in the 60 GHz band," *IEEE Wireless Commun.*, vol. 18, pp. 6–7, Dec. 2011.

[15] Huang, R., Zaruba, G., and Huber, M., "Complexity and error propagation of localization using interferometric ranging," in *Proc. IEEE ICC*, (Glasgow,UK), pp. 3063–3069, June 2007.

[16] Kaune, R., Horst, J., and Koch, W., "Accuracy analysis for TDOA localization in sensor networks," in *Proc. FUSION*, (Chicaco,IL), pp. 1648–1654, July 2011.

[17] Kusý, B., Balogh, G., Sallai, J., Lédeczi, A., and Maróti, M., "InTrack: high precision tracking of mobile sensor nodes," in *Proc. EWSN*, (Delft, The Netherlands), pp. 51–66, July 2007.

[18] Kusý, B., Lédeczi, A., and Koutsoukos, X., "Tracking mobile nodes using RF doppler shifts," in *Proc. ACM SenSys*, (Sydney, Australia), pp. 29–42, Nov. 2007.

[19] Kusý, B. and Sallai, J., "Analytical solution for radio-interferometric localization of mobile sensors," tech. rep., Institute for Software Integrated Systems, Vanderbilt University, Nashville, TN, Dec. 2006.

[20] Kusý, B., Sallai, J., Balogh, G., and Lédeczi, A., "Radio interferometric tracking of mobile wireless nodes," in *Proc. ACM MobiSys*, (San Juan, Puerto Rico), pp. 139–151, June 2007.

[21] La Scala, B., Wang, X., and Moran, B., "Node self-localisation in large scale sensor networks," in *Proc. IEEE IDC*, (Adelaide, Australia), pp. 188–192, Feb. 2007.

[22] Ledeczi, A., Volgyesi, P., Sallai, J., Kusy, B., Koutsoukos, X., and Maroti, M., "Towards precise indoor RF localization," in *Proc. HotEmNets*, (Charlottesville, VA), June 2008.

[23] Li, W., Wang, X., and Moran, B., "Resolving RIPS measurement ambiguity in maximum likelihood estimation," in *Proc. FUSION*, (Chicago, IL), pp. 1–7, July 2011.

[24] Li, W., Wang, X., and Moran, B., "Sensor network localisation with wrapped phase measurements," in *Proc. FUSION*, (Singapore), pp. 68–73, July 2012.

[25] Li, W., Wang, X., Wang, X., and Moran, B., "Distance estimation using wrapped phase measurements in noise," *IEEE Trans. Signal Process.*, vol. 61, pp. 1676–1688, Apr. 2013.

[26] Li, X. and Pahlavan, K., "Super-resolution toa estimation with diversity for indoor geolocation," *IEEE Trans. Wireless Commun.*, vol. 3, pp. 224–234, Jan. 2004.

[27] Liu, H., Darabi, H., Banerjee, P., and Liu, J., "Survey of wireless indoor positioning techniques and systems," *IEEE Trans. Syst., Man, Cybern. C*, vol. 37, pp. 1067–1080, Nov. 2007.

[28] Lucarelli, D., Saksena, A., Farrell, R., and Wang, I.-J., "Distributed inference for network localization using radio interferometric ranging," in *Wireless Sensor Networks*, vol. 4913 of *Lecture Notes in Computer Science*, pp. 52–73, Berlin: Springer-Verlag, 2008.

[29] Maróti, M., Kusý, B., Balogh, G., Völgyesi, P., Nádas, A., Molnár, K., Dóra, S., and Lédeczi, A., "Radio interferometric geolocation," in *Proc. ACM SenSys*, (San Diego, CA), pp. 1–12, Nov. 2005.

[30] Ohlemueller, T., Winkler, F., and Grass, E., "Radio localization in OFDM networks using the round trip phase," in *Proc. IEEE WPNC*, (Dresden,Germany), pp. 23–27, Mar. 2010.

[31] Pahlavan, K., Akgul, F., Heidari, M., Hatami, A., Elwell, J., and Tingley, R., "Indoor geolocation in the absence of direct path," *IEEE Wireless Commun. Mag.*, vol. 13, pp. 50–58, Dec. 2006.

[32] Pahlavan, K., Krishnamurthy, P., and Beneat, J., "Wideband radio propagation modeling for indoor geolocation applications," *IEEE Commun. Mag.*, vol. 36, pp. 60–65, Apr. 1998.

[33] Pahlavan, K., Li, X., and Makela, J.-P., "Indoor geolocation science and technology," *IEEE Commun. Mag.*, vol. 40, pp. 112–118, Feb. 2002.

[34] Patwari, N., Ash, J., Kyperountas, S., Hero, A., Moses, R., and Correal, N., "Locating the nodes: cooperative localization in wireless sensor networks," *IEEE Signal Process. Mag.*, vol. 22, pp. 54–69, July 2005.

[35] Patwari, N. and Hero III, A. O., "Indirect radio interferometric localization via pairwise distances," in *Proc. EmNets*, (Cambridge, MA), May 2006.

[36] Perry, T., "Navigating the great indoors," *IEEE Spectr.*, vol. 49, pp. 20–20, Nov. 2012.

[37] Pi, Z. and Khan, F., "An introduction to millimeter-wave mobile broadband systems," *IEEE Commun. Mag.*, vol. 49, pp. 101–107, June 2011.

[38] Porretta, M., Nepa, P., Manara, G., and Giannetti, F., "Location, location, location," *IEEE Veh. Technol. Mag.*, vol. 3, pp. 20–29, June 2008.

[39] Proakis, J. G. and Salehi, M., *Digital Communications*. New York, NY: The McGraw-Hill Companies, Inc., fifth ed., 2008.

[40] Rappaport, T. S., *Wireless Communications: Principles and Practice*. Upper Saddle River, NJ: Prentice-Hall, Inc., second ed., 2002.

[41] Roh, W., Seol, J.-Y., Park, J., Lee, B., Lee, J., Kim, Y., Cho, J., Cheun, K., and Aryanfar, F., "Millimeter-wave beamforming as an enabling technology for 5G cellular communications: theoretical feasibility and prototype results," *IEEE Commun. Mag.*, vol. 52, pp. 106–113, Feb. 2014.

[42] Roy, R. and Kailath, T., "ESPRIT-estimation of signal parameters via rotational invariance techniques," *IEEE Trans. Acoust., Speech, Signal Process.*, vol. 37, pp. 984–995, July 1989.

[43] Sadler, B., "Fundamentals of energy-constrained sensor network systems," *IEEE Aerosp. Electron. Syst. Mag.*, vol. 20, pp. 17–35, Aug. 2005.

[44] Sarkar, T. K. and Pereira, O., "Using the Matrix Pencil Method to Estimate the Parameters of a Sum of Complex Exponentials," *IEEE Antennas Propag. Mag.*, vol. 37, pp. 48–55, Feb. 1995.

[45] Sarris, I. and Nix, A. R., "Ricean K-factor measurements in a home and an office environment in the 60 GHz band," in *Proc. 16th IST Mobile & Wireless-Commun. Summit*, (Budapest, Hungary), pp. 1–5, July 2007.

[46] Sayed, A., Tarighat, A., and Khajehnouri, N., "Network-based wireless location: challenges faced in developing techniques for accurate wireless location information," *IEEE Signal Process. Mag.*, vol. 22, pp. 24–40, July 2005.

[47] Schneider, D., "You are here," *IEEE Spectr.*, vol. 50, pp. 34–39, Dec. 2013.

[48] Schroth, G., Huitl, R., Chen, D., Abu-Alqumsan, M., Al-Nuaimi, A., and Steinbach, E., "Mobile visual location recognition," *IEEE Signal Process. Mag.*, vol. 28, pp. 77–89, July 2011.

[49] Seco-Granados, G., Lopez-Salcedo, J., Jimenez-Banos, D., and Lopez-Risueno, G., "Challenges in indoor global navigation satellite systems: Unveiling its core features in signal processing," *IEEE Signal Process. Mag.*, vol. 29, pp. 108–131, Mar. 2012.

[50] Shinotsuka, M., Cheng, L., Ma, X., Chang, G. K., and Zhou, G. T., "AIPS: Accurate indoor positioning system using mm-wave signaling and space-time coding," *IEEE Signal Process. Lett.*, 2015. to submit.

[51] Shinotsuka, M., Cheng, L., Ma, X., Chang, G. K., and Zhou, G. T., "Hardware implementation of the space-time radio interferometric positioning system," in *Proc. IEEE IWS*, (Shenzhen, China), Mar. 2015.

[52] Shinotsuka, M., Wang, Y., Ma, X., and Zhou, G. T., "Designing radio interferometric positioning system employing undersampling techniques," in *Proc. IEEE MILCOM*, (Baltimore, MD), pp. 312 – 316, Oct. 2014.

[53] Shinotsuka, M., Wang, Y., Ma, X., and Zhou, G. T., "Designing radio interferometric positioning systems for indoor localizations in millimeter wave bands," in *Proc. Asilomar Conf. on Signals, Systems, and Computers*, (Pacific Grove, CA), pp. 1184–1188, Nov. 2014.

[54] Shinotsuka, M., Wang, Y., Ma, X., and Zhou, G. T., "Analyzing radio interferometric positioning systems with undersampling receivers," *EURASIP J. Advances in Signal Processing*, 2015. submitted.

[55] Smulders, P., "Exploiting the 60GHz band for local wireless multimedia access: Prospects and future directions," *IEEE Commun. Mag.*, vol. 40, pp. 140–147, Jan. 2002.

[56] Stoica, P. and Li, J., "Lecture notes - source localization from range-difference measurements," *IEEE Signal Process. Mag.*, vol. 23, pp. 63–66, Nov. 2006.

[57] Stoica, P., Li, H., and Li, J., "Amplitude estimation of sinusoidal signals: survey, new results, and an application," *IEEE Trans. Signal Process.*, vol. 48, pp. 338–352, Feb. 2000.

[58] Sun, G., Chen, J., Guo, W., and Liu, K., "Signal processing techniques in network-aided positioning: a survey of state-of-the-art positioning designs," *IEEE Signal Process. Mag.*, vol. 22, pp. 12–23, July 2005.

[59] Tretter, S., "Estimating the frequency of a noisy sinusoid by linear regression (corresp.)," *IEEE Trans. Inf. Theory*, vol. 31, pp. 832–835, Nov. 1985.

[60] Wang, C., Yin, Q., and Chen, H., "Robust Chinese remainder theorem ranging method based on dual-frequency measurements," *IEEE Trans. Veh. Technol.*, vol. 60, pp. 4094–4099, Oct. 2011.

[61] Wang, C., Yin, Q., and Wang, W., "An efficient ranging method based on Chinese remainder theorem for RIPS measurement," *Science China Information Sciences*, vol. 53, no. 6, pp. 1233–1241, 2010.

[62] Wang, X., Moran, B., and Brazil, M., "Hyperbolic positioning using RIPS measurements for wireless sensor networks," in *Proc. IEEE ICON*, (Adelaide, SA, Australia), pp. 425–430, Nov. 2007.

[63] Wang, Y. and Leus, G., "Reference-free time-based localization for an asynchronous target," *EURASIP J. Advances in Signal Processing*, 2012:19, Jan. 2012, doi:10.1186/1687-6180-2012-19.

[64] Wang, Y., Li, L., Ma, X., Shinotsuka, M., Chen, C., and Guan, X., "Dual-tone radio interferometric positioning systems using undersampling techniques," *IEEE Signal Process. Lett.*, vol. 21, pp. 1311–1315, Nov. 2014.

[65] Wang, Y., Ma, X., Chen, C., and Guan, X., "Designing dual-tone radio interferometric positioning systems," *IEEE Trans. Signal Process.*, vol. 63, pp. 1351–1365, Mar. 2015.

[66] Wang, Y., Shinotsuka, M., Ma, X., and Tao, M., "Design an asynchronous radio interferometric positioning system using dual-tone signaling," in *Proc. IEEE WCNC*, (Shanghai, China), pp. 2294 – 2298, Apr. 2013.

[67] Werb, J. and Lanzl, C., "Designing a positioning system for finding things and people indoors," *IEEE Spectr.*, vol. 35, pp. 71–78, Sep 1998.

[68] Winkler, F., Fischer, E., Grab, E., and Fischer, G., "An indoor localization system based on DTDOA for different wireless LAN systems," in *Proc. IST Mobile&Wireless Communications Summit*, (Dresden, Germany), June 2005.

[69] Wyne, S., Haneda, K., Ranvier, S., Tufvesson, F., and Molisch, A., "Beamforming effects on measured mm-wave channel characteristics," *IEEE Trans. Wireless Commun.*, vol. 10, pp. 3553–3559, Nov. 2011.

[70] Xu, G., Zhang, L., Wang, Y., and Hu, Y.-H., "The influence of the carrier frequency inaccuracy and multipath effects on radio interferometric positioning system," in *Proc. IEA*, vol. 154, (Chongqing, China), pp. 847–854, London: Springer, Oct. 2012.

[71] Yang, C. and Shao, H.-R., "WiFi-based indoor positioning," *IEEE Commun. Mag.*, vol. 53, pp. 150–157, Mar. 2015.

[72] Yang, Z., Zhou, Z., and Liu, Y., "From RSSI to CSI: Indoor localization via channel response," *ACM Comput. Surv.*, vol. 46, pp. 25:1–25:32, Dec. 2013.

[73] Zhang, W., Yin, Q., Feng, X., and Wang, W., "Distributed TDoA estimation for wireless sensor networks based on frequency-hopping in multipath environment," in *Proc. IEEE VTC*, (Taipei, Taiwan), pp. 1–5, May 2010.

[74] Zhang, W., Yin, Q., and WenjieWang, "Distributed TDOA estimation for wireless sensor networks," in *Proc. IEEE ICASSP*, (Dallas, TX), pp. 2862–2865, Mar. 2010.

[75] Zhang, Y., Qi, W., Li, G., and Zhang, S., "Performance of ML range estimator in radio interferometric positioning systems," *IEEE Signal Process. Lett.*, vol. 22, pp. 162–166, Feb. 2015.